Measurements of Density Scale Length Dependence of Brillouin Backscatter from Laser Produced Plasmas

R. E. Turner

Report No. 105
June, 1980

I. INTRODUCTION

Controlled thermonuclear fusion holds forth the promise of a virtually inexhaustable energy supply for mankind, and has, therefore, received considerable attention from researchers over the past three decades. Since the fuel, isotopes of hydrogen, must be heated to temperatures of over 1 KeV, it is fully ionized, and rich in the phenomena of plasma physics. While most of the research effort has focused on magnetic confinement, another approach, laser driven inertial confinement, became possible with the advent of high power laser systems. The basis of this approach is to use a laser to compress and heat a fuel pellet to high enough densities and temperatures that a significant number of thermonuclear reactions take place before the pellet disassembles. The basic ideas have been reviewed by a number of authors[1,2].

One of the plasma physics problems of obvious importance is the absorption of the laser light by the plasma. Ideally, one would hope to have all of the light absorbed and used to heat and compress the fuel. The 'classical' absorption of light by a plasma is due to electron-ion collisions, which randomize the electrons' otherwise ordered motion in the electromagnetic field[2].

Since the collision rate is proportional to the density squared[2], collisional absorption is ineffective at low densities. To give a specific example, consider light of one micrometer wavelength incident on a plasma which has an electron temperature of one kilovolt. Collisional absorption is significant only if the density profile is slowly varying (e.g., $L > 30$ μm, where L is the density scale length, n is the electron density, and $L = n(dn/dx)^{-1}$), and then only near the critical surface. The critical surface is the region where the local plasma frequency ($\omega_p^2 = 4\pi ne^2/m$) equals the laser frequency, and beyond which light cannot propagate.

Resonant absorption[3] is thought to be the principle absorption mechanism in current short pulse, small density scale length experiments. The laser light can stimulate the growth of plasma waves at the critical surface; the energy in the plasma waves is then coupled to the electrons either through Landau damping[4], or, in the case of high intensities, wave breaking[5], which generates high energy electrons. The plasma waves are strongly driven only at the critical surface, where their frequency is resonant with that of the incoming laser light.

There are still other candidates for explaining 'anomalous' absorption, such as the parametric decay instability[6]. However, all the absorption mechanisms share a common characteristic; they require the laser

light to propagate to the vicinity of the critical surface. Any plasma instability which hinders this will therefore reduce the absorbed energy, making compression and heating more difficult. One such instability is stimulated Brillouin scattering[6-9].

Brillouin scattering is a three wave parametric instability involving an incident electromagnetic wave, an ion-acoustic wave, and a scattered electromagnetic wave. The scattered wave is very nearly at the same frequency as the incident wave, differing only by the ion-acoustic frequency, which is typically three orders of magnitude smaller than the electromagnetic frequencies. Therefore, the energy in each scattered photon (Planck's constant times the frequency) is very nearly equal to the incident photon's energy; Brillouin scattering can reflect a large fraction of the incident light. As will be shown in chapter II,the instability depends on the ion-acoustic wave being resonantly driven by the beat between the incident and scattered electromagnetic waves. This resonance, or matching condition, can, in general, be satisfied only locally in a plasma with density and velocity gradients. As the gradients become smaller, the conditions for growth of the instability become more favorable. Furthermore, the saturation of the instability, thought to be due to ion heating[10] or ion trapping[11],

will occur at a higher level for a more homogeneous plasma, due to the larger number of ions within the scattering region.

Brillouin scattering is a cause of some concern when one considers the pulse shapes planned for future fusion experiments. Most previous experiments used relatively short, fast rising pulses of 30 to 200 nsec, illuminating thin shells, which resulted in 'exploding pusher' behavior; the shell of the target is rapidly heated and explodes, resulting in multi-kilovolt core temperatures, and densities of 0.2 gm/cm^3 (liquid D-T) or less. There is relatively little underdense plasma present during the laser pulse. In addition, the high intensities cause density profile steepening around the critical surface, further suppressing parametric instabilities. High core densities are not reached, however. Therefore, alternative pulse shapes are now under consideration, or being used, to provide 'ablative pusher' type implosions. Long pulses, 1 nsec or more, starting at low intensities and slowly rising to high intensities, are to be used to ablate away the outside of the target without shock-heating the fuel. As the plasma streams away, the reaction forces will drive the remaining shell inward, compressing the fuel. However, the large amount of underdense plasma produced may be

ideal for the growth of Brillouin scattering, which could reflect the laser light before it has reached the critical surface, and thus reduce the amount of energy absorbed. Thus it is important to be able to predict the amount of Brillouin scattering present in such a situation. Various models and computer simulations have attempted to do this. Their predictions depend on a number of parameters, including laser wavelength and intensity, electron and ion temperatures, and velocity and density profiles. The main thrust of this thesis has been to measure the effect of various density profiles on stimulated Brillouin scattering. In addition, insight into the behavior of this instability in the high intensity, non-linear regime, is provided by temporally resolved backscatter spectral data. To simulate the effects of a shaped pulse, we have used a short (60 psec FWHM), high intensity pulse to irradiate a pre-pulse generated plasma.

Others have examined the behavior of stimulated backscatter, but with different diagnostics, geometry, and/or laser parameters, than the work presented here. Ripin[12], et al., measured backscatter off of plane targets, using a prepulse to create a (presumed) plane plasma. A Raman shifted probe beam measured the density profile. However, the relatively long wavelength of the

probe (6329 Å) restricts the measurement to densities of approximately 10^{19} cm^{-3} or less, far removed from the critical surface. Additionally, the plane geometry can result in a steady state velocity flow profile considerably different from that which occurs with spherical targets. Phillion, et al.[10], measured Brillouin scattering from plane targets irradiated with moderately long pulse widths (150 to 400 psec) and large (100 to 250 μm) focal spots. The density scale lengths were not measured; they were estimated as being comparable to the focal spot radius. The laser pulse was not preceded by a prepulse. The backscatter spectra were dominated by the large outward expansion velocity of the plasma, and consequently show a Doppler shift toward shorter wavelengths. The authors also present a model, based on strong ion heating and consequent large Landau damping, to estimate the total amount of backscattered energy. This model will be reviewed in chapter II, and compared with our data in chapter VI.

We have attempted, in this thesis, to simulate laser fusion experiments with shaped pulses, and to measure the density profiles in the region of greatest importance, e.g., near critical density. To this end, we have used prepulses to create sizeable underdense plasmas, similar to the effect of long, low intensity

pulses; and, we have used an ultraviolet probe beam, capable of measuring electron densities up to 10^{21} cm^{-3}, to measure the density profiles. Density scale lengths obtained ranged from 5 to 50 micrometers.

Our results support the ion-heating theory of Kruer[10], in that a relatively slow increase in back-scattered energy is observed with increasing density scale lengths. The time integrated backscatter spectra show the red shift characteristic of Brillouin scattering.

The time resolved spectra reveal an interesting mode structure in the backscattered light. Several possible explanations of this data will be discussed in chapter VI. This data should be useful in pointing the way toward an increased theoretical understanding of Brillouin scattering.

II. THEORY OF STIMULATED BRILLOUIN BACKSCATTER

A. Linear Theory For Homogeneous Plasmas

In this section, the linearized theory of Brillouin scattering is reviewed. This theory has been covered extensively in the published literature[1,2,3,4]; we will mainly follow the treatment given by Forslund, et al.[4] The basic fluid and Maxwell equations are:

$$\frac{\partial}{\partial t}\underline{v}_\alpha + \underline{v}_\alpha\cdot\nabla\underline{v}_\alpha = \frac{q_\alpha}{M_\alpha}\left[-\nabla\phi - \frac{1}{c}\frac{\partial}{\partial t}\underline{A} + \frac{1}{c}\,\underline{v}_\alpha\times(\nabla\times\underline{A})\right] + -\gamma_\alpha T_\alpha \nabla N_\alpha/(M_\alpha N_\alpha) \tag{1}$$

$$\frac{\partial}{\partial t}N_\alpha + \nabla\cdot(N_\alpha\underline{v}_\alpha) = 0 \tag{2}$$

$$\nabla^2\underline{A} - \frac{1}{c^2}\frac{\partial^2}{\partial t^2}\underline{A} = -\frac{4\pi}{c}\underline{J} + \frac{1}{c}\frac{\partial}{\partial t}\nabla\phi \tag{3}$$

$$\nabla^2\phi = -4\pi\sum_\alpha q_\alpha N_\alpha \tag{4}$$

where α denotes the species (ion or electron), N the number density, $\underline{v}$ the fluid velocity, T the temperature, q the charge, M the mass, and $\underline{J}$ the current. γ is the ratio of specific heats (c_p/c_v), and $\underline{A}$ and ϕ are the usual vector and scalar potentials. Implicit in equation (3) is the choice of the Coulomb gauge ($\nabla\cdot\underline{A} = 0$). We will consider only waves in the $\underline{\hat{x}}$ direction; i.e.,

$$\nabla \equiv \underline{\hat{x}}\cdot\frac{\partial}{\partial x} \quad . \tag{5}$$

Linearizing equation (1), and looking only at motions in the y-z plane, we see that

$$\underline{v}_\alpha = -(q_\alpha/M_\alpha c)\underline{A} \tag{6}$$

to lowest order. Now breaking the density into a homogeneous term plus a spatially dependent pertubation, we have

$$N_\alpha = N_{o\alpha} + n_\alpha(x) \tag{7}$$

The current is then given by

$$\underline{J} = -e\underline{v}_e(N_o + n_e) \tag{8}$$

where we have neglected the contribution due to the ion motion. Using equations (5) and (8), the electromagnetic wave equation (3) becomes

$$-\left\{\frac{\partial^2}{\partial t^2} + \omega_D^2 - c^2\nabla^2\right\}\underline{A} = \omega_p^2\,\frac{n}{N_o}\underline{A} \tag{9}$$

Lack of a species subscript should be understood to refer to electrons; i.e., N_o is the homogeneous, unperturbed part of the electron number density.

To develop an equation for the density perturbation, we take the divergence of equation (1), neglect v_x in the non-linear convective terms, substitute for $\underline{v}$ with equation (2), using

$$\nabla\cdot(N_\alpha\underline{v}) = N_{o\alpha}\nabla\cdot\underline{v} \tag{10}$$

and we have

$$\frac{\partial^2}{\partial t^2}\,n = \frac{-e}{m}\,N_o\nabla^2\phi + (e/mc)^2(N_o/2)\,\nabla^2(\underline{A}\cdot\underline{A}) +$$

$$+ (\gamma\,T_e/m)\,\nabla^2 n \tag{11}$$

for the electrons, and

$$\frac{\partial^2}{\partial t^2} n_1 = (e N_o/M_1) \nabla^2\phi + (\gamma_1 T_1/M_1) \nabla^2 n_1 \qquad (12)$$

for the ions. In the ion equation, we have used $ZN_{o1} = N_o$, and the motion due to the electromagnetic field has been neglected. Now, for Brillouin scattering, we are interested in slow moving (acoustic) waves, so that the quasi-neutral approximation may be applied to the perturbed quantities everywhere except in Poisson's equation. That is, $n = n_e = Zn_1$ but $\nabla^2\phi \neq 0$. Eliminating $\nabla^2\phi$ between equations (11) and (12), and using $(Zm/M_1)<<1$, gives

$$\left[\frac{\partial^2}{\partial t^2} - c_s^2\nabla^2\right] n = N_o \frac{Ze^2}{2mMc^2} \nabla^2(\underline{A}\cdot\underline{A}) \qquad (13)$$

where

$$c_s^2 = (ZT_e + 3T_1)/M_1 \qquad (14)$$

In equation (14), the ratios of specific heats have been chosen appropriately for an acoustic wave; $\gamma_e = 1$ (isothermal), $\gamma_1 = 3$ (adiabatic).

Equations (9) and (13) form a pair of coupled equations describing the parametric interaction of the electromagnetic waves and an ion-acoustic wave. The normal modes of these waves are on the left hand side of the equations; the driving terms are on the right hand side. It should be clear that if a driving term

contains a component at the normal mode (resonance) frequency of one of the waves, that wave will experience exponential growth.

We now consider the particular case of circular polarization. Let

$$\underline{A}_o(x,t) = A_o\left[-\hat{\underline{y}}\cos(\omega_o t - k_o x) + \hat{\underline{z}}\sin(\omega_o t - k_o x)\right] \tag{15}$$

where $\omega_o^2 = \omega_p^2 + k_o^2 c^2$.

It is assumed that equation (15) satisfies the left hand side of equation (9). Let the backscattered wave be given by

$$\underline{A}_1(x,t) = A_{1y}\,\hat{\underline{y}}\cos(\omega_1 t - k_1 x) + A_{1z}\,\hat{\underline{z}}\sin(\omega_1 t - k_1 x) \tag{16}$$

and the ion-acoustic wave by

$$n(x,t) = n\cos(\omega_2 t - k_2 x) \tag{17}$$

We will use exponential notation for convenience. Substituting the expressions (16) and (17) into equations (9) and (13), and using care to keep the right hand side real, we have

$$(-\omega_1^2 + \omega_p^2 + k_1^2 c^2)\left(A_{1y}\, e^{i\omega_1 t - ik_1 x} + C.C.\right) = -(\omega_p^2/N_o)(1/2)\left(n\, e^{i\omega_2 t - ik_2 x} + C.C.\right)\left(-A_o e^{i\omega_o t - ik_o x} + C.C.\right) \tag{18}$$

and

$$(-\omega_2^2 + c_s^2 k_2^2)(n\, e^{i\omega_2 t - ik_2 x} + C.C.) =$$

$$\frac{Ze^2 N_o}{2mMc^2}\nabla^2\left[(-A_o e^{i\omega_o t - ik_o x} + C.C.)(A_{1y} e^{i\omega_1 t - ik_1 x} + CC) + \right.$$

$$\left.(-i)(A_o e^{i\omega_o t - ik_o x} + CC)(A_{1z} e^{i\omega_1 t - ik_1 x} + CC)\right] \tag{19}$$

where C.C. stands for complex conjugate of the preceding term. In equation (19) the terms $\underline{A}_o \cdot \underline{A}_o$ and $\underline{A}_1 \cdot \underline{A}_1$ have been dropped, since they have no components at the low frequency ω_2, and are therefore unimportant in driving the instability. The equation for A_{1z} is identical to equation (18) with the replacement

$$A_{1y} = -A_{1z} \quad . \tag{20}$$

Since we will see shortly that k_1 is negative (i.e., $\underline{A}_1$ is backscattered), equation (20) shows that for a left circularly polarized incident wave, the backscattered wave is right circularly polarized, and vice versa.

Knowing that the acoustic frequency ω_2 is much less than the electromagnetic frequencies ω_o and ω_1, we see that equations (18) and (19) can be satisfied only if

$$\omega_o = \omega_1 + \omega_2^* \tag{21}$$

and $$k_o = k_1 + k_2^* \tag{22}$$

These are called the matching conditions. One sees the quantum mechanical analog by multiplying these equations by $(h/2\pi)$; equations (21) and (22) then represent conservation of energy and momentum, respectively. We also see that, as illustrated in Figure 1, $k_2 = 2k_o = -2k_1$.

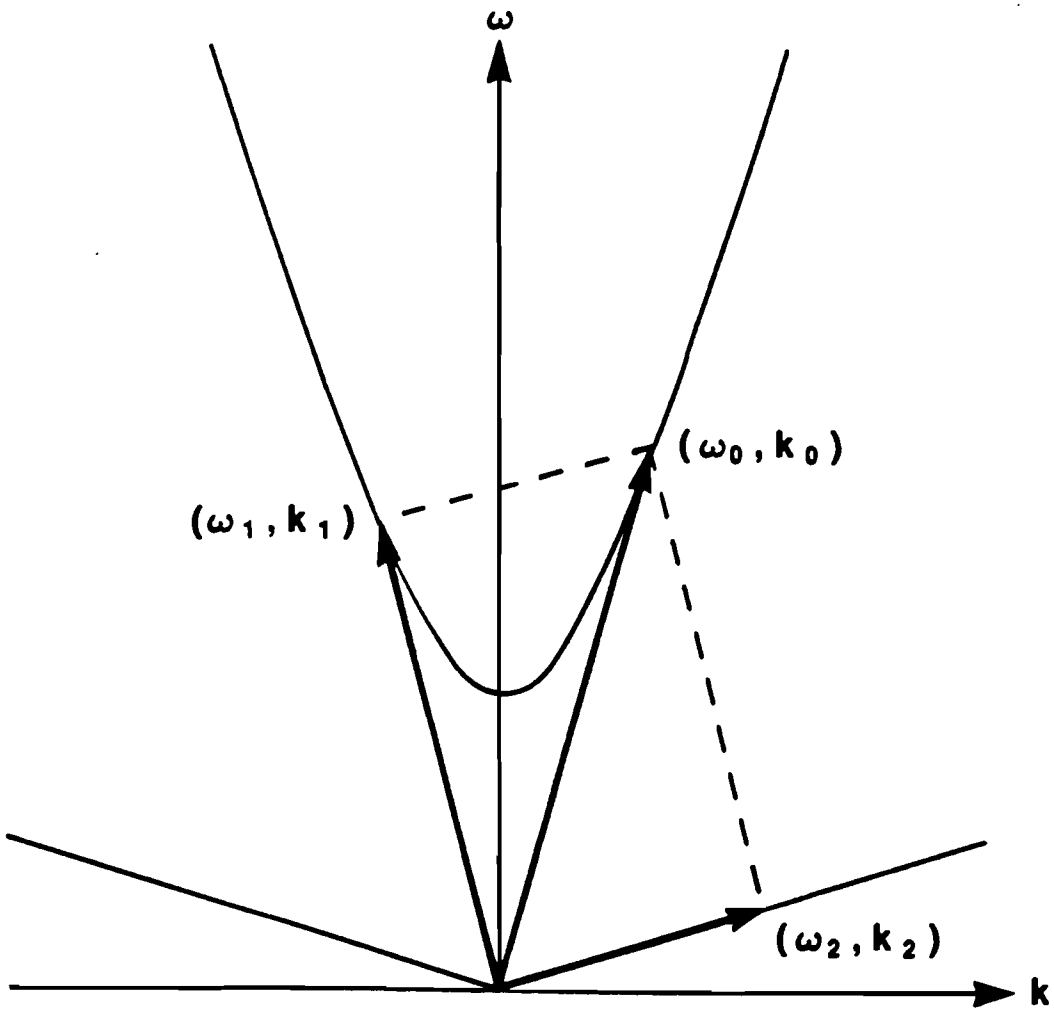

Figure 1. An (ω,k) diagram. The upper curve is the dispersion relation for an electromagnetic wave; the lower, for an ion-acoustic wave (shown with a greatly exaggerated slope, for clarity). The vector-like construction guarantees that the matching conditions will be satisfied.

Keeping only the resonant driving terms, equations (18) and (19) become

$$(-\omega_1^2 + \omega_p^2 + k_1^2c^2)\, A_{1y} = (\omega_p^2/2N_o)A_o n^* \qquad (23)$$

$$(-\omega_2^2 + c_s^2k_2^2)\, n = (Ze^2N_ok_2^2/mMc^2)A_oA_{1y}^* \qquad (24)$$

Taking the complex conjugate of equation (24) and eliminating n^* in equation (23) yields

$$(-\omega_1^2 + \omega_p^2 + k_1^2c^2)(-\omega_2^{*2} + c_s^2k_2^2) = (Ze^2\omega_p^2k_2^2/2mMc^2)A_oA_o^* \qquad (25)$$

Now using equation (21), letting $\omega_2 = \omega_{2r} + i\gamma_o$ where $\omega_{2r}^2 = c_s^2k_2^2$, $\gamma_o << \omega_{2r}$, and using $k_1^2 \approx k_o^2$, we have finally the homogeneous growth rate in the absence of damping[4]:

$$\gamma_o = -k_2v_o\omega_{pi}(8\omega_o\omega_2)^{-\frac{1}{2}} \qquad (26)$$

where $\omega_{pi}^2 = (Zm/M)\omega_p^2$, and $v_o = (e/mc)A_o$ is the electron 'jitter' velocity. For parameters typical of our experiments ($I = 10^{16}$ W/cm^2 or $v_o = 10^9$ cm/sec, $\lambda_o = 1$ μm), we see that $\gamma_o = 10^{13}$ sec^{-1}. The homogeneous growth rate is indeed large, even on picosecond time scales.

B. Quasi-Modes

Using equation (25), it is possible to examine the situation where the electromagnetic pump is so strong that it dominates the restoring force due to the electron

pressure, namely, $\omega_2 >> k_2 c_s$. These waves are called quasi-modes[5], since they do not obey the usual ion-acoustic dispersion relation. Using $\omega_2 >> k_2 c_s$ in equation (25), and solving for the growing root, we have

$$\omega_2 = \frac{1 - i\sqrt{3}}{2} \left\{ \frac{k_o^2 v_o^2}{\omega_o} \omega_{pi}^2 \right\}^{1/3} \tag{27}$$

with the requirement that

$$(v_o/v_e)^2 >> 4\omega_o c_s k_2/\omega_{pe}^2 \tag{28}$$

where again $k_2 = 2k_o$. We note that the frequency of the quasi-modes depends on the incident intensity to the one-third power.

C. Linear Theory For Inhomogeneous Plasmas

We now consider Brillouin scattering in an inhomogeneous plasma. The linearized problem has been extensively described in the literature[1,4,6], and only the main points will be reviewed here. It is customary to define the wavenumber mismatch K(x) as

$$K(x) = k_o(x) - k_1(x) - k_2(x) \tag{29}$$

where, as before, the subscripts 0, 1, 2, refer to the incident electromagnetic wave, the backscattered wave, and the ion-acoustic wave, respectively. Since the plasma parameters may vary with position, the wavenumbers depend on x, and, in general, it will be possible to

satisfy the matching conditions exactly ($K = 0$) only at one point in space. The growth of the waves will be limited to a region around that point such that the total phase mismatch is small; i.e.,

$$\left|\int K(x)\, dx\right| < (\pi/2) \quad .$$

For simplicity, one usually considers plasma parameters which are linear functions of position:

$$\omega_p^2(x) = \omega_p^2 \,(1 - x/L_n) \tag{30}$$

$$T_e(x) = T_e \,(1 - x/L_T) \tag{31}$$

$$u(x) = u_o \,(1 - x/L_u) \tag{32}$$

u is the plasma fluid velocity. In the presence of a non-zero fluid motion, the ion-acoustic wave will be Doppler shifted, and its dispersion relation is[1]

$$\omega = (\underline{k}\cdot\underline{u} + kc_s)(1 + k^2\lambda_D^2)^{-\frac{1}{2}} \tag{33}$$

The factor inside the square root comes from charge separation effects, which were neglected when we used quasi-neutrality in the first section. We will usually use the limit $k^2\lambda_D^2 << 1$.

Rosenbluth has shown[6] that, for a wavenumber mismatch approximated by

$$K(x) = K'(0)\, x \ , \tag{34}$$

the instability is convective, with a spatial amplification, in the absence of damping, given by

$$I = I_o \exp(2\pi\lambda_\beta) \tag{35}$$

where $$\lambda_\beta = (\gamma_o^2/K'v_-c_s) \tag{36}$$

γ_o is the homogeneous growth rate (equation (26)), and v_- is the group velocity of the backscattered wave; $v_- = c^2|k_1|/\omega_1$. I is the intensity of the backscattered wave, and I_o is its initial (thermal noise) intensity. Clearly, substantial amplification requires $\lambda_\beta > 1$. For the linearized plasma parameters given by equations (30), (31), and (32), K' is found to be[4]

$$K' = (\omega_o/c)\{(\omega_p^2/\omega_o^2)(1/L_n) - (2/L_u)\} +$$

$$-k_2\omega_{pi}(\omega_{pi}^2 - \omega_2^2)^{-\frac{1}{2}}[(1/2L_T) + (\omega_2^2/2L_n)(1/(\omega_{pi}^2 - \omega_2^2))] \qquad (37)$$

To find the instability threshold, we require the amplification factor λ_β to be order one. Specializing to $\omega_{pi} >> \omega_2$, and $k_2 = 2k_o$, the threshold is given by[4]

$$(v_o/v_e)^2 > 4\{(c/\omega_o L_n)[1 - (4v_e^2 ck_o^3\omega_o/\omega_{pe}^4)] +$$

$$-(c^2k_o/L_T\omega_{pe}^2) - (2c\omega_o^2/L_u\omega_o\omega_{pe}^2)\} \qquad (38)$$

In our experiment, the plasma is approximately isothermal throughout the region of interest, so $L_T^{-1} = 0$. Also, for $k^2\lambda_D^2 << 1$, the second term may be neglected. The two remaining terms describe the effects of the wavenumber mismatch of the electromagnetic waves due to the changing density, and the changing ion-acoustic wavenumber due to the position dependent flow velocity. For most plasmas of interest for laser fusion, the fluid velocity increases

as one moves toward lower densities, so that L_u is negative in equations (32) and (38), and in (39) below. With the approximations mentioned above, the amplification factor, given by equation (36), is

$$\lambda_\beta = (1/8)(v_o/v_e)^2(\omega_p/\omega_o)^2 k_o\left[(1/2L_n)(\omega_p/\omega_o)^2-(1/L_u)\right]^{-1} \tag{39}$$

This is the spatial amplification of a backscattered wave in an inhomogeneous plasma. In equations (38) and (39), $u_o >> c_s$ has been assumed. For $u_o << c_s$, the following replacement is made:

$$(1/L_u) \rightarrow (M^*/L_u) \tag{40}$$

where M^* is the Mach number, (u_o/c_s). We see that subsonic flows reduce the importance of velocity gradients. Inserting parameter values of the order expected in these experiments ($(v_o/v_e) \sim 1$, $(\omega_p/\omega_o) = 0.5$, $L_n = -L_u = 20\ \lambda_o$), we see that $\lambda_\beta > 1$, so that large backscatter is predicted.

It should be noted that the theory thus far presented is a linearized one; that is, the incident wave is considered to be large and unchanging, while the backscattered and ion-acoustic waves are small and growing. Only resonant interactions between the incident wave and one of the small waves are considered. However, when the backscatter grows large, other terms may be important. For example, it has been shown[7] that

when the ion-acoustic wave grows large ($\{n/N_o\} > k^2\lambda_D^2$), strong harmonic generation occurs. These harmonics can interact with the pump wave to drive backscatter at $(\omega_o - 2\omega_2)$, $(\omega_o - 3\omega_2)$, etc., while the fundamental backscatter at $(\omega_o - \omega_2)$ continues to drive the acoustic wave. Another complication we have ignored is the possibility of two or more stimulated scatterings taking place in the plasma[8]. For this to occur, the back-scattered waves must be comparable to the pump wave, so the linear theory is no longer applicable. Additional problems include pump depletion, the strong Landau damping which occurs when the ion temperature approaches the electron temperature, and other non-linear dissipation mechanisms such as ion trapping and wave breaking. The proper treatment of these non-linear effects in limiting Brillouin scattering is currently as area of active research. Some of the ideas involved will be reviewed in the next section.

D. Non-Linear Models of Brillouin Scattering

Non-linear models of Brillouin scattering generally assume that the density perturbation has saturated at a value δn. Some of the possible saturation mechanisms are listed at the end of the previous section. We assume that the amplitudes of the backscattered and incident

waves are slowly varying functions of position; i.e.,

$$\underline{A}_1 = \underline{A}_1(x)\cos(\omega t - k_1 x) \tag{41}$$

where $k_1 A_1' >> A_1''$,

and similarly for the incident wave $\underline{A}_o$. Consider a plasma of constant density N_o and length L. Then substitution of (41) into the wave equation (9) yields[9,10]

$$\frac{d}{dx} A_1 = -\alpha \frac{\delta n}{N_o} A_o \tag{42}$$

and similarly for the incident wave

$$\frac{d}{dx} A_o = -\alpha \frac{\delta n}{N_o} A_1 \tag{43}$$

where

$$\alpha = (\omega_p^2/4k_1c^2) = (\pi/2)(N_o/n_c)(1/\lambda_o)\left[1-N_o/n_c\right]^{-\frac{1}{2}} \tag{44}$$

and where λ_o is the vacuum wavelength. As in the linear case, the non-resonant driving terms have been dropped. If we normalize the incident wave to one ($A_o(0) = 1$), and assume that the initial backscatter noise level is small ($A_1(L) = 0$), then the solution to equations (42) and (43) is

$$A_o = \left(e^{\theta x/L} + e^{2\theta} e^{-\theta x/L}\right)\left(1 + e^{2\theta}\right)^{-1} \tag{45}$$

$$A_1 = \left(-e^{\theta x/L} + e^{2\theta} e^{-\theta x/L}\right)\left(1 + e^{2\theta}\right)^{-1} \tag{46}$$

where $\theta = \alpha L(\delta n/N)$

The reflectivity is given by

$$r = |A_1(0)/A_o(0)|^2 = \tanh^2(\theta) \tag{47}$$

We will now consider two of the possible mechanisms which can limit the size of the ion wave, starting with ion trapping[7]. When the wave amplitude grows to a value such that the ion velocities are affected, then trapping can occur. Specifically, the ions which have velocities comparable to the wave's phase velocity feel the potential of the wave for a long period of time. The ions are accelerated; the energy they gain is lost from the wave. This loss limits the wave amplitude. A crude estimate of the value of $\delta n/N$ for which trapping occurs may be obtained by modeling the distribution with the water-bag model[11]. (In this model, the ion distribution function is a constant for $|v| < \sqrt{3}\, v_i$, and zero otherwise.) Calculating the size of the wave where the ion velocity (driven plus thermal) equals the wave velocity, one finds

$$(\delta n/N) = (1/2)\left\{(1 + (T_i/T_e))^{\frac{1}{2}} - (3T_i/T_e)^{\frac{1}{2}}\right\}^2 \qquad (48)$$

Since we will see that this model has serious failings if the ion temperature is comparable to the electron temperature, we will take, as an example, $(T_i/T_e) = 0.1$. Then equation (48) gives $(\delta n/N) = 0.13$. Continuing the example, if $N = 0.2\, n_c$, and $L = 20\, \lambda_o$, then equation (47) predicts a reflectivity of 50%. Clearly, ion trapping does not limit the Brillouin scattering to small values.

We now consider the possibility of the size of the ion wave being limited by harmonic generation. For finite $\delta n/N$, the plasma's phase space characteristics intersect[7], indicating that shock waves can form there. Near the intersection, the waveform steepens, generating harmonics. The time for a disturbance to propagate to the shock point is

$$t_1 = \pi\left(2\,\omega\,(\delta n/N)\right)^{-1} \tag{49}$$

However, no shock will form if the plasma is too dispersive; that is, if the harmonics are appreciably out of phase (say, by $\lambda/4$) with the fundamental at t_1. To estimate the dispersion time, the complete dispersion relation must be used:

$$\omega^2 = c_s^2 k^2 \left(1 + k^2 \lambda_D^2\right)^{-1} \tag{50}$$

We then find the time for the fundamental and second harmonic to be out of phase:

$$t_2 = \pi\left(3\omega k^2 \lambda_D^2\right)^{-1} \tag{51}$$

Equating t_1 and t_2, we find the condition for harmonic generation:

$$(\delta n/N) = k^2 \lambda_D^2 \tag{52}$$

If this limit is exceeded, the wave's energy cascades into the harmonics. Applying the same parameters we used previously ($N = 0.2\ n_c$, $L = 20\ \lambda_o$) and taking $T_e = 2$ KeV,

equation (52) gives $(\delta n/N) = 0.06$, and equation (47) predicts a reflectivity of 17%, considerably lower than the ion-trapping limit. It should be noted that equation (47) predicts a drastic increase in Brillouin scattering for increasing scale lengths. For example, if we use $L = 40\ \lambda_0$ in the above example, the reflectivity increases to 50%.

We now review a model, due to Kruer[12,13], which takes into account the finite amount of ion heating. It is well known[14] that ion-acoustic waves are strongly (ion) Landau damped, unless $(ZT_e/T_i) >> 3$. Ion-trapping by the wave produces a 'tail' of energetic ions; however, the model assumes, for simplicity, that the effect is similar to uniform heating of the ions[15]. Since the ions are warm, they Landau damp the acoustic wave. This damping, in turn, deposits more energy into the ions; the ion temperature rises, and this increases the damping. Thus, we have a negative feedback mechanism which seeks to limit the size of the ion-acoustic wave.

To calculate the size of the wave, we must use equation (13). As before, only the resonant terms are kept, yielding

$$\frac{\delta n}{N_o} = \frac{Ze^2k^2}{2m_i M\omega\nu c^2}\ A_o A_1 \qquad (53)$$

where ω is the ion-acoustic frequency, and ν is the Landau damping rate, given by[14]

$$\nu = \omega\sqrt{\pi/8}\ (ZT_e/T_i)^{3/2}\exp(-ZT_e/2T_i) \qquad (54)$$

where $k^2\lambda_D^2 << 1$ has been assumed. It should be noted that, for our experiments using silicon dioxide plasmas, the proper Z to use in equation (54) is the charge state of the oxygen ions. Not only are they the most abundant species, but they are also the lightest; their thermal velocity is larger, and they therefore damp the acoustic wave more effectively. (The exponent in equation (54) should have $M_j\langle Z/M\rangle$ instead of simply Z, where M_j is the mass of the j^{th} species, and $\langle\ \rangle$ denotes a species average. For our plasmas, however, $\langle Z/M\rangle = Z_j/M_j$ for all species. Thus the exponent is smallest for the smallest mass, and $M_j\langle Z/M\rangle = Z_j$.)

Equations (42), (43), and (53) can be solved for the reflectivity[13,16], for a plasma of density n and length L:

$$r(1 - r) = B(\exp[q(1 - r)] - r) \qquad (55)$$

where

$$q = (k_oL/4)(n/n_c)(\omega/\nu)(v_o/v_e)^2(1-n/n_c)^{-1}(1+3T_i/ZT_e)^{-1} \qquad (56)$$

Here B is the initial noise level of the backscattered wave ($B = A_1(L)$), k_o is the vacuum wavenumber of the incident wave, $v_o = (eA_o/mc)$, and $v_e^2 = T_e/m$. The damping rate, ν, depends on the ion temperature (see equation (54)).

To estimate T_i, it is assumed that all of the acoustic wave energy is going into heating the ions, and that the ions are transporting the energy away as fast as possible (free streaming). Equating these two terms gives

$$rI_o\omega/\omega_o = n_i v_i T_i \tag{57}$$

Here rI_o is the fraction of the incident wave undergoing Brillouin scattering, and $(\omega/\omega_o) = 2k_o c_s/\omega_o$ is the fraction of the scattered energy which goes into the ion-acoustic wave. Equations (55) and (57) can be solved iteratively for the reflectivity, r. For example[13], if $n = 0.2n_c$, $T_e = 6$ KeV, and $I_o = 3\times10^{15}$ W/cm^2 at $\lambda_o = 1$ μm, then r = 10% for $L = 10\lambda_o$, and r = 40% for $L = 100\lambda_o$. As predicted earlier, we see that ion heating has a negative feedback effect; the increase in back-scatter with increasing scale length is much slower than was predicted when ion heating was ignored (equation (47)).

Finally, an estimate can be made for the time required to heat the ions to $T_i = ZT_e/3$. Assuming r is a constant, one gets[13]

$$t_h = L(n/n_c)(v_e/v_o)^2(1/3c_s r) \tag{58}$$

as the time required to heat the ions. For the example above, with $L = 100\lambda_o$, $t_h = 100$ psec. It should be noted that equation (58) overestimates the time required for ion damping to be important. Inspection of the damping rate, equation (54), shows that the damping is a maximum

for $ZT_e/T_i = 3$; however, it is still appreciable for much larger temperature ratios. For example, if $ZT_e/T_i = 12$, then equation (54) gives, for $\lambda_o = 1\ \mu m$ and $T_e = 1$ KeV, $\nu^{-1} = 6$ psec.

E. Hydrodynamics

We will now review two of the aspects of the coronal hydrodynamics which can effect our experiment. First of all, as was pointed out in equation (39), velocity gradients can limit the size of the phase-matching region, by Doppler shifting the acoustic wave frequency. These gradients are likely to be large in plane target experiments, due to the one dimensional nature of the expansion. They may also be large in short pulse experiments, where hydrodynamic steady state may not be reached during the laser pulse. However, in our prepulse experiments, the plasma has time to expand into a quasi-steady state flow. Our measurements will show that the density profile is well described by an exponential over the range of 1 to 9×10^{20} cm^{-3}. If we assume that it is exponential everywhere ($n = n_c \exp(-z/L_n)$), and that we have steady state flow, then we can use the continuity equation ($\nabla\cdot(n\underline{v}) = 0$) to find the velocity as a function of z, the distance from the critical surface. Defining the velocity scale length in the usual fashion,

$$L_u = v(dv/dz)^{-1}$$

we find

$$L_u = L_n(R + z)/(R + z - 2L_n) \qquad (59)$$

where R is the radius to the critical density, and z is the radial distance measured from the critical surface. For our parameters of R = 40 μm, and L_n from 10 to 40 μm, equation (59) shows that the velocity scale lengths are always greater than the density scale lengths. Furthermore, L_u is particularly large in the density region of 0.1 to 0.5 of critical density, especially for density scale lengths of 20 μm or more. Therefore, the velocity gradients are not of great importance in limiting the phase-matching length at densities near critical density.

The plasma hydrodynamics can effect the interpretation of the spectral data. If the critical surface is moving, or if ions are flowing through the critical surface, the reflected light will be Doppler shifted[17]. Since this shift is toward shorter wavelengths for plasma motion outward, it can mask or confuse the interpretation of the Brillouin shift toward longer wavelengths. When there is no prepulse, this is indeed the case. With a prepulse formed plasma, however, the hydrodynamic motions have time to relax to a quasi-steady state. Further evidence in support of this statement is the observation[18] that, with long pulse irradiation, the critical surface

moves out rapidly for the first ~70 psec, but then assumes a more or less stationary position for the duration of the pulse. Since the Doppler shift is $\Delta\lambda/\lambda = 2v/c$, critical surface velocities of less than 6×10^6 cm/sec will produce spectral shifts of less than 4 Å.

One can also use a steady state, isothermal model[18] to estimate the plasma flow velocity. For short pulse experiments, the isothermal assumption is not particularly accurate, so the results should be considered as order of magnitude estimates. The equation of motion may be integrated to obtain

$$v^2 = 2c_s^2 \ln(n_s/n) + v_s^2 \qquad (60)$$

where c_s is the ion-acoustic speed, n_s and v_s are the density and velocity at the plasma source. One usually assumes $(n_s/n) >> 1$, and $c_s >> v_s$. Similarly, the mass conservation equation (steady state) may be integrated, giving

$$r^2 nv = (1/4\pi)(\dot{m}/M_i) \qquad (61)$$

where $\dot{m}$ is the (constant) rate of mass flow, in a spherically symetric geometry. Equation (60) predicts an outward flow velocity of approximately $2c_s$ in the vicinity of the critical surface. This flow of material into the underdense region can give rise to a spectral shift toward shorter wavelengths. For a one dimensional

expansion, the shift is given by[17]

$$(\Delta\lambda/\lambda) = -(u/c) \tag{62}$$

where u is the flow velocity at the critical surface. However, for a three dimensional steady state flow, the magnitude of this shift is reduced by the factor $(R_c/R_F)^2$ where R_c is the radius of the critical density, and R_F is the radius of the expansion front. This extra factor, which is due to the three dimensional steady state continuity equation ($\nabla\cdot(r^2 n\underline{v}) = 0$), can reduce the predicted blue shift by an order of magnitude or more. This is especially true for prepulse formed plasmas, where $R_F >> R_c$.

III. EXPERIMENTAL PROCEDURES

A. Introduction

There are two specific objectives in this thesis. The first is to present data showing the relationship between the density gradient and the amount of stimulated backscatter produced, when a spherical glass microshell is illuminated with a high power laser. In the following sections, we describe the laser system, and the diagnostics used for these measurements; the optical probe beam and holographic interferometry, and the calorimetry. The numerical procedures used to unfold the interferometric data are discussed in chapter IV.

The second objective of this work is to examine the spectral content of the backscattered energy, with emphasis on time resolved spectroscopy. The procedures and equipment used for these measurements are described in the final two sections of this chapter.

B. Glass Development Laser

The Laboratory For Laser Energetics' Glass Development Laser[1] (GDL) is a one beam, phosphate glass system capable of peak powers in excess of 0.5 TW in short pulses. Figure 2 shows a schematic diagram of the laser

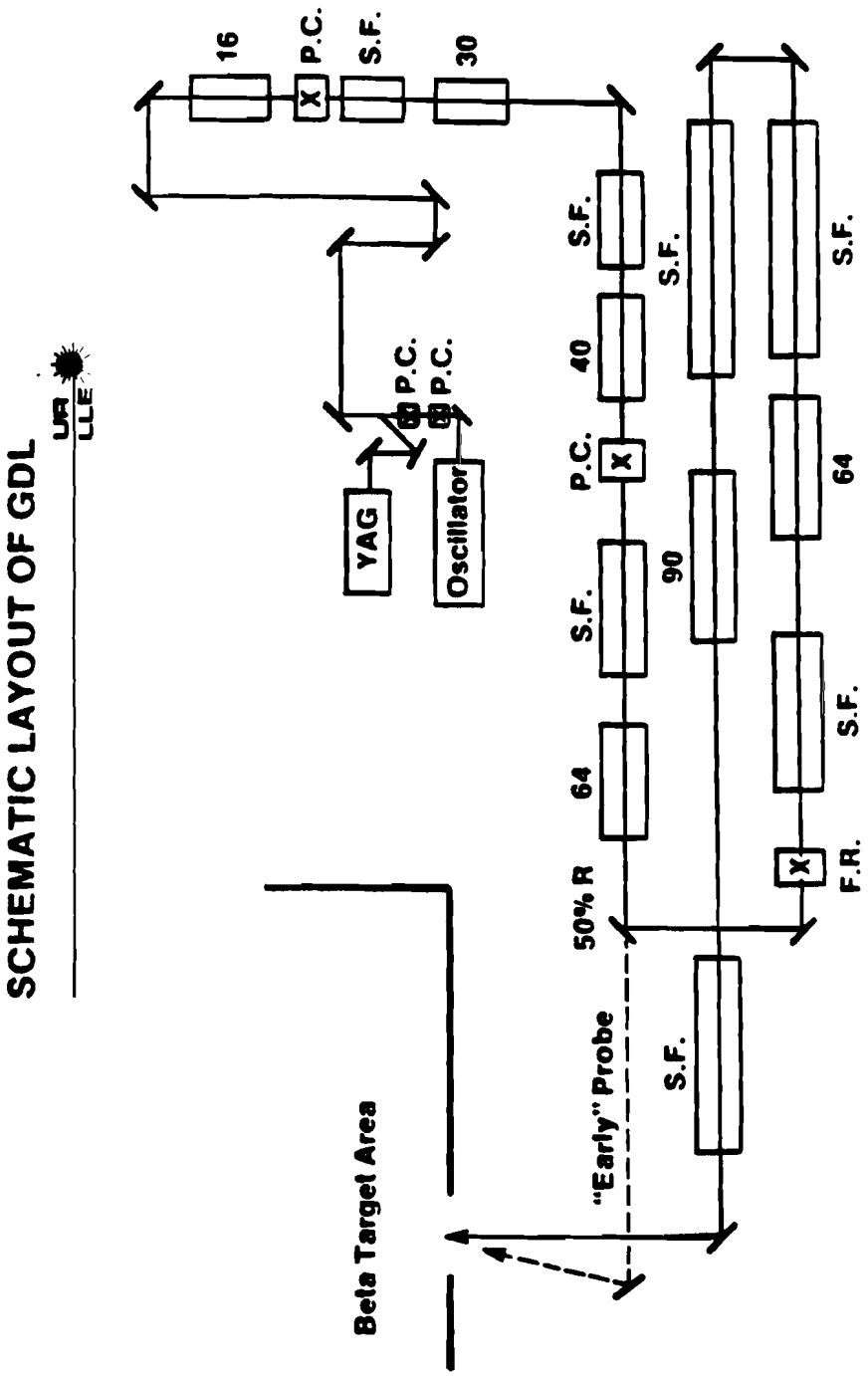
SCHEMATIC LAYOUT OF GDL
UR
LLE
16
P.C.
S.F.
30
YAG
Oscillator
P.C.
P.C.
S.F.
40
P.C.
S.F.
90
64
50% R
"Early" Probe
Beta Target Area
S.F.
S.F.
S.F.
64
S.F.
F.R.

Figure 2

system. Notice that there are two beams exiting the room; one is the output of the last laser amplifier, while the other contains half of the energy output of the first 64 mm rod amplifier. This latter beam will be referred to as the 'early' probe beam.

The GDL system was slightly modified to allow for the introduction of a controlled prepulse. The prepulse insertion system is shown in Figure 3. A translation stage, holding the retroreflecting prism, makes it possible to adjust the prepulse timing from 0.5 nsec, to 1.8 nsec, before the main pulse. The two half-wave plates, in conjunction with the polarizer P, independently adjust the intensity of the main pulse and the prepulse. The main pulse is always reduced by at least a factor of two, to avoid overdriving the laser system. Therefore, ratios of prepulse energy to main pulse energy of zero to ten percent are available.

The prepulse system was assembled as follows. First, the retroreflecting prism was adjusted, with a helium-neon laser, to have its front face orthogonal to the direction of motion of the sliding stage. This assembly was then inserted into the prepulse system, and mirror M2 adjusted to bring the YAG alignment beam orthogonal to the prism's front surface. This left the laser beam parallel to the slide direction, so that when

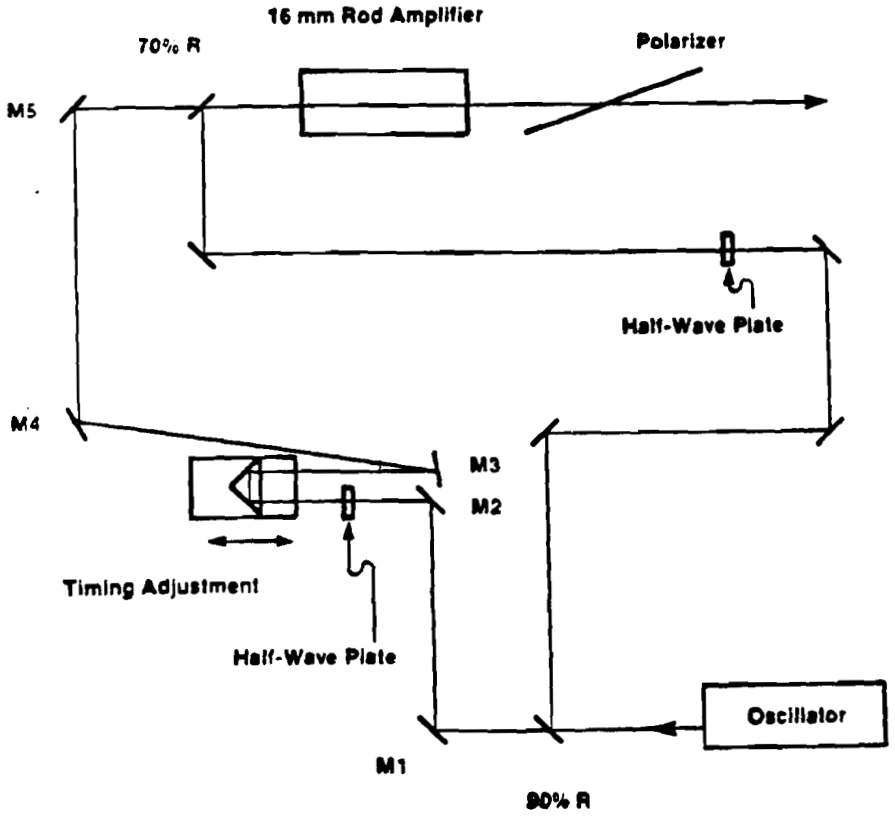

Figure 3. Prepulse System

the stage was translated back and forth, there was no change in the location of the retroreflected beam on M3. Mirrors M4 and M5 were then used to insert the prepulse back into the laser system.

Measurement of the relative timing between the prepulse and the main pulse was accomplished using a vacuum photodiode and a Tektronics 7844 oscilloscope. The half-wave plates were adjusted so that the prepulse and main beam were of approximately equal intensity, and a low power shot, firing only the first 4 rod amplifiers, was taken. From the resulting oscilloscope trace, the prepulse to main beam time difference was found to be 1.8 nsec. The accuracy, limited mainly by the rise time of the scope and 80 feet of RG-59 cable, is estimated at 0.2 nsec. The position of the translation stage was noted, and all subsequent prepulse times were calculated from $t = 1.8(\text{nsec}) - 2d/c$, where 2d is the distance by which the path length was increased. Since this can easily be measured to millimeter accuracy, the reproducibility of any setting is accurate to within a few picoseconds.

We will end this section with a brief description of the target area, also known as Beta. A schematic diagram is shown in Figure 4. At the first mirror the GDL beam encounters in the target room, four percent of

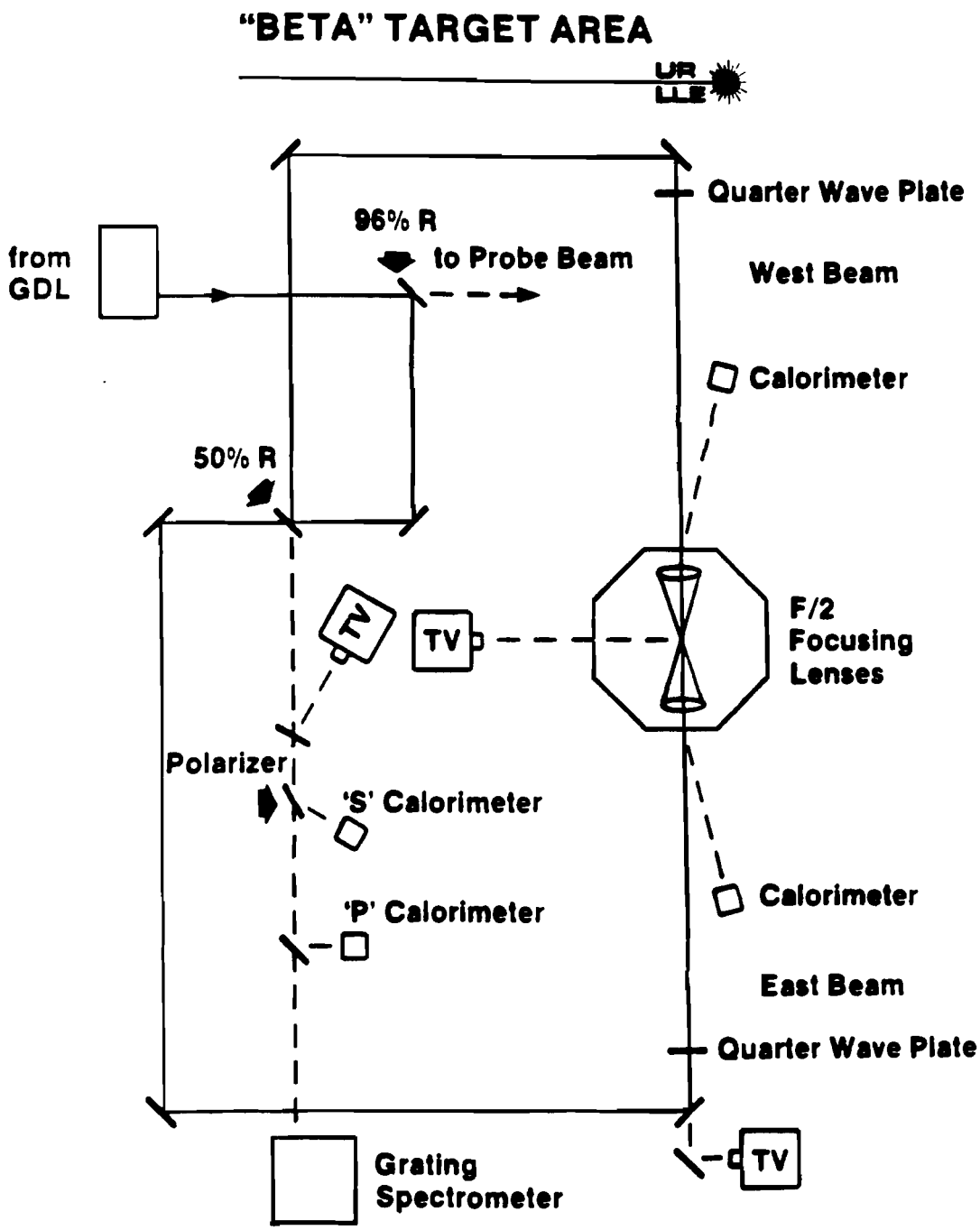
"BETA" TARGET AREA
UR
LLE
Quarter Wave Plate
96% R
from
GDL
to Probe Beam
West Beam
Calorimeter
50% R
TV
TV
F/2
Focusing
Lenses
Polarizer
'S' Calorimeter
'P' Calorimeter
Calorimeter
East Beam
Quarter Wave Plate
TV
Grating
Spectrometer

Figure 4

the energy is transmitted and directed to the probe beam table. This beam will be referred to as the 'synchronous' or 'main' probe beam, to distinguish it from the early probe beam. The remaining ninety six percent of the energy is then split into two approximately equal intensity beams, which are directed through quarter-wave plates and into the vacuum chamber from opposite directions. Inside the chamber, F/2 aspheric lenses focus the beams onto the target. The quarter-wave plates are oriented to give right circular polarization.

A videcon is positioned to view the target through the fifty percent beamsplitter; it observes the back-reflected light of the YAG alignment laser, insuring proper focus. (A 50 μm correction is applied to the focusing lenses to compensate for the chromatic shift due to the 100 Å difference between YAG and phosphate glass lasing wavelengths.) This backscatter viewing system was also used to confirm the proper alignment of the prepulse insertion system, by allowing the YAG to propagate only along the path taken by the prepulse, and checking that it too was properly focused on target.

C. Ultraviolet Probe Beam

A synchronous, ultraviolet probe beam was constructed, so that the electron density could be measured

interferometrically. The wavelength was made as short as was practical, in order to minimize refractive effects. This requirement will be discussed in more detail in the next chapter. For our probe beam, a small fraction of the incident laser beam is split off and passed through two successive frequency doubling crystals. The resulting probe beam has the desired short wavelength (2635 Å), and its timing, relative to the main laser beam, is mechanically fixed. An undesirable property is its harmonic relationship to the main beam, since harmonics are also generated within the plasma[2]. Others have avoided the problem of harmonic light from the plasma by Raman shifting their second harmonic probe beam in alcohol[3]. However, the resulting wavelength is too long for probing to high densities. An approach which deserves more attention is to use a frequency doubled dye laser. A short pulse, non-harmonic ultraviolet probe can be generated; the difficulty lies in synchronizing the probe beam to the main laser.

The theory of optical harmonic generation, by the use of non-linear crystals, is discussed in many modern optics texts. An especially lucid account is given in Yariv[4]. Basically, one requires that the fundamental and harmonic travel through the crystal at the same phase velocity, in order to eliminate interference effects.

Satisfying this requirement is referred to as 'phase matching'. There are two commonly used methods for achieving this, called simply type I and type II. In type I phase matching, the fundamental propagates through a negative (positive) uniaxial crystal as an ordinary (extraordinary) wave, while the harmonic propagates as an extraordinary (ordinary) wave. (A negative uniaxial crystal has one optic axis, and the extraordinary index of refraction is smaller than the ordinary index, at the same wavelength.) In type II phase matching, two fundamental waves are used, one ordinary and one extra-ordinary. Their average index of refraction equals the index of refraction of the harmonic.

For our probe beam system, type II, angle tuned KDP (potassium dihydrogen phosphate) was chosen as the first doubling crystal. It has a high damage threshold, an angular acceptance nearly twice as large as type I KDP[5], and is relatively insensitive to temperature fluctuations. The crystal (1 cm long, 2.5 cm diameter) was mounted in a housing filled with an index matching fluid (FC-104). No temperature stabilization was used; however, the room temperature seldom varied more than one degree centigrade.

The second non-linear crystal doubles the second harmonic to the fourth harmonic, which is in the ultra-violet. Since the dispersion of the crystal is rather

large in the ultraviolet, it is highly desirable to use 90° (type I) phase matching; this maximizes the size of the angular misalignment which can be tolerated[4]. Figure 5 shows the 90° phase matching temperatures and wavelengths for a number of crystals[6]. Deuterated KDP (KD*P) is the best choice for generating the fourth harmonic of Nd:YAG, at 266 nm. However, it requires an impractically low (less than 0 °C) temperature when used with a phosphate glass system (fourth harmonic at 264 nm). Therefore, we used ADP (ammonium dihydrogen phosphate). Using a small phosphate glass oscillator (the diagnostic evaluation laser), the 90° phase matching temperature was determined to be 35.6 °C, in good agreement with Figure 5. The 1.2 cm per side ADP crystal was mounted in a temperature controlled oven, and a piece of KG-3 glass[7] was placed over the entrance window to prevent one micron light from reaching the crystal.

A schematic diagram of the probe beam system is shown in figure 6. Spatial filters[8] are used to improve the beam quality. A 0.5 mm pinhole, located at the focal point of the input lens, passes the zero and low spatial frequency Fourier components, while blocking the high frequency components of the light. These pinholes are in air, not vacuum, and each shot is accompanied by air breakdown in the vicinity of the hole.

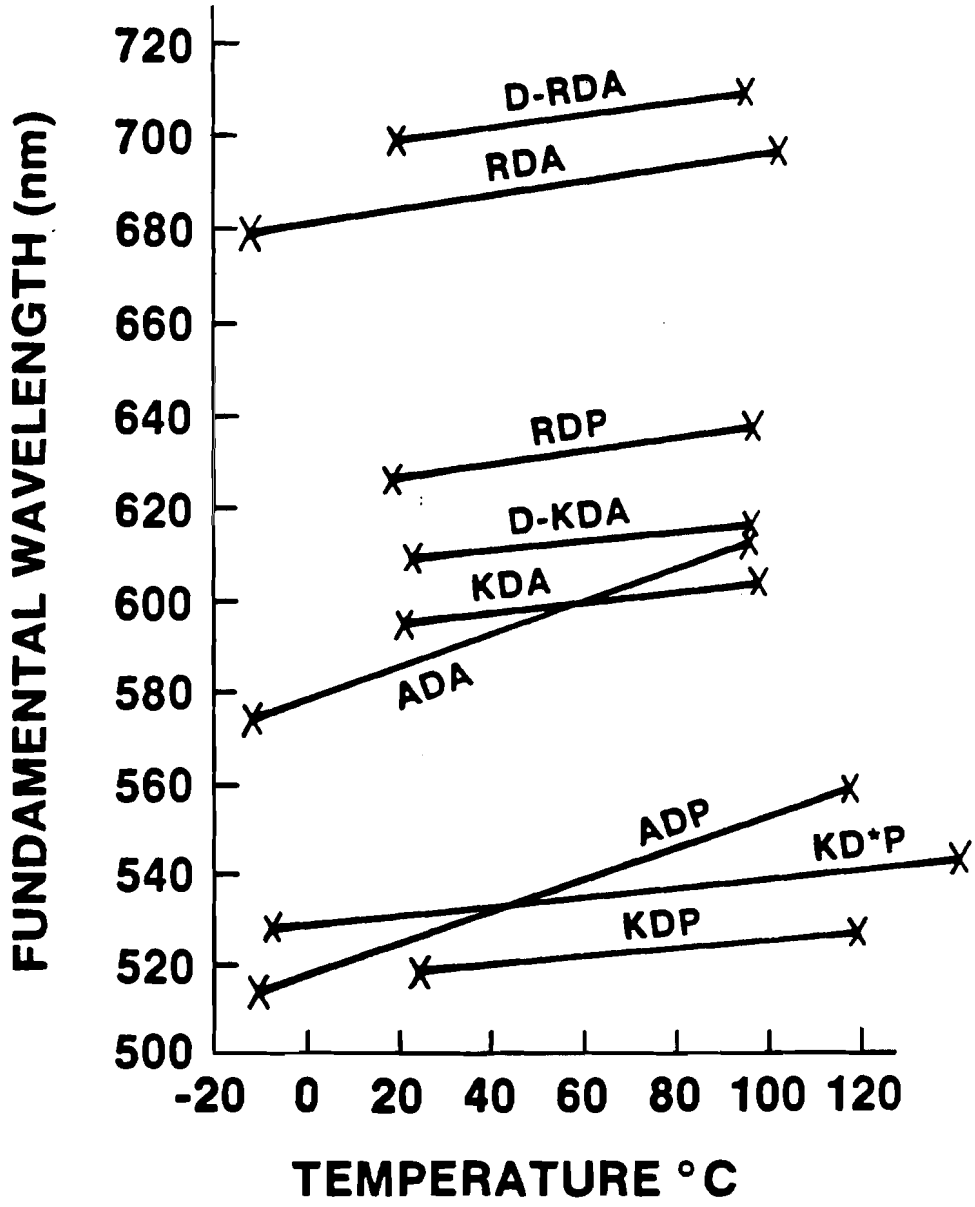

Figure 5. Temperature-Wavelength Relationships For 90° Phase Matching

PROBE BEAM SYSTEM

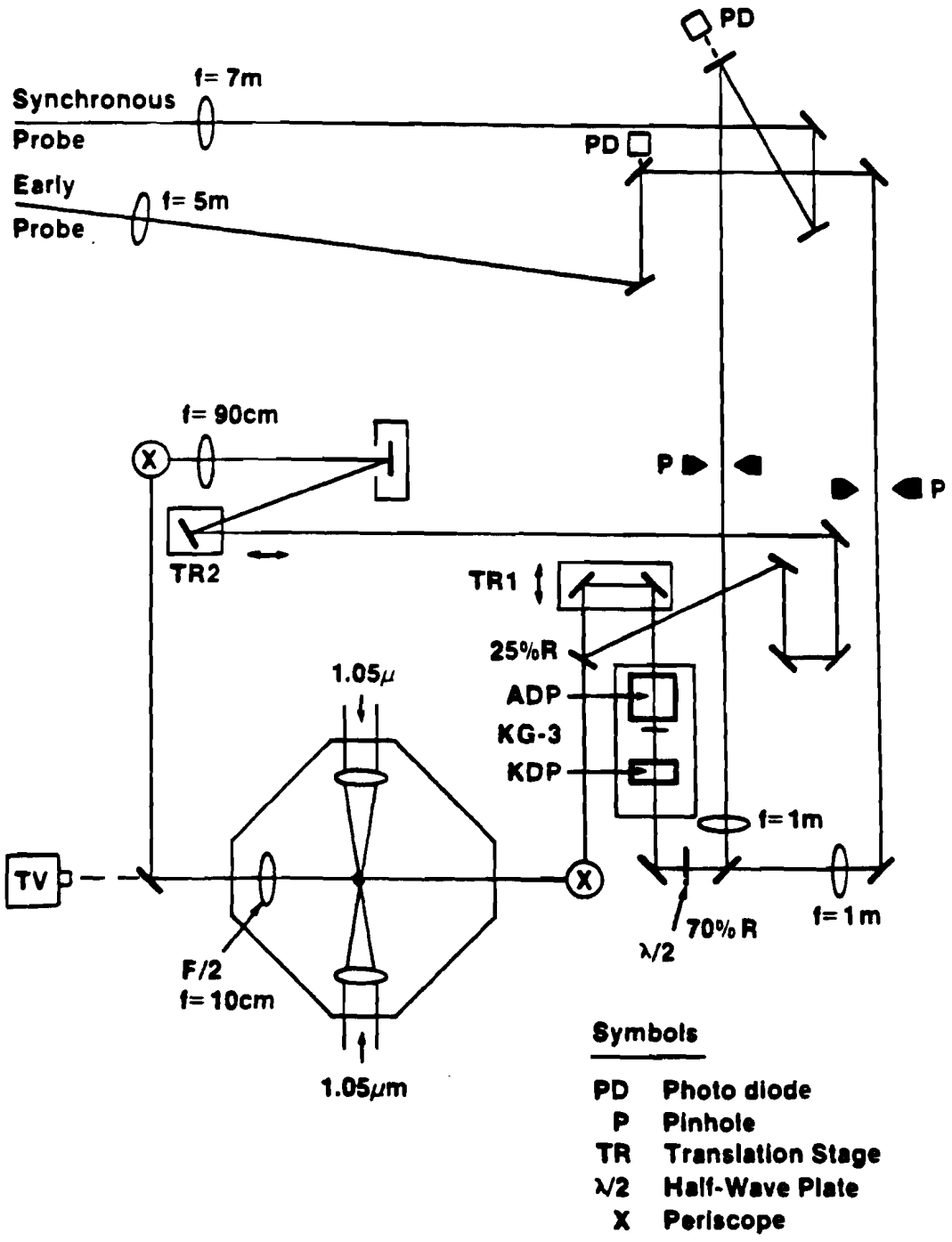

Figure 6

However, this did not appear to have any deleterious effects for our short (60 psec) pulse experiments. If a longer probe were desired, vacuum spatial filters are probably required.

The lenses which are used for the spatial filters simultaneously serve two other purposes. They down collimate the beams to approximately 1 cm in diameter, to match the size of the crystals, and they also relay the image of the beam at the last amplifier to the vicinity of the crystals. This latter function helps to improve the beam quality, by restoring the phase front to its condition at the image location.

The early and synchronous probe beams are combined by a beam splitter just before the crystals, as shown in Figure 6. The system thus produces two ultraviolet pulses, one synchronous with the irradiation of the target, and one approximately 100 nsec in advance of target irradiation. The time of arrival of the synchronous pulse can be varied ±100 psec by moving the translation stage (TR1). All of the non-normal incidence ultraviolet mirrors have dielectric coatings (magnesium fluoride on glass substrates) with high (greater than 95%) reflectivity at 0.26 μm, and low (less than 20%) reflectivity at 0.53 μm. Thus, no filters were necessary in the ultraviolet beam to separate it from the green second harmonic. A beam

splitter (magnesium fluoride on a fused silica substrate) splits off 25% of the ultraviolet beam for use as the reference beam in the holographic system. The remainder is brought up to the vacuum chamber level by a two mirror periscope, and directed to the target. The probe beam, with a diameter of approximately 1 cm, is of course, much larger than the target, and its intensity is low enough that it does not damage the target. A pair of quartz lenses relays the image of the target to the vicinity of the holographic plate. These will be discussed further in the next section. Notice that a second two mirror periscope brings the scene beam back down to table level. Each periscope rotates the polarization by 90°, so that the final polarization at the photographic plate is the same as the original (vertical) polarization. This, of course, is necessary, since to produce the hologram, we must be able to have interference between the scene and reference beams.

We will now discuss the methods used in aligning the probe beam, without an in situ alignment oscillator. As has already been mentioned, the diagnostic evaluation laser was used to determine the 90° phase matching temperature of 35.6 °C for the ADP crystal. The ADP crystal, in its temperature controlled oven, and the KDP crystal, in a gimbal mount, were mounted on an aluminum

plate which was anchored to the optical table by magnetic bases. The plate also had holes drilled and tapped to accept a mirror mount on its front edge. The entire assembly was placed near the output of a Q-switched YAG oscillator. This laser produced 5 watts average power, using a 30 nsec wide pulse and a 5 KHz repetition rate. The laser was aligned to go through the crystals. The angular orientation of the KDP was then varied until the green light produced was of maximum intensity, as measured by a photodiode. The expected[4] $(\sin(\theta)/\theta)^2$ variation in intensity was easily observed. A mirror was then mounted on the aluminum plate, and carefully adjusted to exactly backreflect the laser beam. This mirror marked the proper beam direction through the crystals. The entire assembly of plate, crystals, and mirror was then placed in position in the GDL target chamber area, as shown in Figure 6. The YAG alignment laser was turned on, and the probe beam mirrors adjusted until the beam was exactly retroreflected from the (temporary) mirror on the aluminum plate. Adjustable iris diaphragms were used to mark the proper beam positions. The retro-reflecting mirror was then removed from in front of the crystals. A series of seven low power shots were taken to 'fine tune' the crystal alignment. Only the first three laser rods were fired; this gave sufficient energy

in the 'early' probe beam, and allowed for a repetition rate of 12 minutes per shot. A calorimeter, with a 1 μm blocking filter, monitored the harmonic energy, while the crystal was stepped through a range of 5 milliradians. The full width-half maximum of the harmonic energy was found to be 2 milliradians.

All of the ultraviolet mirrors were roughly aligned with a helium-neon laser. Final alignment was accomplished by 'walking' Polaroid film and cross hairs through the system on a shot to shot basis.

Similarly, the temperature of the ADP crystal was adjusted while observing the ultraviolet output on Polaroid film. Since the conversion efficiency was very low at 35.6 °C, the beam was evidently not orthogonal to the crystal axis. Rather than adjust the beam, the crystal temperature was lowered, and shots were taken and observed on Polaroid film, until a maximum ultraviolet intensity was found. The phase matching temperature used was 32.2 °C. (The temperature controller, which is poorly calibrated, was set at 35.8 °C.)

To match the reference beam optical path length to that of the scene beam, a translation stage, TR2 in Figure 6, is used. As the path length was changed, on a shot to shot basis, the region over which reconstructed images could be obtained was found. This region was

approximately 2 cm long, which indicates that the ultraviolet pulses were of at least 30 psec duration.

Finally, the timing of the synchronous probe was compared to the main heating beams. For this purpose, a Hadland streak camera, with an S-20 photocathode, was placed on the south side of the target chamber, in line with the probe beam exit window. The streak camera was able to detect the small amount of green probe light which was reflected by the dielectric mirrors; it could also easily detect second harmonic light generated within a target plasma by the main laser. The heating beam (only the east beam was used) was attenuated, and several shots were taken. These measurements made it possible to relate the setting of the translation stage (TR1 in Figure 6) to the timing of the probe beam with respect to the heating beam, to within 10 psec. All of the times are measured from the peak of the probe beam to the peak of the heating beam.

The conversion efficiencies, and the energy of the probe beam, were not routinely monitored. The conversion efficiency from 1.05 μm to 0.53 μm, for low energy alignment shots, was typically 5% for 15 mJ of 1.05 μm energy input. For a typical full power shot, 100 mJ of infrared energy was incident on the first crystal in a 1 cm diameter beam, giving an intensity of 2 GW/cm^2; 20% of this energy was converted to the green. No measurement

was made of the ultraviolet energy produced. However, by estimating the sensitivity of the Agfa 10E75 plates, by extrapolation from the literature[9], to be on the order of 100 ergs/cm^2, and attempting to account for all losses, we may make a crude estimate. Such an estimate yields a conversion efficiency of 5% from green light to ultraviolet.

D. Interferometers

Optical interferometry is used to measure the plasma density profile. Since there is considerable refraction of the probe beam in traversing these plasmas, the interferometric system must be capable of accurate imaging. This is discussed in more detail in the next chapter. It is also desirable to have a system which is as compact and stable as possible, because of the difficulties in aligning optics to interferometric tolerances in the ultraviolet.

The folded wave interferometer[10] meets the latter criterion. In this system, the probe beam, after traversing the plasma, is split into two beams. The beams are then recombined in such a fashion that the image of the plasma in one beam overlaps, and interferes with, the image of the nearby vacuum region in the other beam. All of the critical optical components can be

mounted in a compact arrangement, and alignment of the mirrors can be done with visible light. Accurate imaging of the plasma must, however, be verified with ultraviolet light.

Holographic interferometry[11] has a number of advantages[12], the principle one being the ability to easily obtain imaging accuracy. This method of interferometry depends on three of the properties of holograms. First, the reconstructed holographic image contains not only the intensity variations of the original light, but also the phase variations. Secondly, a number of independent holograms can be recorded on the same photographic plate, one on top of the other. Finally, the reconstructed image is three dimensional. It is this last property which enables one to obtain imaging accuracy; since all image planes are contained in the three dimensional reconstructed image, exact focusing can be done after the shot, with a CW, visible light reconstruction. The first two holographic properties mentioned above form the basis for double pulse holographic interferometry. First, a hologram is made of a plane wave in a vacuum (the 'reference exposure'). Then, on the same plate, a hologram of light passing through the plasma is recorded. When the hologram is reconstructed, the images of both the plasma and the plane wave are

simultaneously re-created; where their phases differ, they produce interference fringes.

We chose to use a double pulse holographic system, despite several disadvantages. One must use high resolution photographic plates, which are inherently insensitive; a strong probe beam is required for proper exposures. The interferogram is not available for analysis immediately after the shot; the plate must be developed, the image reconstructed and photographed through a microscope. One needs two exposures for each interferogram. However, the ability to do post-shot focusing outweighs these limitations. In addition, the hologram tends to be less sensitive than other methods to spurious light from plasma emissions, and to blurring due to a rapidly moving plasma. (The ultra-fine holographic fringes on the plate are not formed from the former, and are 'washed out' for the latter, so that they do not reconstruct.) We review the interferometric system in the next section.

E. Double Pulse Holographic System

In our system, the 'early' probe beam produces a hologram of the target, and the surrounding vacuum region, approximately 100 nsec before the target is irradiated by the high intensity 1.05 μm beams. When reconstructed,

the image of the vacuum region is simply a plane wave. The reconstructed light showing the target is, of course, not a plane wave; it has had intensity and phase variations impressed on it by the glass microballoon.

The synchronous probe is used to create a hologram of the plasma formed during the irradiation of the target, or some other (selectable) time. When reconstructed, the light which passed through the plasma is re-created in intensity and phase. The early and synchronous holograms are formed on the same plate, and, when suitably illuminated, both are reconstructed. Fringes appear, showing where the probe beam through the plasma interferes with the early probe through the vacuum. Since the latter image is a plane wave, the interpretation is straightforward; they show the phase variations caused by the plasma. It should be noted that if fringes are observable inside the original target diameter, they are the result of interference between the probe beam through the plasma, and the early probe through the glass; they cannot be easily interpreted, since the effects of the glass are not well characterized.

The schematic layout of the holographic interferometer is shown in Figure 6. The collection lens, located inside the vacuum chamber, is a custom designed[13] F/2, 10 cm focal length triplet. To transmit 264 nm light, its

elements are fused silica. The maximum density which can be observe depends on the amount of refraction in the plasma, and the acceptance angle of the collection lens. Numerical simulations, which will be discussed in more detail in the next chapter, indicated that for a typical plasma (100 μm diameter, exponential density scale length of 10 μm), an F/2 collection lens is required in order to probe to the critical density.

Another effect of the refraction is that the (refracted) light from the synchronous probe will strike the imaging lens near its edge, while the (unrefracted) light in the early probe beam will be incident very nearly on axis. This means that the lens must be well corrected for spherical aberration. It is sometimes stated[11] that, with double pulse holography, errors due to poor optics 'cancel out'. This is only true in the absence of refraction.

The spherical wavefront aberration of the F/2 triplet was measured by the manufacturer using visible (6328 Å) light, with a (calculated thickness) corrector plate. From this measurement, it was inferred that the spherical aberration in the ultraviolet was less than one-sixth of a wavelength[14].

This lens is used with a second quartz lens (F/18, 90 cm focal length) to form a relay pair with 9X

magnification. It was pointed out earlier that the holographic system frees us of the need for exact focusing prior to collecting the data. There are, however, two limitations to this statement. The lens must be used close to its design parameters(infinite conjugate ratio) if its performance is to fall within its specifications. The other constraint is due to the quartz vacuum window. This window will produce spherical aberration unless the image is focused at infinity. Fortunately, a simple estimate shows the spherical aberration to be negligible for focusing errors of 1 mm or less (conjugate ratios of 100 or more). This degree of accuracy is easily achieved, as follows. The holographic plate is positioned approximately 89 cm from the 90 cm focal length lens. If the F/2 lens is properly focused, therefore, the image of the target should appear 1 cm behind the plate. A hologram is made, and the image location is observed. If it is not 1 cm from the plate, the collection lens is adjusted, and the procedure is repeated. It should be noted that since the longitudinal magnification is 81, (the lateral magnification squared), an error of 1 cm in locating the image (highly unlikely) produces an uncertainty of only 0.12 mm in the focusing of the collection lens.

The holographic camera consists simply of a

photographic plate holder, surrounded by a light-tight box with a four inch diameter, electrically operated shutter. The shutter is activated from the GDL control room. A small photodiode is used to send a signal to the control room, to indicate whether or not the target area room lights are off.

The photographic plates we use are Agfa 10E75 NAH, nominally 4 by 5 inches. They are considerably more sensitive than needed for this application. Since we lacked high optical quality ultraviolet attenuators, it was decided to reduce the film speed rather than attenuate the beam. (We could not reduce the probe beam intensity before the target without decreasing the signal to noise ratio.) To accomplish this, the D-19[15] developer was diluted 1:1 with water, and an anti-fog agent[16] was added at twice its recommended strength[17]. For a typical shot, the plate was developed for two minutes at 20 °C. This time was adjusted if the intensity for that shot was unusually weak or strong. In lieu of an acid stop bath, a running water bath was used to halt development. Next, the plate was bathed for two to four minutes in Rapid Fixer[15], then washed for five to ten minutes, followed by drying in air. The hologram was then ready for reconstruction.

The reconstruction apparatus is shown in Figure 7.

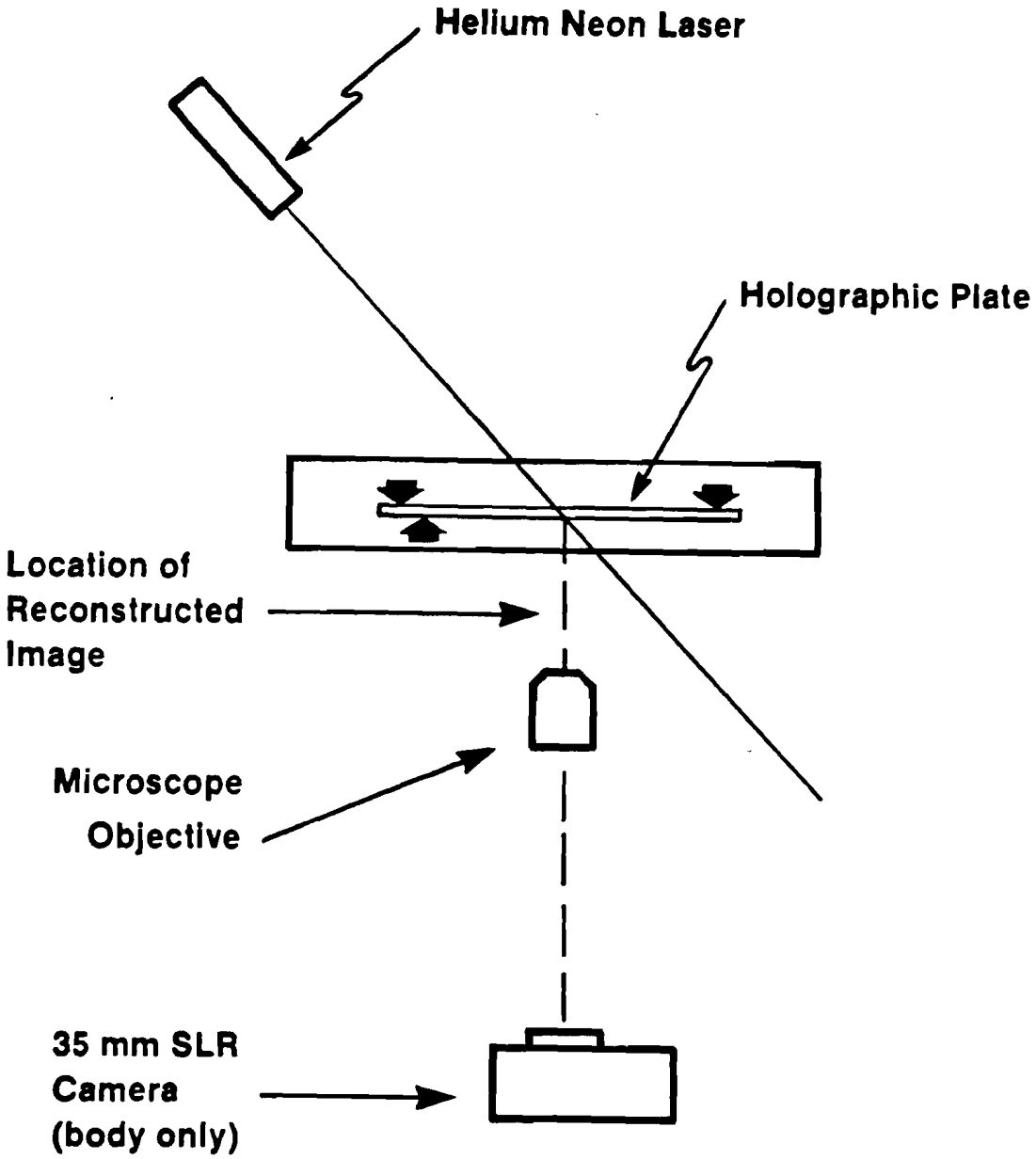

Figure 7. Holographic Reconstruction Apparatus

A 0.5 mW helium-neon laser is used to illuminate the hologram. The reconstructed image is magnified by a 5X microscope objective, which relays the image onto the film plane of a 35 mm single lens reflex camera body. The microscope objective is adjusted to produce a sharp image of the target support stalk. (The desirability of focusing at the mid-plane of the target will be discussed in the next chapter.)

Individual holograms varied considerably in the brightness of the reconstructed image. Typically, however, an exposure time of one second on Tri-X[15] film (ASA 400) was required. After processing, the 35 mm negatives were used to produce large prints, from which the data could be directly digitized.

The data reduction and error analysis for the interferometric data will be reviewed in chapter IV.

F. Calorimetry

The Beta target area uses four thermoelectric calorimeters (Scientech Model 3-80101) to monitor the incident east and west beam energies, the backscattered energy, and any energy transmitted around or through the the target. These are shown in Figure 4. The incident energy calorimeters measure the amount of light which is reflected from the uncoated vacuum chamber windows.

To understand the functioning of the backscattered and transmitted light calorimeters, it is necessary to review the polarization present at various points along the optical path. The light from the laser is vertically polarized ('S'). On passing through the quarter-wave plates it becomes right circularly polarized (see Figure 4). Light which misses the target travels down the opposite beam line. The quarter-wave plate in that beam line changes the polarization back to vertical. The light travels back to the 50% reflecting beamsplitter, where half of it is sent down the dotted path shown in Figure 4. The polarizer directs this light to the 'S' calorimeter, where its energy is measured.

Now consider light which hits the target. If this light is specularly reflected, or undergoes Brillouin backscattering, its polarization is changed from right to left circular. On passing through the quarter-wave plate, it is converted to horizontal polarization ('P'). The beamsplitter directs some of this light through the polarizer, to the 'P' calorimeter (and also to the spectrometer). It should be noted that, for 'P' polarization, the beamsplitter is ~65% transmitting, and ~35% reflecting. Therefore, the 'P' calorimeter is more sensitive to backscatter from the west beam than from the east beam.

The calorimeters were all calibrated in situ against a large (six inch diameter) reference calorimeter by firing a number of low power laser shots, with the reference calorimeter taking the place of the target. A high reflectance mirror, inserted in one beam line at a time, was used to calibrate the backscattered and transmitted light calorimeters. The reference calorimeter was calibrated using an internal electrical resistance as a heat source. The relative calibration between the incident energy calorimeters and the backscatter calorimeter was periodically checked by firing a low power shot off of a retroreflecting mirror placed in the beam line. The calibrations used are shown in Table I. Notice that, as previously mentioned, the backscatter calorimeter is more sensitive to the west beam than the east. The calorimeter signals are each fed into an amplifier and a hold circuit, and are read out on digital voltmeters. The hold circuits have a decay time on the order of 0.01 volt/sec. The voltmeters are manually latched within a few seconds after the shot, ensuring read out accuracies of 20 to 30 millivolts. For a typical shot, (10 Joules on target, 10% backscatter), this results in relative backscatter error bars of 3%. Subsequent calibration shots showed fluctuations on the order of 6%, presumably due to small misalignments and/or electrical

Table I

Calorimeter	Calibration (Volts/Joule)
East Beam	0.415
West Beam	0.556
Transmitted ('S')	0.89*
Backscattered ('P')	
Both Beams	0.90
West Beam Only	1.17
East Beam Only	0.63

*To correct for 'P' reflections off of the polarizer, 8% of the 'P' reading, in volts, is subtracted from the 'S' calorimeter reading, before applying the 0.89 V/J calibration factor.

noise. Thus the error bars for the backscatter fraction are typically 10% of the fraction.

The transmitted energy calorimeter showed negligible energy getting by the target, except when the beams were greatly defocused.

G. Backscatter Spectroscopy: Time Integrated

A portion of the 'P' polarized backscattered light is directed to a one meter focal length Czerny-Turner grating spectrometer[18], as indicated in Figure 4. It is easily shown[19] that the resolving power of a grating, $\lambda/\Delta\lambda$, is equal, in first order, to the total number of lines illuminated. This assumes, of course, that all of the grating lines are continuously illuminated, and can therefore interfere with each other. For short pulses, the effective size of the grating is limited to those optical path differences which are less than the pulse width. This limitation, which will be elaborated on in the next section, can be expressed as

$$\Delta\nu \cdot \Delta\tau = 1 \qquad (63)$$

where $\Delta\nu$ is the smallest resolvable frequency difference, and $\Delta\tau$ is the pulse width. A practical resolution limit is often imposed by the finite size of the entrance slit.

The spectrometer uses a 5 cm wide, 1200 lines/mm grating. For our time-averaged studies, this grating was

fully illuminated, giving a possible resolution of $\Delta\lambda = 0.2$ Å at $\lambda = 1.05$ μm, in first order. However, the pulse width of 60 psec constrains the effective size; equation (63) yields $\Delta\lambda = 0.6$ Å. The input slit was set at 100 μm width. Since the dispersion at 1 μm is 7 Å/mm, the slit limits the resolution to $\Delta\lambda = 0.7$ Å. Taking the r.m.s. average yields the resolution $\Delta\lambda = 1$ Å.

The spectrometer is aligned with the aid of the GDL YAG alignment laser. The target is removed, and the light allowed to propagate down both the east and west beams. One of the quarter-wave plates is rotated 90° ; as a result, the light traveling through the target chamber and back the opposite beam line is horizontally ('P') polarized. A fraction (~10%) of this light is focused onto the spectrometer entrance slit by an 8 cm focal length cylindrical lens. The spectrometer output is viewed in the film plane with the aid of a ground glass and an infrared viewer. The viewer is also used to confirm that the grating is fully illuminated.

When alignment is complete, the ground glass is replaced by a film holder containing a 4 by 5 inch sheet of High Speed Infrared[15] film. The film is exposed to the YAG laser light for several seconds, to furnish a reference line for use during analysis. When this is completed, the wave plate is returned to its original

position, and the spectrometer is ready to record the backscatter spectrum.

After the data shot, the film is developed in D-19[15] to yield a film gamma of approximately one. A microdensitometer is then used to generate a plot of film density versus wavelength.

To calibrate the dispersion of the system, a retro-reflecting mirror was inserted into the west beam, and a low power shot was taken. The resulting densitometer trace, shown in Figure 8, shows the glass laser line at 1.054 μm, and the YAG line at 1.064 μm. The measured dispersion is 7 Å/mm.

H. Backscatter Spectroscopy: Time Resolved

To record time resolved backscatter spectra, it was necessary to modify the system described in the last section. In a grating spectrometer, the optical path length of a light ray diffracting off of any given groove differs by one wavelength (in first order) from the path of a ray diffracting from the adjacent groove. As more grooves, or grating lines, are illuminated, the light is spread out in time. Therefore, the temporal resolution degrades in proportion to N, the number of lines illuminated. Recalling that the spectral resolution is inversely proportional to N, it is straightforward to

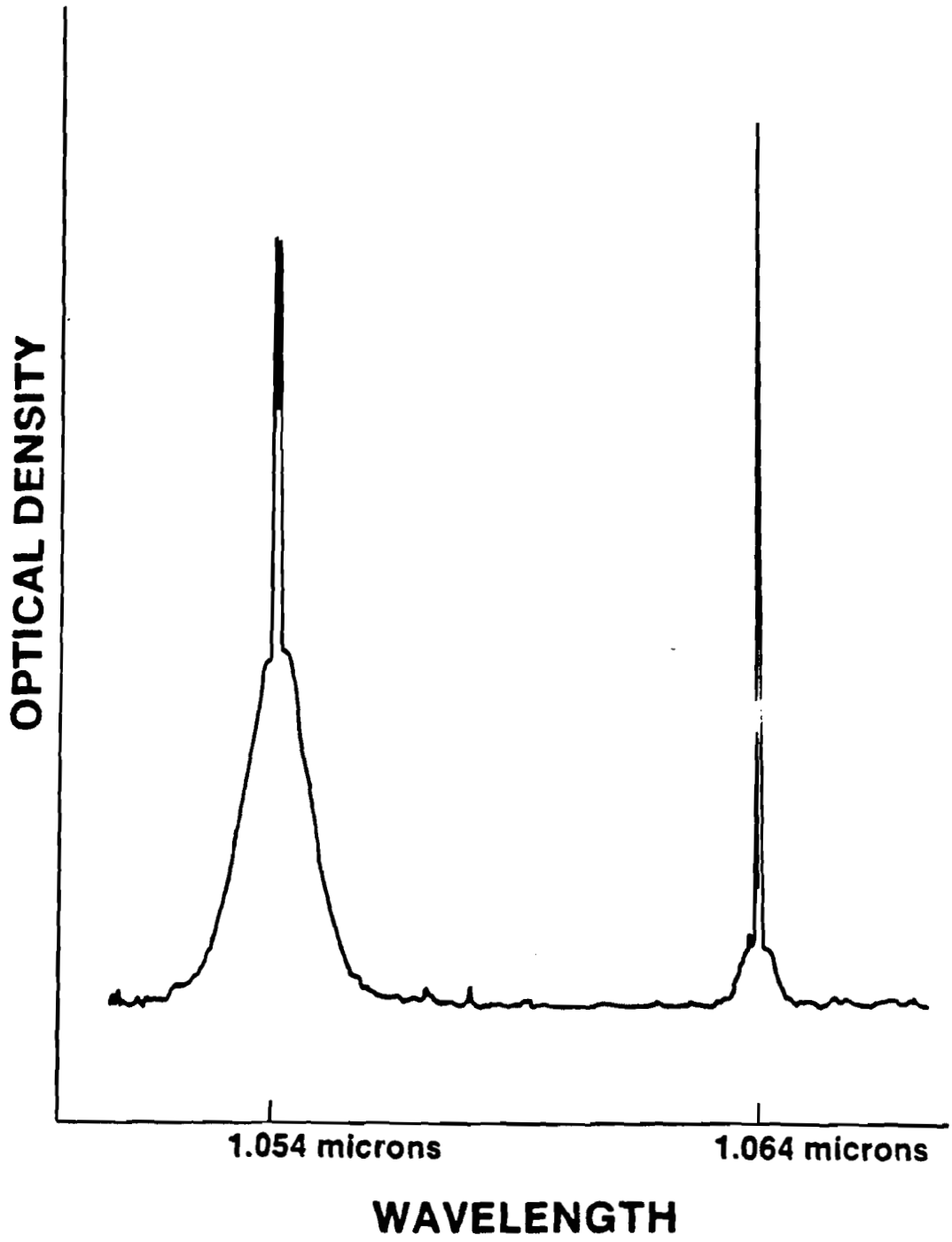

Figure 8. Spectrometer Calibration Lines

derive equation (63) in the previous section. As an example, if a temporal resolution of 10 psec is desired, equation (63) shows that the spectral resolution must be limited to be no better than 3.7 Å, at our laser wavelength of 1.05 μm.

The cylindrical lens was removed from the spectrometer, and a very long (5 meter) focal length lens used instead, to focus the light onto the input slit. This is shown in Figure 9. The high F number input resulted in illumination of only 2.5 mm of the grating. The corresponding spectral resolution is 3.5 Å; the temporal dispersion of the spectrometer is then 10.6 psec. The entrance slit was set at 400 μm, which would limit the resolution to 2.8 Å if the grating were fully illuminated.

The spectrometer output is relayed to the input slit of a streak camera[20] by a prism and a 10 cm focal length lens, with a magnification of 0.5. The prism rotates the image of the spectrometer slit, so that it is orthogonal to the streak camera slit. The system was sufficiently sensitive to detect light from the GDL oscillator. As described for the YAG earlier, one quarter-wave plate is rotated 90°, and the target removed, so that the light transmitted through the chamber becomes horizontally polarized, and is directed to the spectrometer. Since the oscillator can be fired once every 10 seconds,

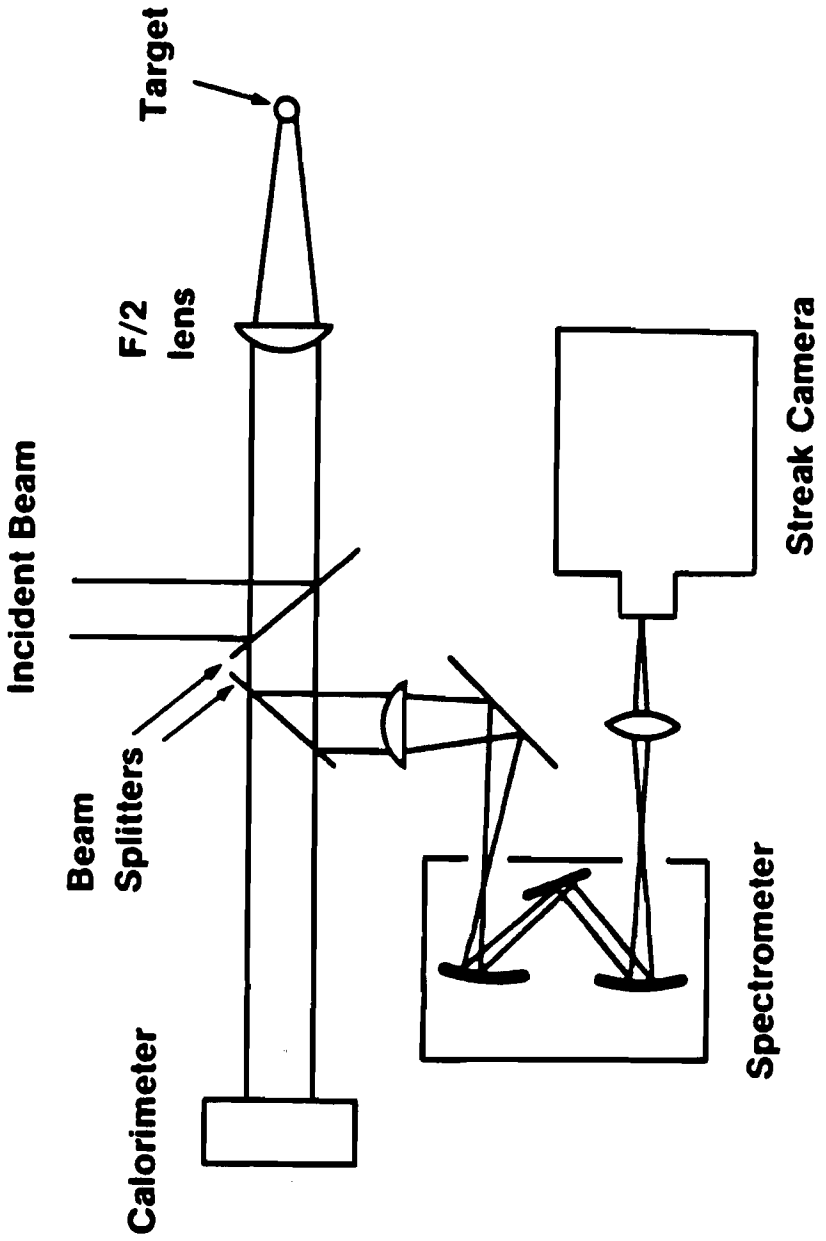

Figure 9. Layout For Time Resolved Backscatter Spectra

this greatly facilitates the timing of the streak camera. The streak camera trigger was furnished by a p-i-n photodiode, positioned to see a small part of the 'early' probe beam.

The system was spectrally calibrated using the YAG laser. The spectrometer grating was set to a center wavelength of 10630 Å, the streak camera turned on in the focus mode, and an exposure of about 3 seconds duration was made. The grating was then advanced to 10640 Å, and another exposure taken; this was repeated at 10650 Å, and at 10660 Å. This resulted in reference marks spaced 10 Å apart on the developed film. A densitometer trace of these calibration marks is shown in Figure 10. The grating drive is known to be very accurate, and the change in the dispersion is negligible.

The spectrometer was set at 10550 Å for data shots. Several low power shots were taken with a retroreflecting mirror in the beam, to calibrate the position of the laser line on the film. (This position can also be calculated from the YAG calibration data; this yields the same result.)

An etalon (5 cm thickness, 70% reflecting on each end) was inserted in the backscatter beamline, before the spectrometer. This gave a series of pulses, 500 psec apart, and each reduced in intensity by a factor of two from the preceding one, which can be used to calibrate

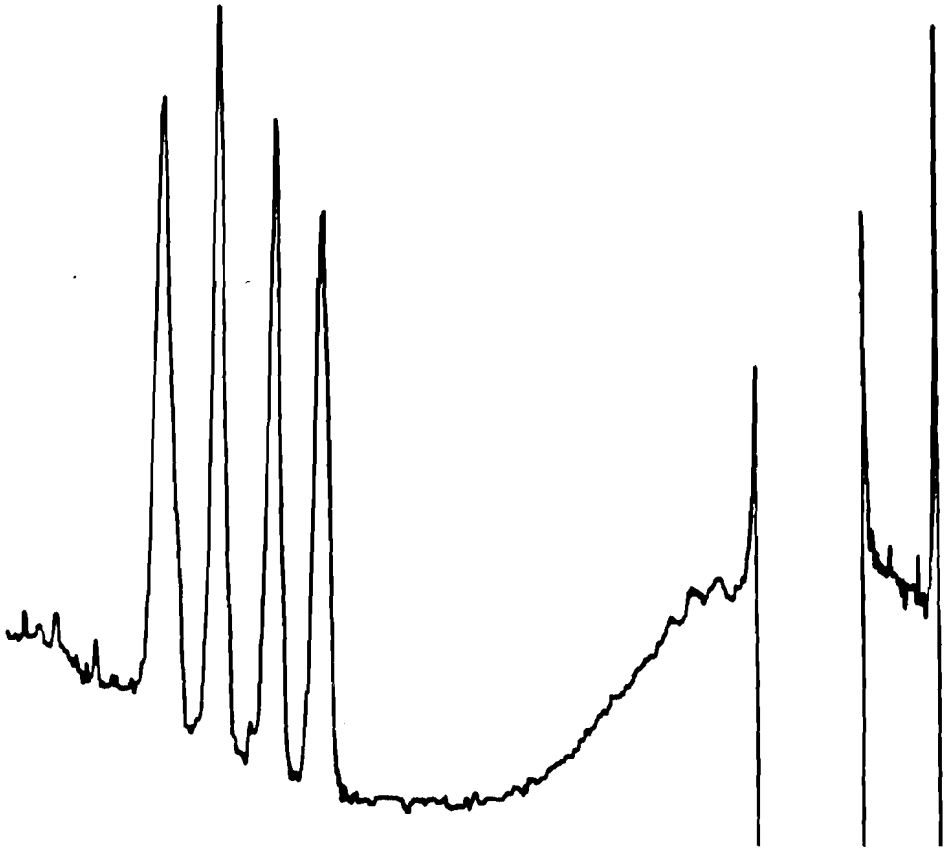

Figure 10. Time Resolved Spectra Calibration Lines (Sharp lines on the right are from the film edge and a sprocket hole.)

the streak speed. The measured speed, averaged over 1 nsec at the center of the streak, is 64 psec/mm. In reducing the data, a pulse near the center of the streak is always used, since the spectral dispersion has been calibrated only in that region. Fortunately, the etalon pulse appearing closest to the center almost always provided the best film exposure as well (in the range of 1.5 optical density). A close examination of Figure 10 shows that there is some distortion (~15%) present, presumably due to pin-cushion distortion in the image intensifier. When the data is presented in chapter V, the figures will show linear (uncorrected) wavelength scales; wavelengths quoted in the text, however, have been corrected for the intensifier distortion. The correction consists of linear interpolation between the calibration lines shown in Figure 10, and linear extrapolation beyond them. The numbers used are: 6.7 Å/mm for $\Delta\lambda$ between zero and 10 Å; 7.8 Å/mm between 10 Å and 20 Å; and 7 Å/mm for $\Delta\lambda$ greater than 20 Å, where $\Delta\lambda$ is the red shift from the incident wavelength.

In order to determine the absolute wavelength, it is necessary to measure from the edge of the film; i.e., the accuracy is limited by the repeatability of the mechanical film transport mechanism. We estimate the tracking accuracy to be better than 0.5 mm, which

corresponds to 3 Å. Shots where a beam was retro-reflected, for calibration purposes, show a variation of less than 2 Å in their position from the bottom edge of the film.

In summary, the time resolved backscatter spectroscopy is capable of 15 psec time resolution (including 10 psec for the streak camera's resolution), and 4 Å spectral resolution. The relative calibration of wavelength, limited by uncertainty in the image intensifier distortion, is ±2 Å for red shifts of zero to 20 Å, and somewhat larger (estimated at ±3 Å) for larger red shifts. The absolute calibration of the wavelength is limited by the mechanical film transport to approximately 2 Å. Finally, the streak speed was measured to average 61.7 psec/mm in the 500 psec before the data, and 67.2 psec/mm in the 500 psec after the data, giving an average streak speed of 64 psec/mm, with a variation of ±5%.

IV. DATA REDUCTION

A. Abel Inversion

We will now review the theory relevant to the interpretation of interferometric data in refracting media.

For the case of negligible refraction, illustrated in Figure 11, the results are well known[1]. Two coordinate systems are shown: cartesian (x,y,z) and cylindrical (r,ϕ,z). In order to interpret the data, it is necessary to impose a symmetry requirement. In particular, it is assumed, in all that follows, that the index of refraction is independent of the coordinate ϕ; i.e., there is a rotational symmetry about the z axis. Now, an interferometer will measure the phase of the probe beam which goes through the medium, compared to a reference beam through vacuum. That phase difference is given by

$$F = (1/\lambda) \int_{-\infty}^{\infty} |\mu(x,y,z) - 1| \, dx \qquad (64)$$

where F is the phase difference, expressed in fraction of a wavelength; μ is the index of refraction of the medium; the index of the vacuum is, of course, one. Changing to cylindrical coordinates, and using the symmetry assumption, we have

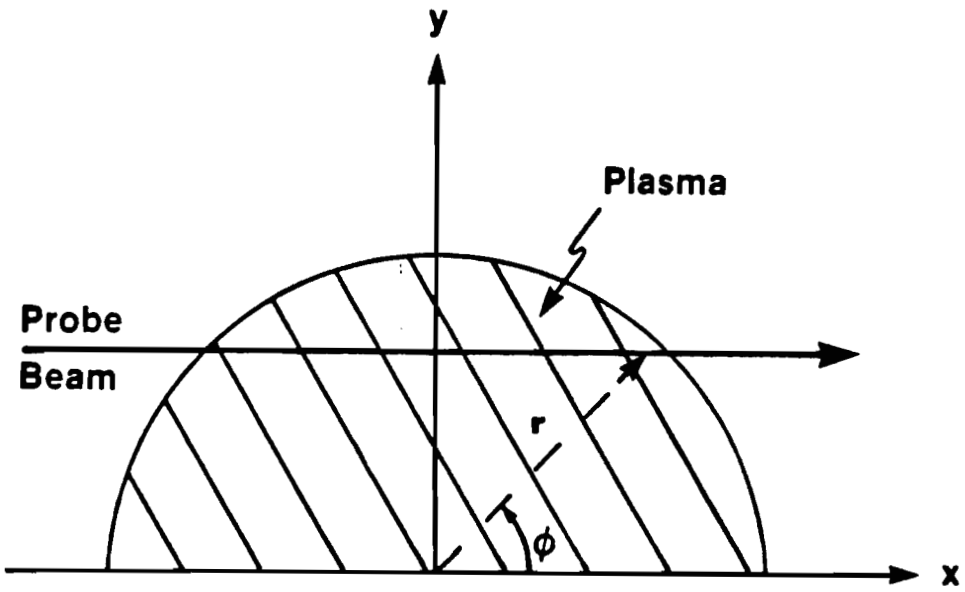

Figure 11. Coordinate System For Abel Inversion

$$F = (2/\lambda) \int_y^\infty |\mu(r,z) - 1| (r^2 - y^2)^{-0.5} r \, dr \qquad (65)$$

This equation has a well known[1] inversion, named after Abel:

$$|\mu - 1| = -\frac{\lambda}{\pi} \int_r^\infty \frac{dF}{dy} \frac{1}{\sqrt{y^2 - r^2}} \, dy \qquad (66)$$

The index of refraction of a plasma is given by

$$\mu = ck/\omega = (1 - \omega_p^2/\omega^2)^{0.5} = (1 - 4\pi e^2 n/m\omega^2)^{0.5} \qquad (67)$$

where n is the electron number density, ω_p is the electron plasma frequency, and we have ignored corrections due to magnetic fields and damping as they are small[2]. Since the plasma frequency depends only on the density, and the index of refraction depends only on the plasma frequency, the density is uniquely determined if one knows the index of refraction. From equation (66), it is clear that the index can be determined by an interferometric measurement of F, the phase difference.

B. Refractive Effects

In order to investigate refractive effects, a numerical simulation was developed. This work is similar to that done by Sweeney[3]. For simplicity, a spherically symmetric plasma was modeled. An HP 9830 calculator program was written to ray trace a probe beam through the

plasma, using Bouger's Law; $\mu r \sin(\theta) = \text{constant}$, where μ is the index of refraction, r the spherical coordinate, and θ the angle between r and the ray direction. The program calculates the true optical path length of the ray, and calculates the fringe pattern generated by an interferometer, assuming an ideal lens is used for the imaging. This fringe pattern is then used as data, and is Abel inverted using equation (66); i.e., as if there were no refraction. A typical result is shown in Figure 12. The discrepancy between the 'actual' density and the 'measured' density is due to the refraction: an ideal lens images the light along a straight line, while the actual path is curved. This is illustrated in Figure 13. The fringe pattern used to calculate the density in Figure 12 was obtained by imaging the mid-plane of the plasma.

When the image plane is (numerically) moved by more than ten micrometers, the error in the measured density grows larger, as shown in Figure 14. This is especially true when the image plane is moved in the direction away from the lens (toward negative x in Figure 13). This can be understood with the help of Figure 13. For mid-plane ($x = 0$) imaging, the imaged refracted ray is compared with the 'wrong' unrefracted (reference exposure) ray, one which is slightly too low. When the image plane

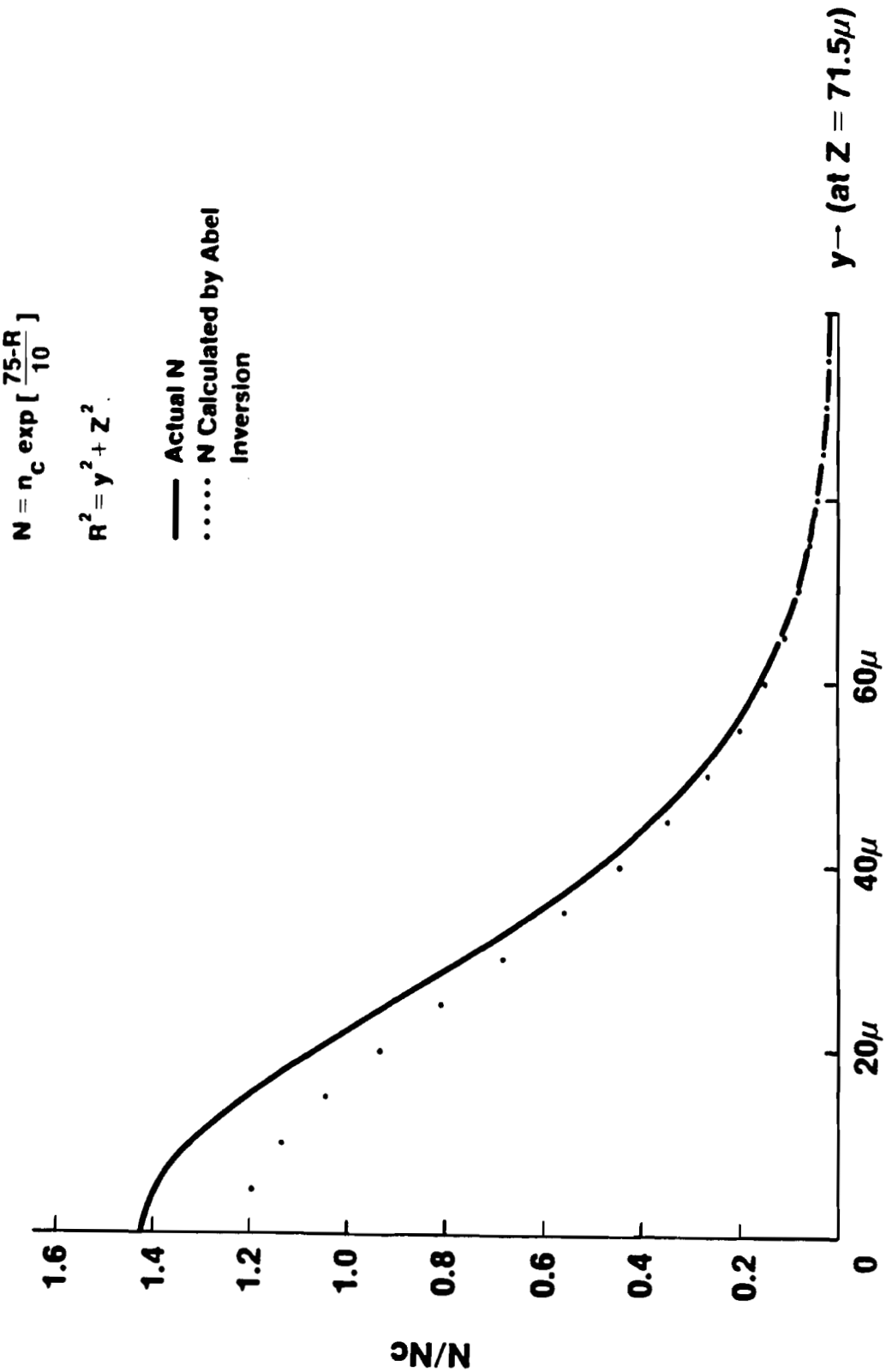

Figure 12. Numerical Simulation Showing Refractive Effects

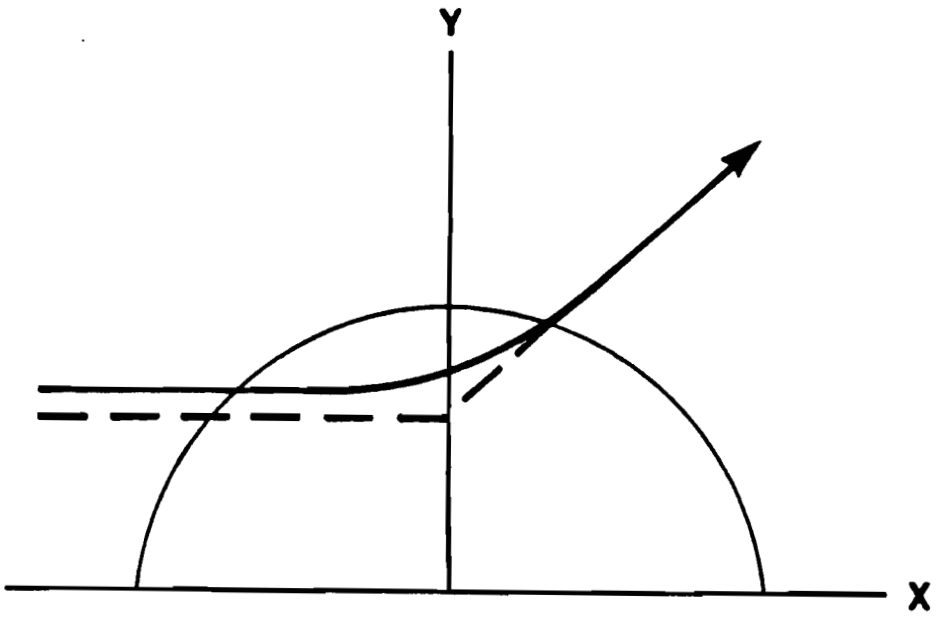

Figure 13. The Effects of Refraction (solid line) and Imaging (dotted line)

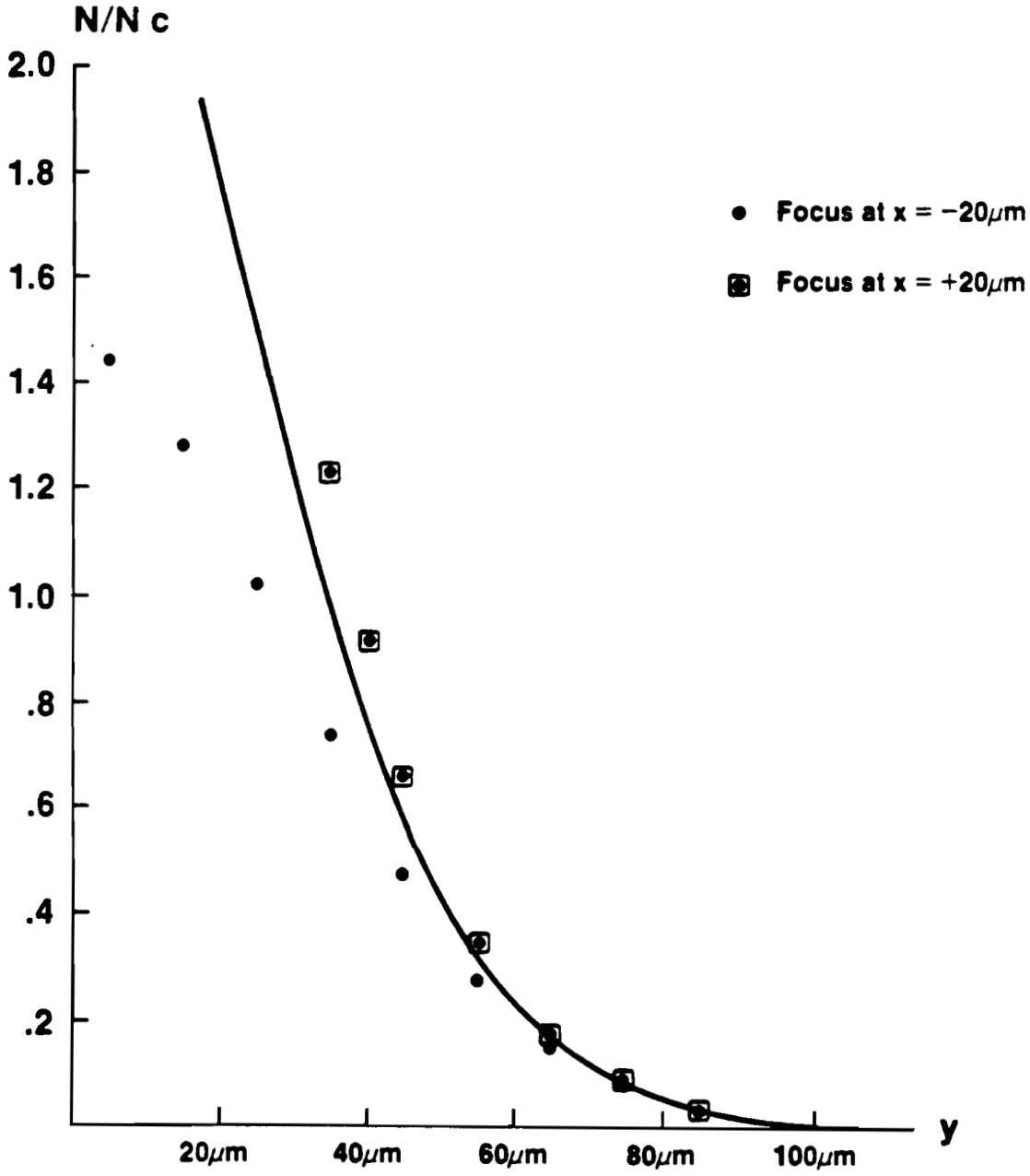

Figure 14. Simulation of Focusing Errors
(Solid line shows 'actual' density)

is moved toward negative x, this effect becomes worse. When moved toward positive x, there is a point where the refracted ray is imaged to nearly the same height (y coordinate) as it had originally, and the error due to the curved path is canceled. The numerical studies show this position to be between x = 0 and x = 10 micrometers for typical plasmas. The ability to compensate for refractive errors has been discussed by others[4]. Unfortunately, this requires an a priori knowledge of the plasma density profile. A number of researchers have attempted to produce codes which would determine the proper focal position iteratively; however, these programs usually do not converge properly without (subjective) operator involvement[4]. If the image plane is placed at still larger positive x, the error again grows. Thus, if the focal plane is continuously varied, the interferometric fringes vary continuously also; only when imaged near the mid-plane (x = 0) can they be correctly interpreted, however. The desirability of focusing at the mid-plane has been pointed out by others[2]. This requirement is, as mentioned before, the main reason for choosing to do the interferometry holographically, since accurate focusing (on the target stalk) can be easily obtained and verified.

C. Numerical Data Reduction

In this the section, the numerical methods used to invert the interferometric data will be reviewed. The actual FORTRAN programs used will be published separately.

An enlarged copy of the interferogram is placed on a Hewlet-Packard 9862A digitizing table. A cylindrical coordinate system is placed on the interferogram, with the z axis lying along the incident laser beam, perpendicular to the target support stalk. Lines are drawn in the r direction (orthogonal to z), wherever a bright or dark fringe intersects the z axis. The fringes are consecutively numbered, in units of wavelength difference; the outermost dark fringe is 0.5, the next bright fringe is 1.0, the next dark fringe is 1.5, etc. The digitizer cross-hair is moved along the lines; it records the coordinates (r,z) wherever a fringe intersects the line. The fringe number is simultaneously noted. Thus, a finite number of data points are accumulated for each line: $\left(F(r_1,z_1)=0.5,\ F(r_2,z_1)=1.0,\ \ldots,\ F(0,z_1)=5.0\right)$, for example, where F is the fringe number at (r,z), and r_1, r_2, ..., 0, are the radial coordinates where the first fringe, second fringe, etc., intersect the line drawn at $z=z_1$. These points are plotted in the example shown in Figure 15.

If the fringe number function F(r,z) were known for all values of r for a given z, the inversion would be straightforward. Recall the Abel inversion equation for the index of refraction, from section A:

$$|1 - \mu| = \frac{-\lambda}{\pi} \int_{r}^{\infty} \frac{dF(y,z)}{dy} \frac{1}{\sqrt{y^2 - r^2}} \, dy \qquad (66)$$

Clearly, if F is accurately known, the integral can be done. In practice, there are two problems. First, F is known only at a finite number of points; secondly, small errors ('noise') in the function F may produce large fluctuations in the value of $\frac{dF}{dy}$. This latter problem requires that some sort of smoothing or filtering be done. A third problem is that the exact form of the function F is unknown for values of r greater than the radius of the first dark fringe (F=0.5). In all of the numerical routines, F is assumed to be a Gaussian for large r. The Gaussian is chosen to smoothly match the data curve fit at the last (F=0.5) data point. While this choice is arbitrary, it can be seen, by examination of equation (66), that its effect on the density near the z axis is small, since the term $(y^2 - r^2)^{-0.5}$ in the integrand will be small in the region (large y) where F is represented by the Gaussian.

The data reduction program, which is listed in the

Appendix, operates in the following manner. The data points are called from storage, in symmetric pairs (i.e., $F(r,z)=F(-r,z)$). A cubic spline curve is fit through all the points, and a Gaussian is fit onto the 'tail' of the function ($F<0.5$). These analytic functions are then used in equation (66); the integrals are evaluated, and the density calculated, for values of r ranging from 1 to 80 microns, in one micron steps. A cubic spline smoothing routine is then applied, to take the noise out of the inversion. This routine leaves the on-axis ($r=0$) density unchanged. In order to be certain that the curve fit accurately represented the function $F(r,z)$ for small r (near the z axis), data was reduced only along lines of constant z such that $F(0,z)$ was, in fact, a data point. The curve fit, therefore, is interpolation only; no extrapolation is necessary. Examination of equation (66) shows that the value of the density on the z axis is most sensitive to the function $F(r,z)$ for small values of r. The program plots the data, the curve fit, and the density (all versus the cylindrical radial coordinate r).

As a test case, we assumed the fringe function to be given by

$$F = 5 \exp(-\beta r^2) \qquad (68)$$

where $\beta = 0.0017675\ (\mu m^{-2})$

The Abel inversion, equation (66), can be done analytically for this function (a Gaussian), yielding

$$|1 - \mu| = 5\lambda(\beta/\pi)^{0.5} \exp(-\beta r^2) \qquad (69)$$

where, as before,

$$\mu = \sqrt{1 - n/16n_c} \qquad (70)$$

Equation (68) was used to calculate the 'data points'; i.e., those values of r where F = 5, 4.5, 4, ..., 1, 0.5. These points were entered into the numerical reduction code. The results are shown in Table II, and in Figures 15 and 16, along with the 'actual' density calculated from equations (69) and (70). As can be seen, the code reproduces the assumed density to within one half of a percent.

A second reduction code was used to verify the results of the code just described, and to investigate the effects of smoothing the data before doing the Abel inversion. This program fits, in a least mean square sense, a second, fourth, or sixth order polynomial to the data. As before, a Gaussian is used to model the tail of the function. Naturally, as a higher order is used, the fit becomes better, while the smoothness (fluctuations in the derivative) becomes worse. Instead of a polynomial, a simple Gaussian can also be least mean square fit to the data. The actual function and order used are subjectively chosen as being the ones which give the best

TABLE II

Results of Test Case

Radius (μm)	1	5	10	20	30
'Actual' Density $\left(\frac{n}{n_c}\right)$	0.983	0.942	0.827	0.489	0.203
Calculated Density $\left(\frac{n}{n_c}\right)$	0.978	0.945	0.827	0.490	0.203

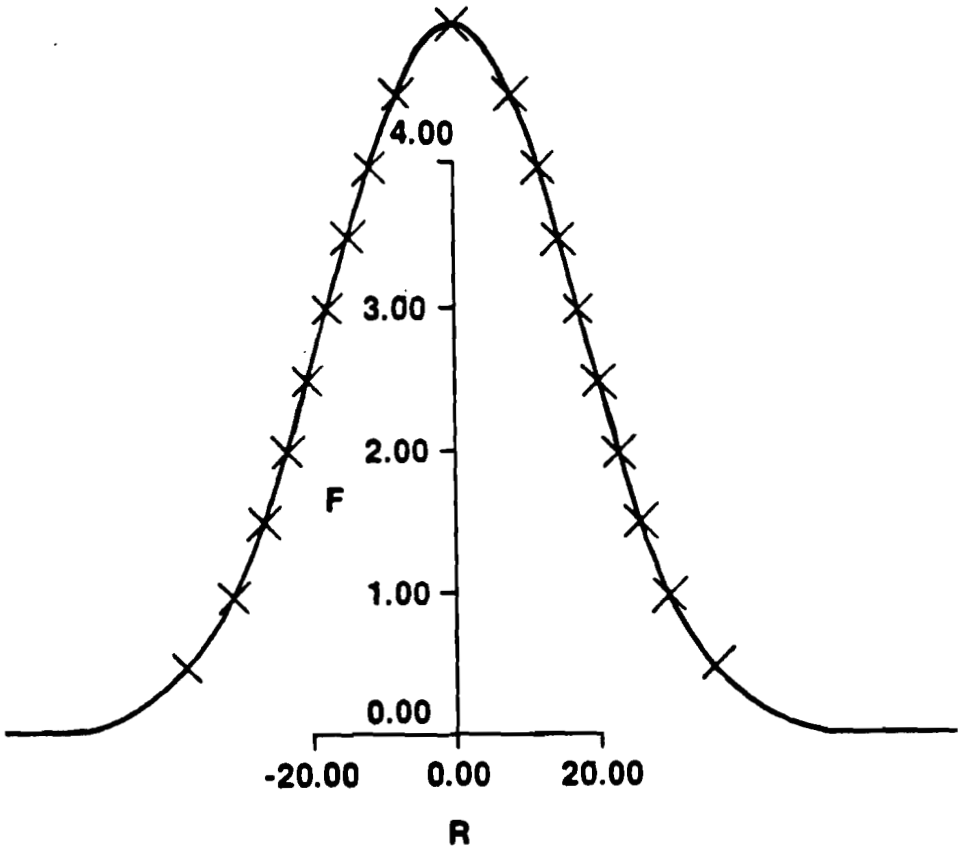

Figure 15. Plot of Fringe Data and Spline Fit

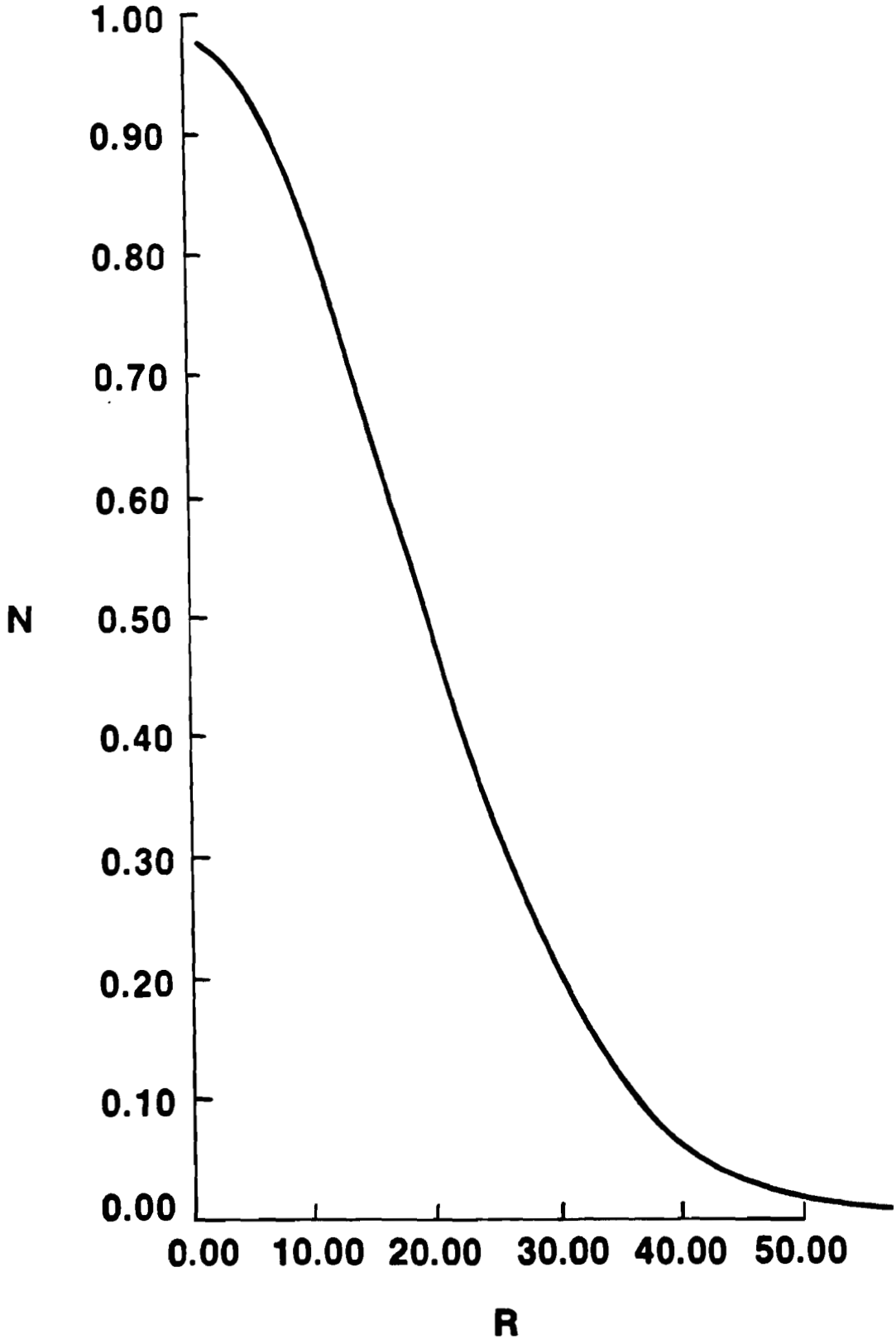

Figure 16. Abel Inversion of Data in Figure 15

f t to the data. The results are compared with those obtained using the spline fitted data. Density differences between the two are reflected in the error bars; the differences were found to exceed 10% only when a polynomial was unable to produce a good fit (as in the case of 'flat' fringes, for example).

A third, independent reduction code, due to Sweeney[3], was used as a check of our results. This code expands the density distribution as a truncated Fourier-Bessel sampling series of finite bandwidth. The first term resembles a Gaussian; higher order terms contain higher frequency fluctuations. The number of terms used is subjectively determined. The series is Abel inverted, and the coefficients are fitted to the data in a least mean square sense. By keeping fewer (or more) terms in the sampling series, the effects of more (or less) smoothing are readily apparent. Sweeney reduced several of our interferograms using this code; the results agreed (to within 10%) with our own data reduction. The small discrepancies which did exist are most likely due to differences in the digitization of the data.

D. Interferometric Error Sources

There are several possible sources of error in analyzing the interferograms. The effects of refraction and poor imaging have already been mentioned. The holographic technique, which allows for post-shot focusing to within better than 10 μm, minimizes the effect of the latter. Numerical simulation shows that refractive effects cause approximately 10% error at densities of 10^{21} cm^{-3}; however, this error falls off to only a few percent for densities of less than 0.5×10^{21} cm^{-3}. The resolution of the digitizing table (0.01 inch) has been investigated, and found to contribute only negligibly to the errors. However, with some wide fringes, there is a degree of subjectivity in determining the center of the fringe. This usually occurs only for the outermost (low density) fringes, which tend to be broad. The resulting uncertainty in location in these cases is estimated to be 3 microns or less.

By far the two largest sources of error are the uncertainty in the exact form of the fringe function (the question of smoothing), and failure of the symmetry assumption. The methods used to estimate the effects of smoothing were discussed in the last section. The symmetry assumption, which is necessary to unfold the data, is that the plasma density depends only on the

cylindrical coordinates (r,z); i.e., it is rotationally symmetric about the laser beam axis. There is no means of verifying that this symmetry existed. A necessary, but not sufficient, condition is that the density profile obtained using the fringe data from above the symmetry axis should match that obtained using data from below the symmetry axis. Differences between the two sides are used as an estimate of the error due to lack of symmetry; these differences, along with the smoothing variations discussed previously, constitute the error bars shown on the density profile plots. There is one exception to this. For very large prepulses, the target support stalk strongly influences the plasma, but in the upper half-plane only. For these shots, only the lower half-plane is used to deduce the density, and there is no adequate check of the symmetry assumption.

V. RESULTS

A. Density Profiles And Backscattered Energy

The results of the density profile and backscattered energy measurements are summarized in Table III and in Figure 17. For each shot listed, an exponential scale length L has been deduced. The scale length is defined by the best fit of the equation

$$n = n_o \exp(-z/L) \tag{71}$$

to the axial density profile. (i.e., L is the inverse slope of the best straight line fit to the axial density data, when plotted on semi-log paper.) An example is shown in Figure 18. For most shots, equation (71) provided an adequate fit of the data. In a few cases, however, it was necessary to model the profile with two different scale lengths; (a small) one at high densities, and (a larger) one at lower densities. In Figure 17, for these cases, the longer scale length is used, since such regions are more favorable to Brillouin scattering[1].

Figures 19 and 20 show contrasting extremes. The interferogram in Figure 19 was taken 100 psec before the heating pulse, and shows the effects of a small prepulse which presumably arrived within a few hundred picoseconds of the main pulse. Figure 20 shows the effect of a large (1 Joule), deliberate prepulse, introduced 1.8 nsec

TABLE III

Scale Length and Backscattered Energy Summary

Shot Number	Energy Main (J)	Energy Prepulse (mJ)	Probe Time (ps)	Percent Backscatter	Density Scale Length (microns)
1913	4.5	700	55	24	44
1914	5.9	900	97	16	40
1915	5.5	900	97	13	27
1917	6.1	120	97	10.6	20
1918	5.4	350	97	15.5	33
1921	4.7	-	97	5.6	6
1922	4.0	-	97	12.8	30
1926	4.1	540	97	20.1	50
1941	4.0	280	97	17	35
1943	4.4	1	97	8.9	9
2012	2.9	-	55	10.6	16
2013	4.2	-	55	13.7	17
2020	3.2	-	27	9	12
2039	3.6	7	40	8.4	20
2041	3.2	6	40	9.9	9
2042	2.3	5	20	9.6	8
2045	2.4	5	0	15.1	10
2046	3.6	7	-30	13.9	16
2059	3.1	6	80	11.8	7
2069	4.0	100	62	10.3	21
2078	4.2	110	20	13.8	22
2131	1.0	25	80	17.9	40
2644	1.6	-	40	9.6	10
2697	5.8	20*	0	8.4	20

Laser Energy is for west beam.

Laser pulse width was nomimally 60 psec (FWHM).

Probe Time is positive if before peak of main beam.

Prepulse was 1.8 nsec in advance of main pulse.

* Had 1.0 nsec prepulse.

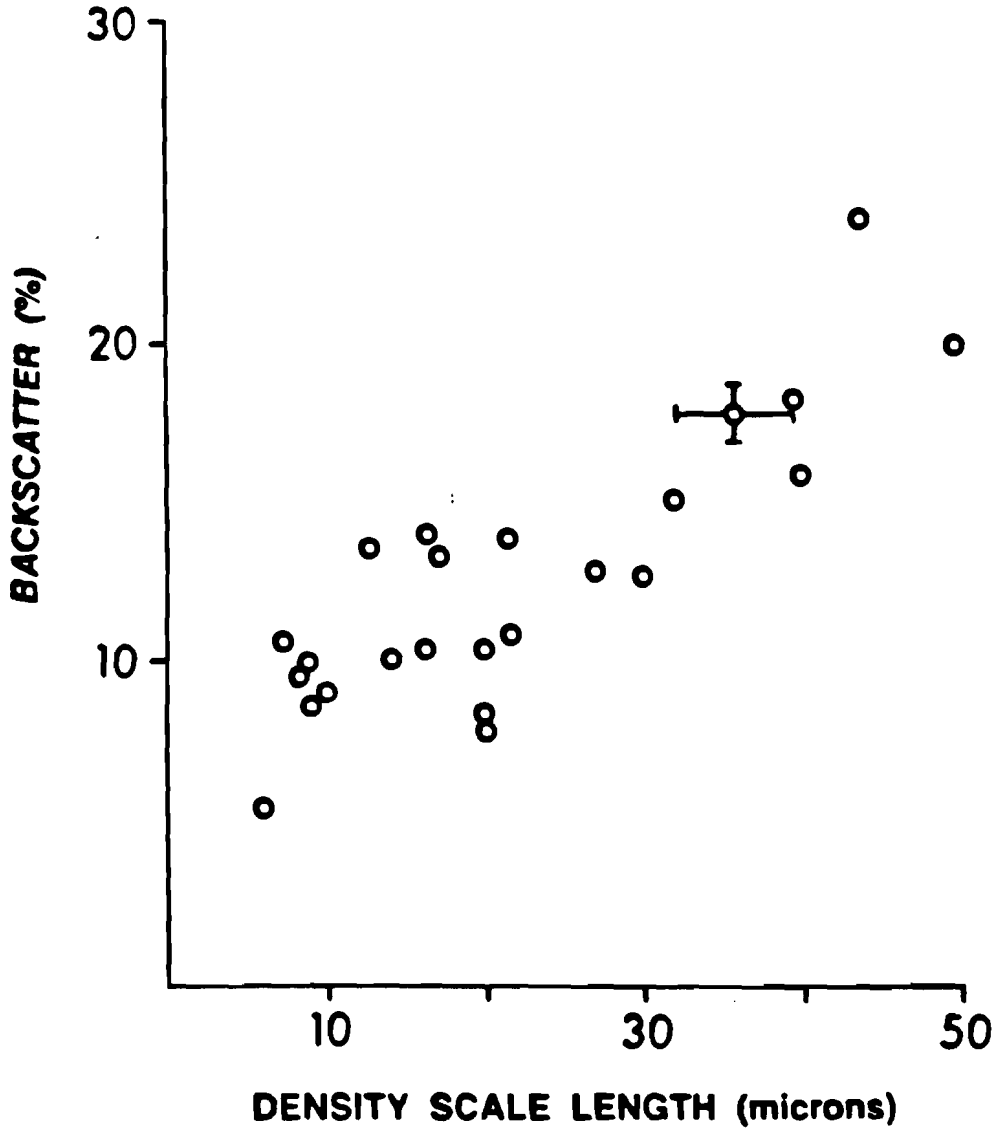

Figure 17. Plot of Fractional Backscatter and Density Scale Length Data

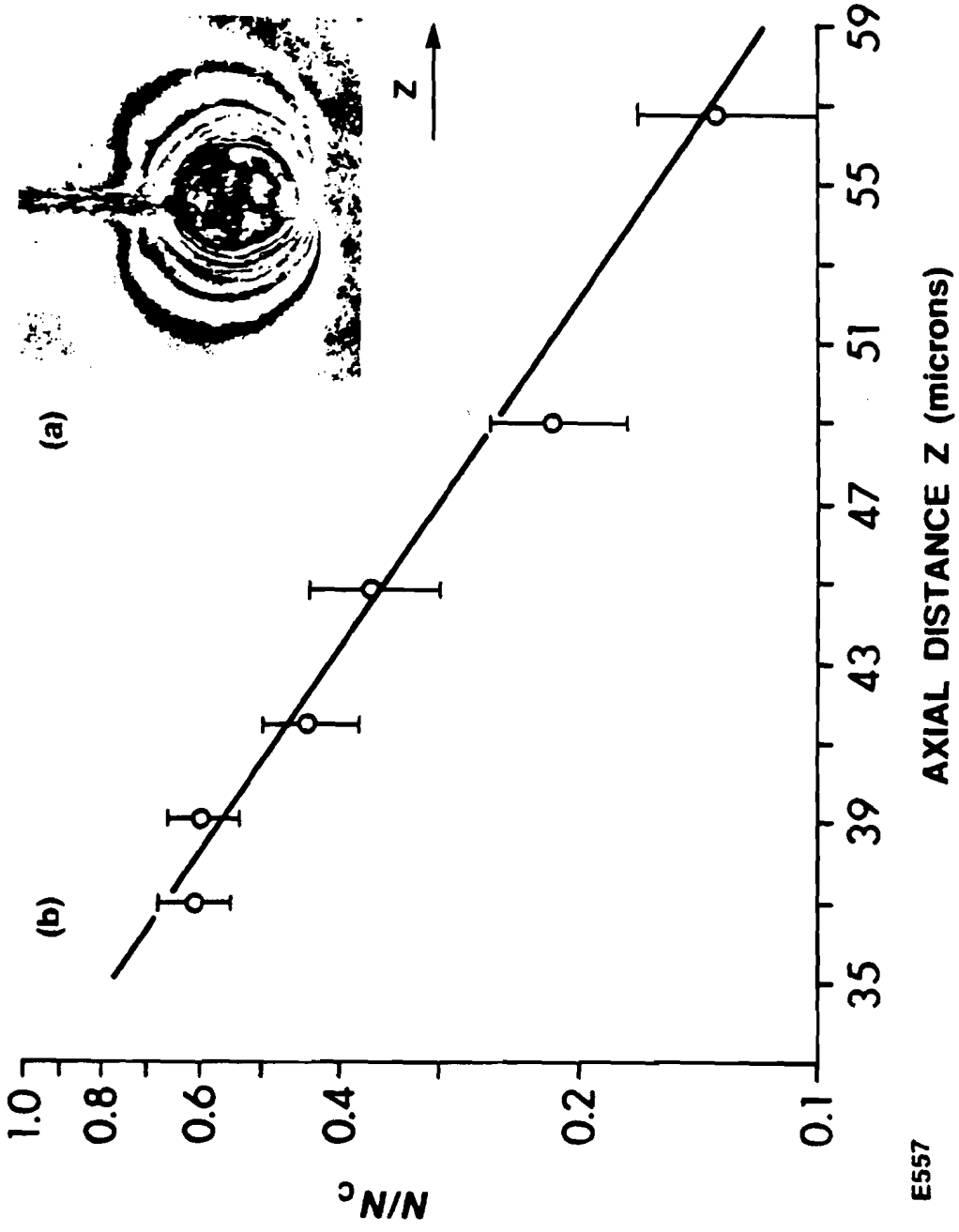

Figure 18. (a) Holographic Interferogram. (b) Axial Density Profile. Shot Number 2045.

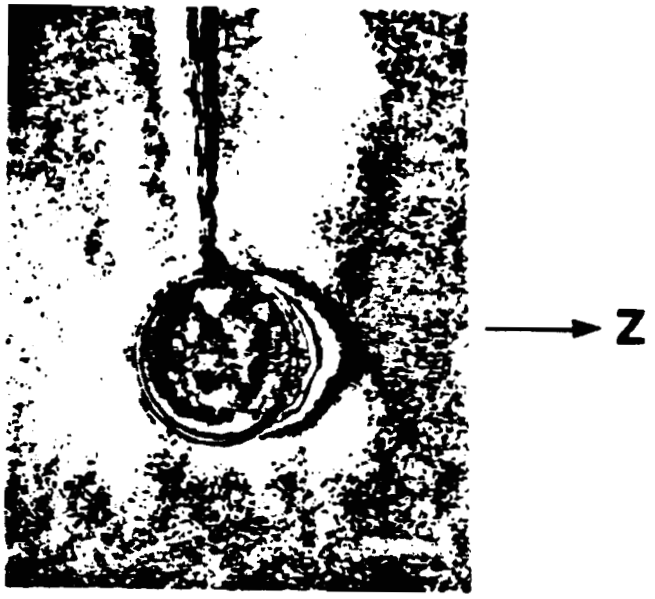

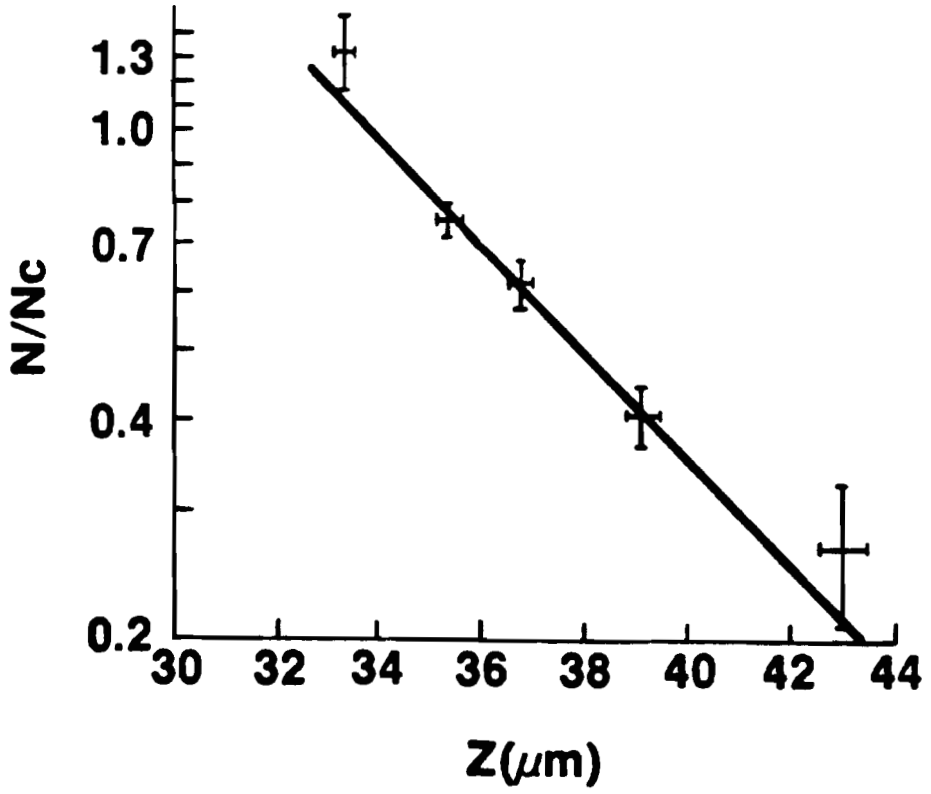

Figure 19. Interferogram and Axial Density Profile
Shot Number 1921

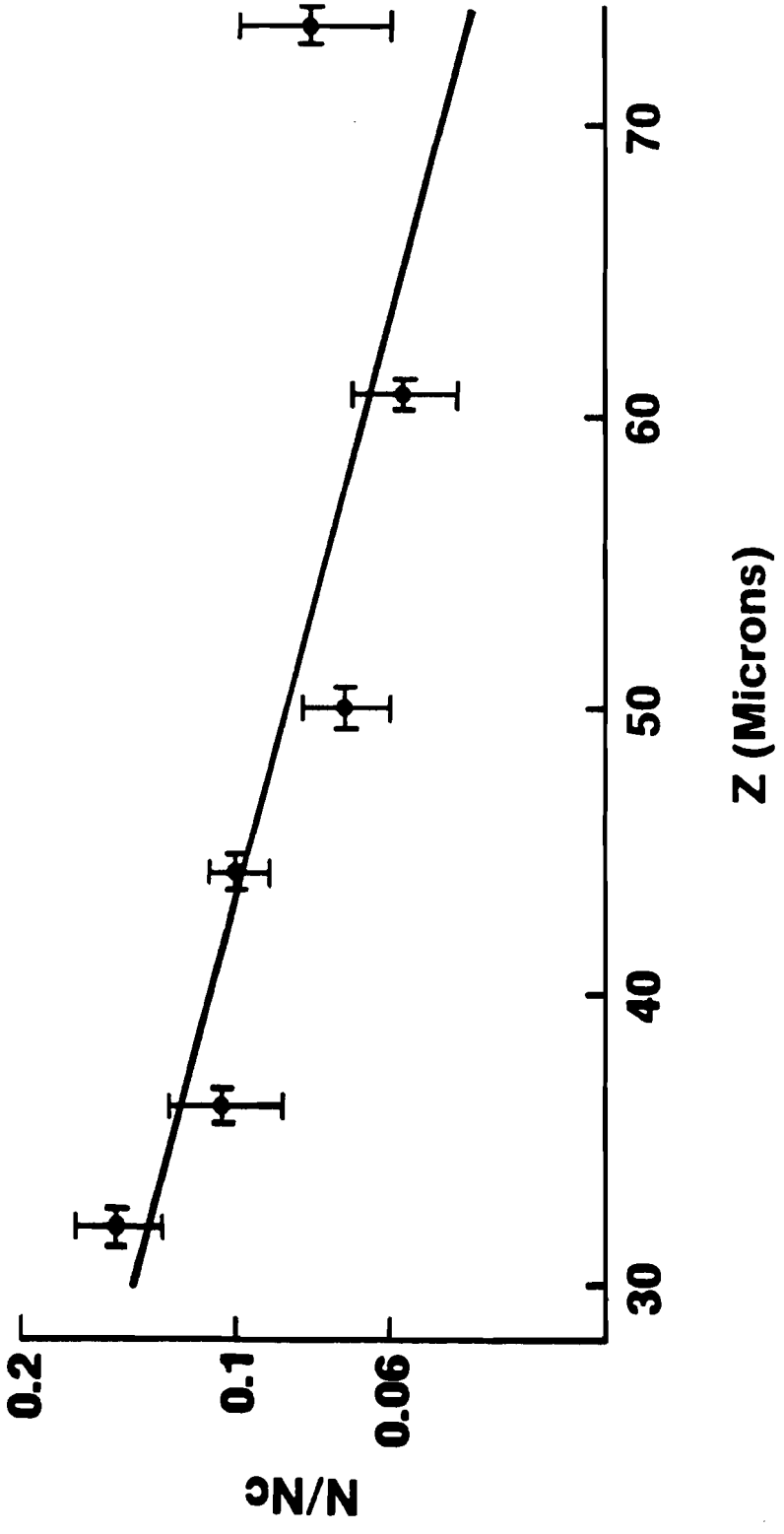

Figure 20. Axial Density Profile for Shot Number 1914

before the heating pulse. The plasma is clearly much larger, with a long axial scale length.

The data shown in Table III were all obtained with focusing at the center of the target. The intensity was not deliberately varied, and those variations that did occur did not seem to influence the results; i.e., no correlation was observed between the fractional backscatter and the incident energy. A qualitative correlation that is expected and observed is that the size of the plasma varies with the size and timing of the prepulse (the larger and earlier the prepulse, the larger the plasma which is observed). In contrast, the correlation between the prepulse energy and the measured scale length is poor. To be sure, very small (<1 mJ) prepulses tend to yield small (<10 μm) scale lengths, and very large (>500 mJ) prepulses give large (>30 μm) scale lengths. However, changing any given prepulse energy by, say, a factor of two, could well result in a larger or a smaller scale length, fluctuating from shot to shot. The reasons for this variation are not well understood. Of course, no two laser shots are ever exactly the same. Small, undetected changes in the pulse shape, including unintentional prepulses, may be responsible.

B. Time Integrated Backscatter Spectra

Time integrated backscatter spectra were recorded for most of the data shots. Figures 21-24 show the backscattered spectra, for a variety of prepulse conditions. The peak at 1.064 μm is the YAG reference line mentioned in chapter III. The traces in Figures 23 and 24 are typical of large backscatter shots. The spectra are asymmetric, with a slower decrease toward the longer wavelengths. Virtually all of the energy is red shifted, as expected for Brillouin scattering. The very weak prepulse case, Figure 21, also shows some energy shifted to longer wavelengths; some, however, also appears to be unshifted. It is somewhat surprising that there is little indication of a Doppler shift to shorter wavelengths, due to an outward expansion of the plasma. In fact, such a blue shift was observed, but only when there was a prepulse-suppressing dye cell in the laser beam. This is shown in Figure 25.

The true nature of the backscatter spectrum is seen only when it is time resolved; these results are reported in the next section.

C. Time Resolved Backscatter Spectra

The experimental procedure used for recording time resolved backscatter spectra is discussed in chapter III.

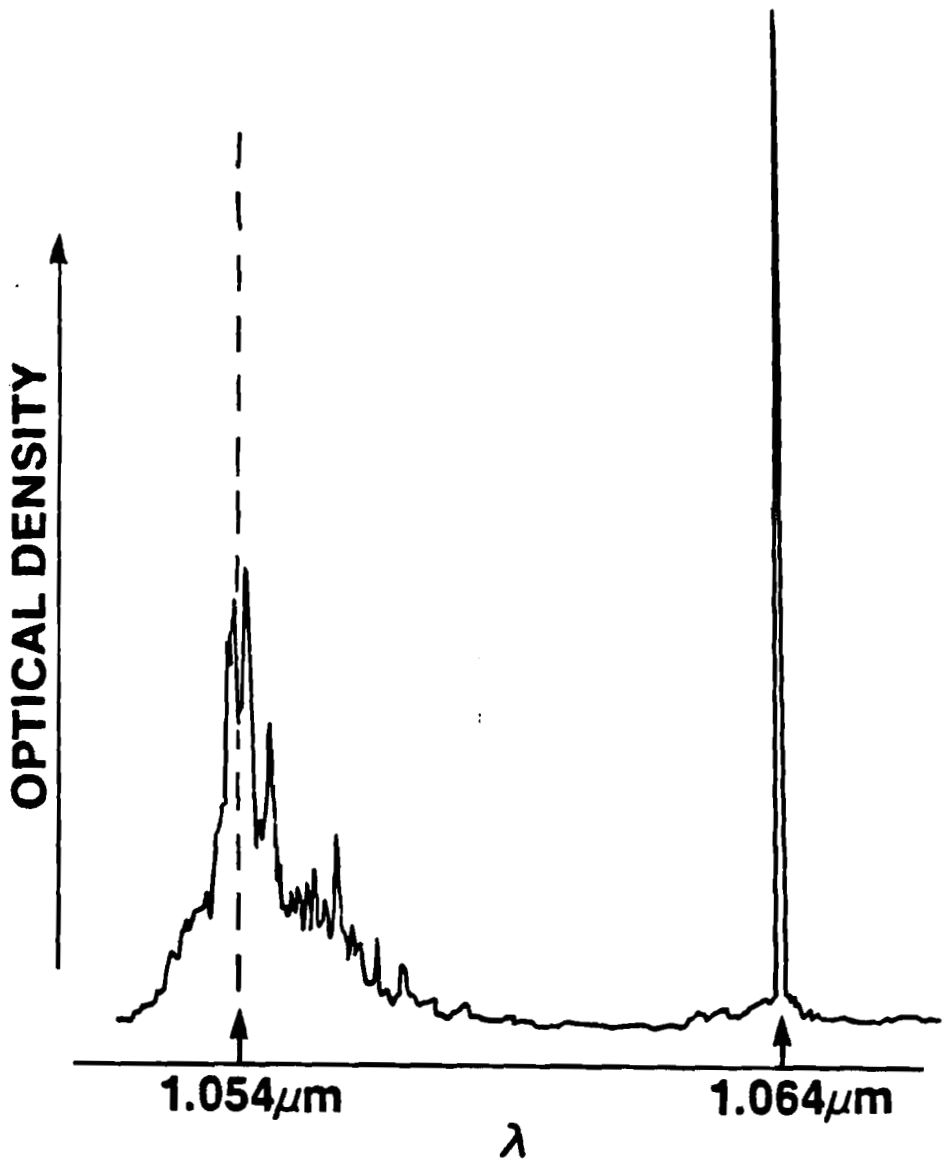

Figure 21. Time Integrated Backscatter Spectra
Shot Number 1921

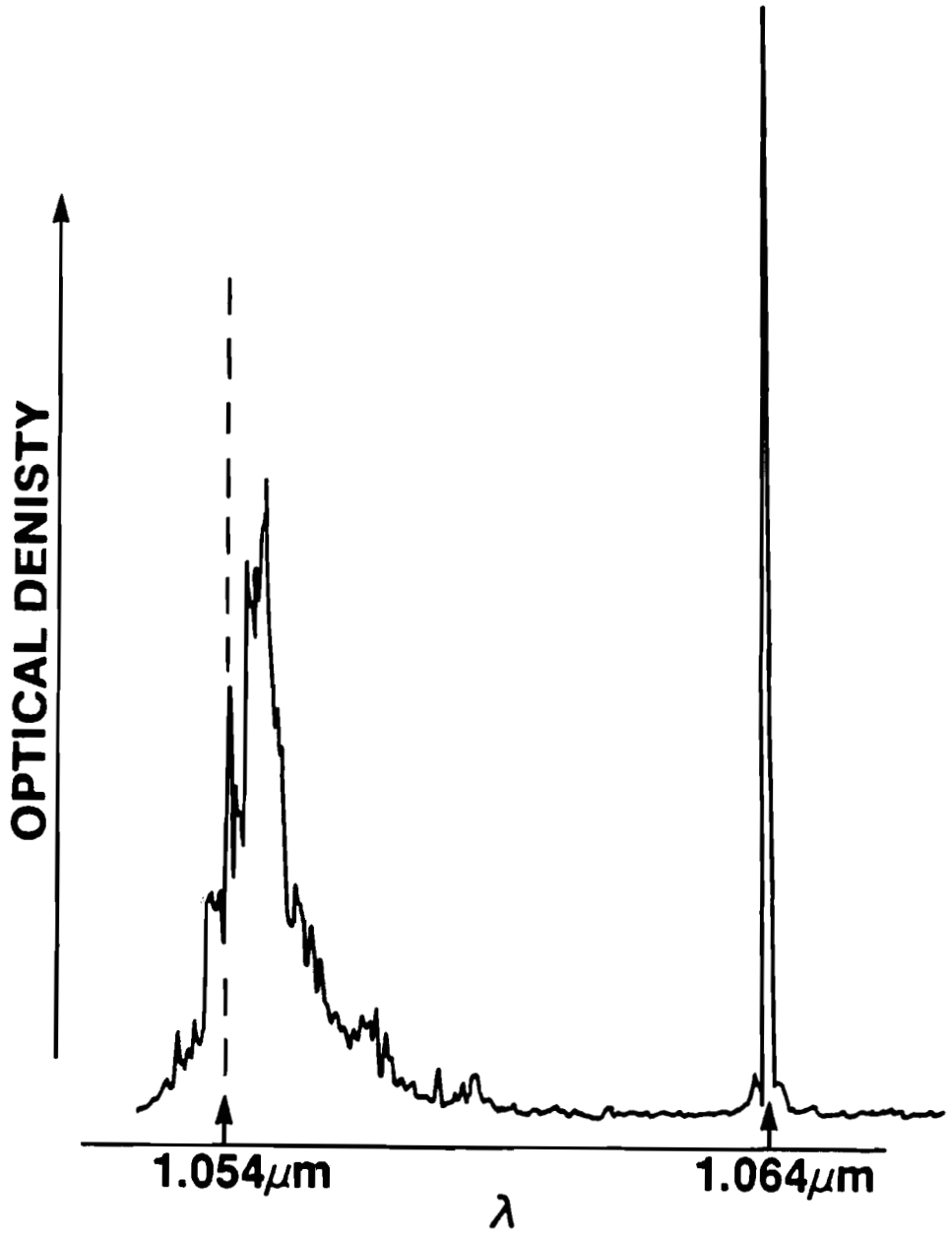

Figure 22. Time Integrated Backscatter Spectra
Shot Number 2045

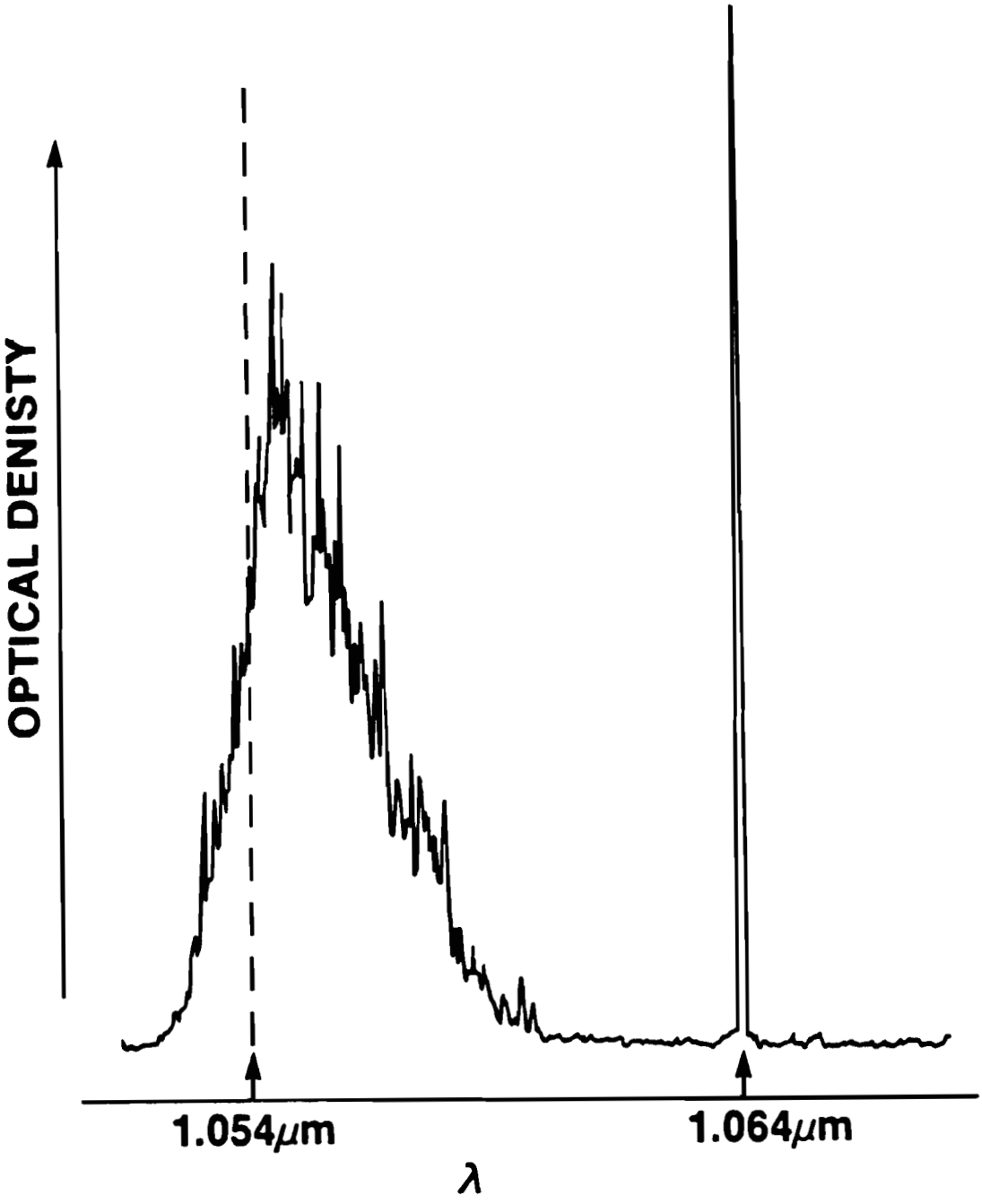

Figure 23. Time Integrated Backscatter Spectra
Shot Number 2078

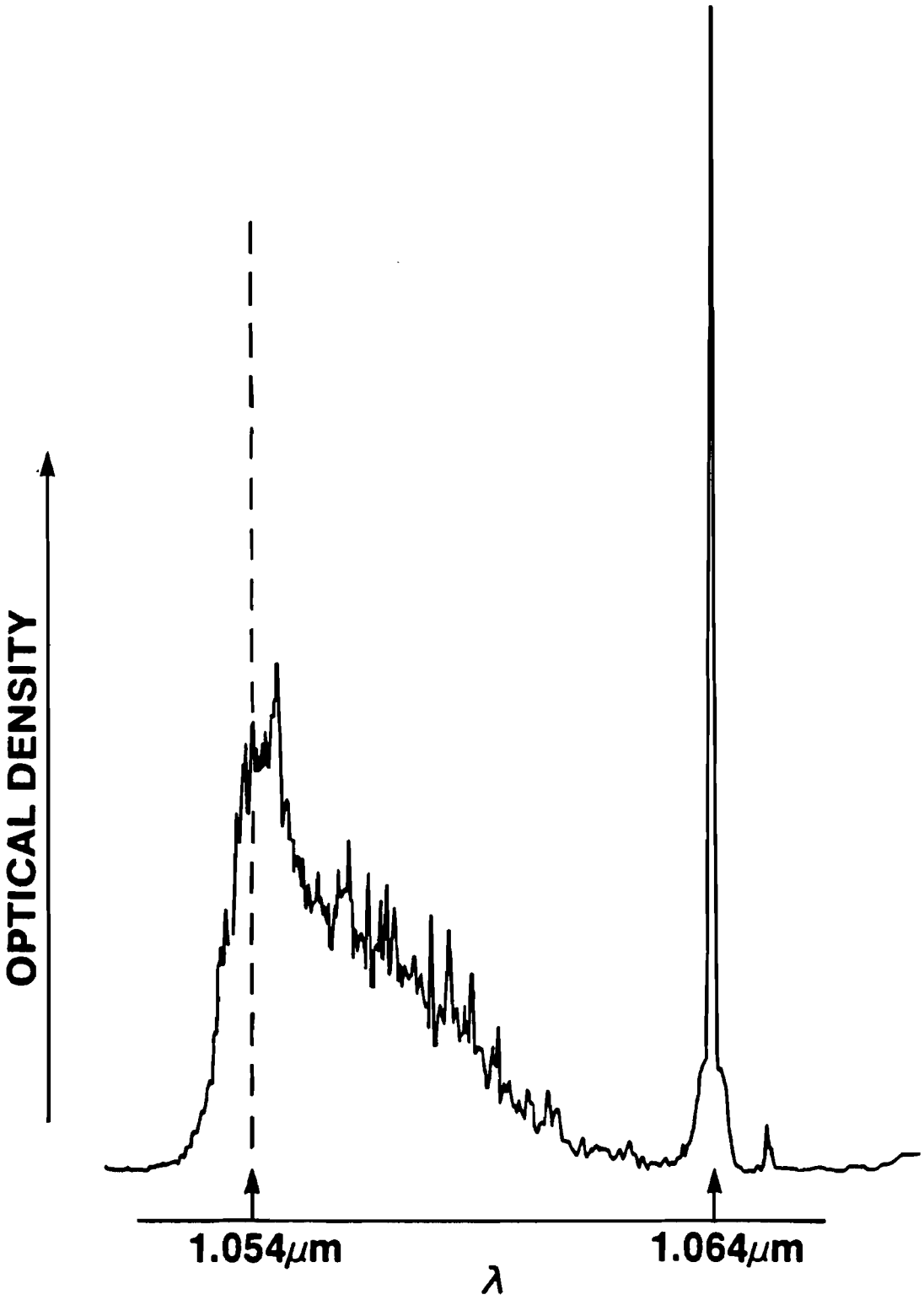

Figure 24. Time Integrated Backscatter Spectra
Shot Number 1914

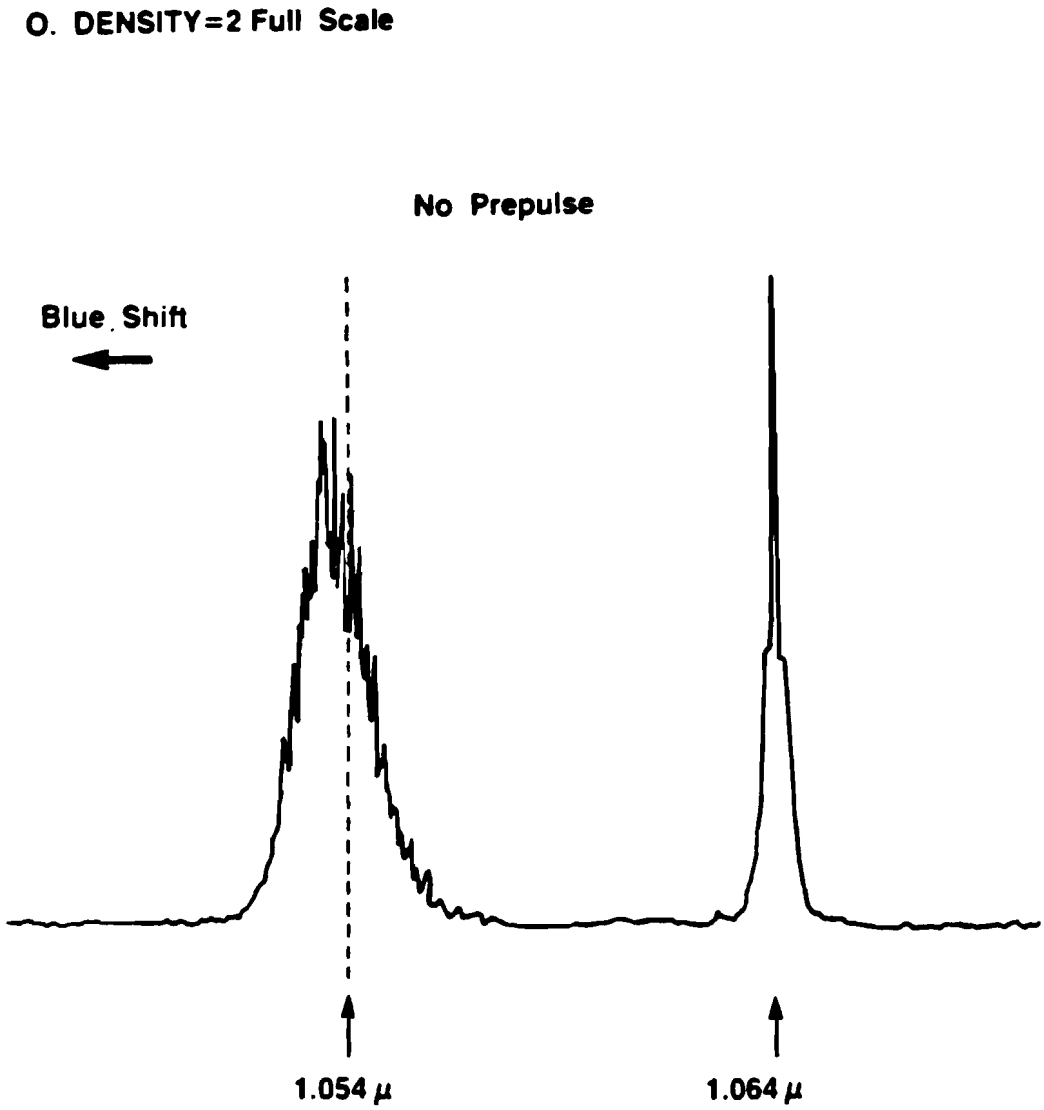

Figure 25. Backscatter Spectra With No Prepulse

Fourteen time resolved spectra (half on Polaroid, half on 35 mm film) were obtained. The focusing was again on the center of the targets. The size of the prepulse, which was introduced 1 nsec in advance of the main pulse, was varied between 0.1% and 1% of the total energy.

A typical streak photograph is shown in Figure 26. Microdensitometer traces for this shot, and two others, are shown in Figures 27, 28, and 29. The zero of the time scale was simply assigned to the earliest trace, in each case; the relationship between the times shown and the incident pulse was not measured. The densitometer slits were set to average over a 'window' of dimensions approximately equivalent to the system resolution: 13 psec by 3.1 Å.

The time resolved results show that the backscatter spectrum is not spectrally continuous, but rather, consists of a number of discrete modes. In Figure 27, the most intense peaks are red shifted from the incident wavelength by 12.2 (±2), 25.8 (±2), and 36.2 (±3) angstroms. While these modes appear to be harmonically related, it is not obvious that this is so in Figure 28 or 29. For these shots, there are modes present at a variety of wavelengths. A feature common to most of this data is the appearance of blue shifted light, at or near the peak of the backscatter intensity, but not earlier in time.

These results will be discussed further in chapter VI.

TIME RESOLVED BACKSCATTER SPECTRA

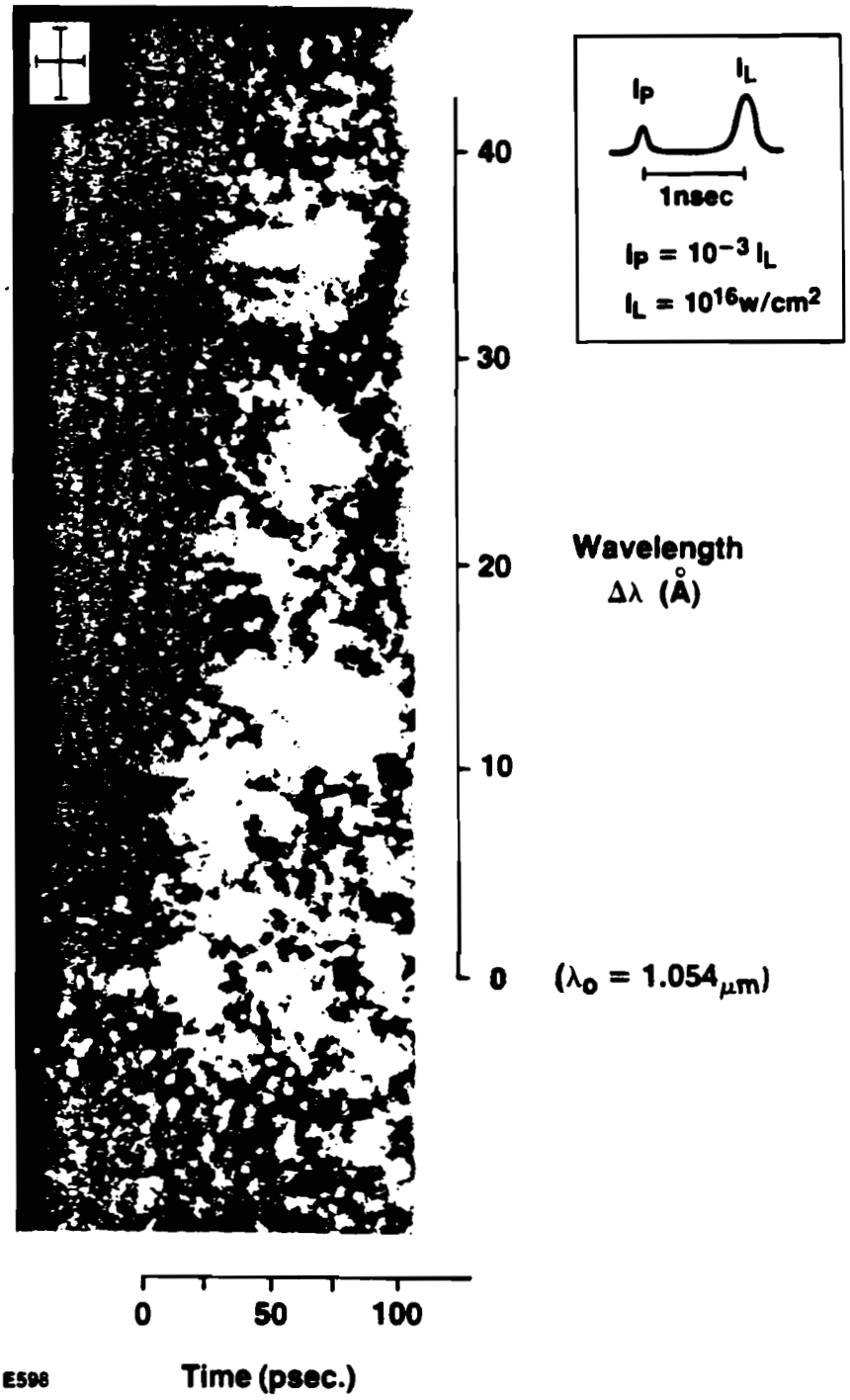

Figure 26

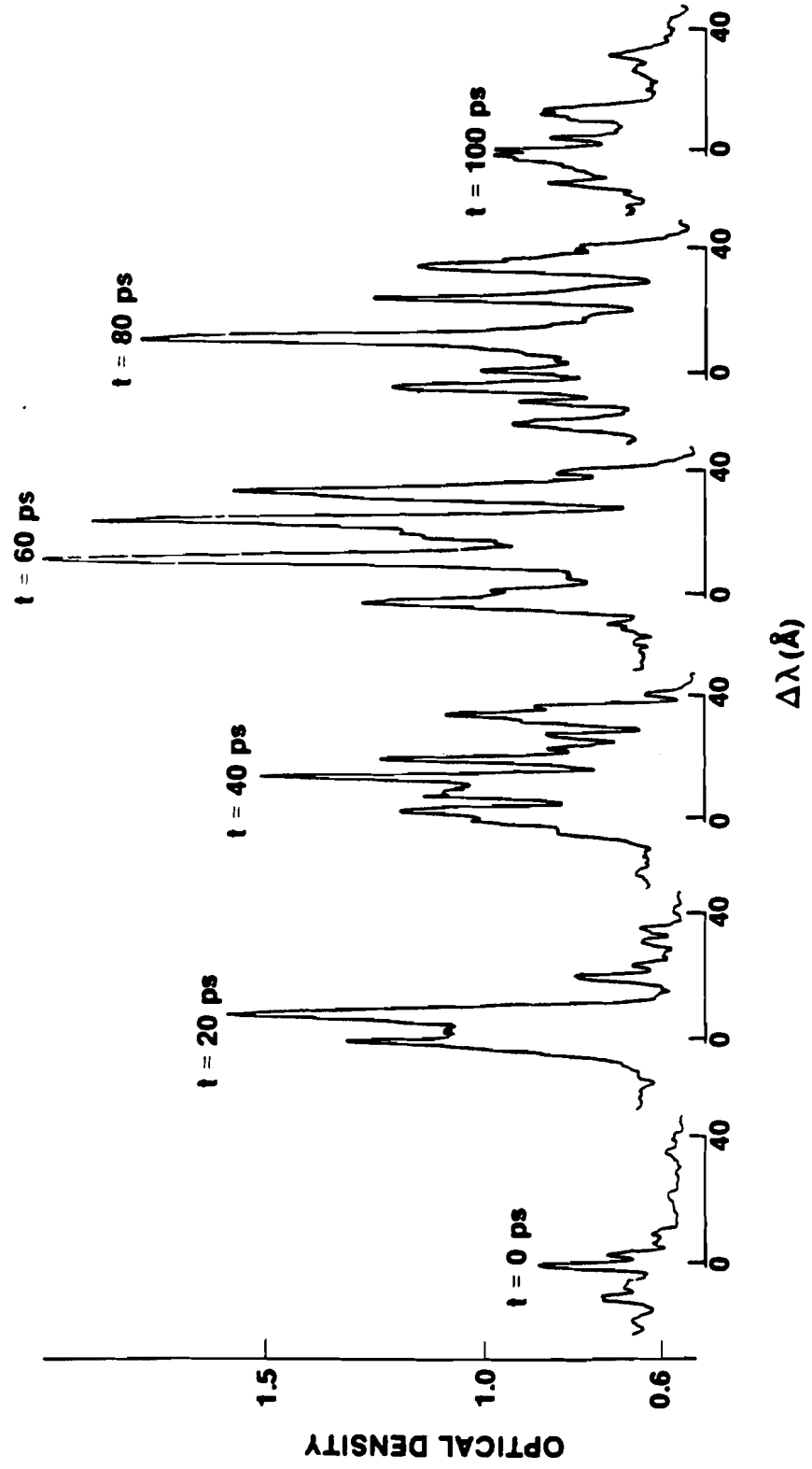

Figure 27. Densitometer Traces of Time Resolved Backscatter Spectra
Shot Number 3222 (0.1% prepulse 1 nsec before main pulse)

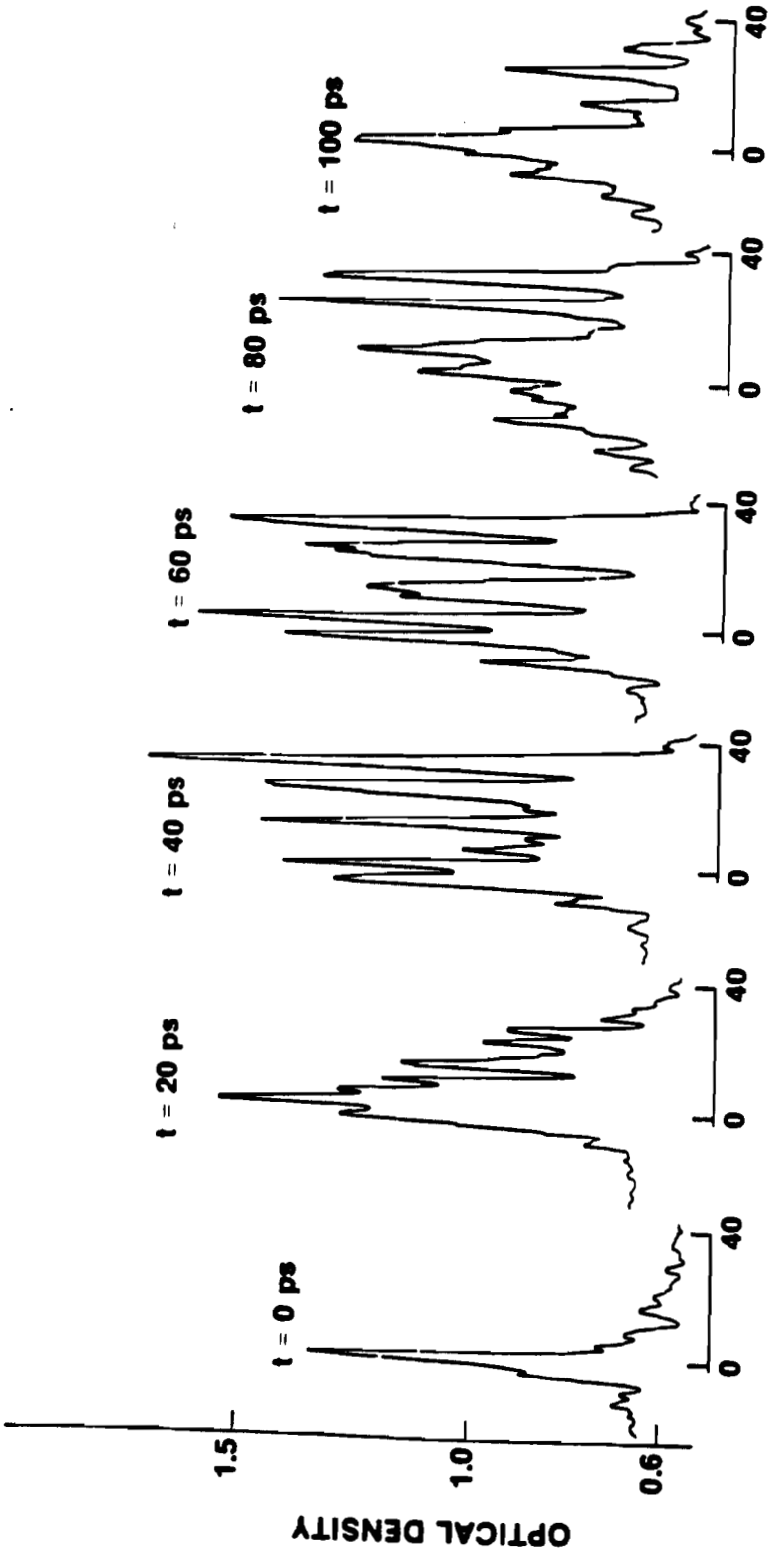

Figure 28. Densitometer Traces of Time Resolved Backscatter Spectra
Shot Number 3224 (0.1% prepulse 1 nsec before main pulse)

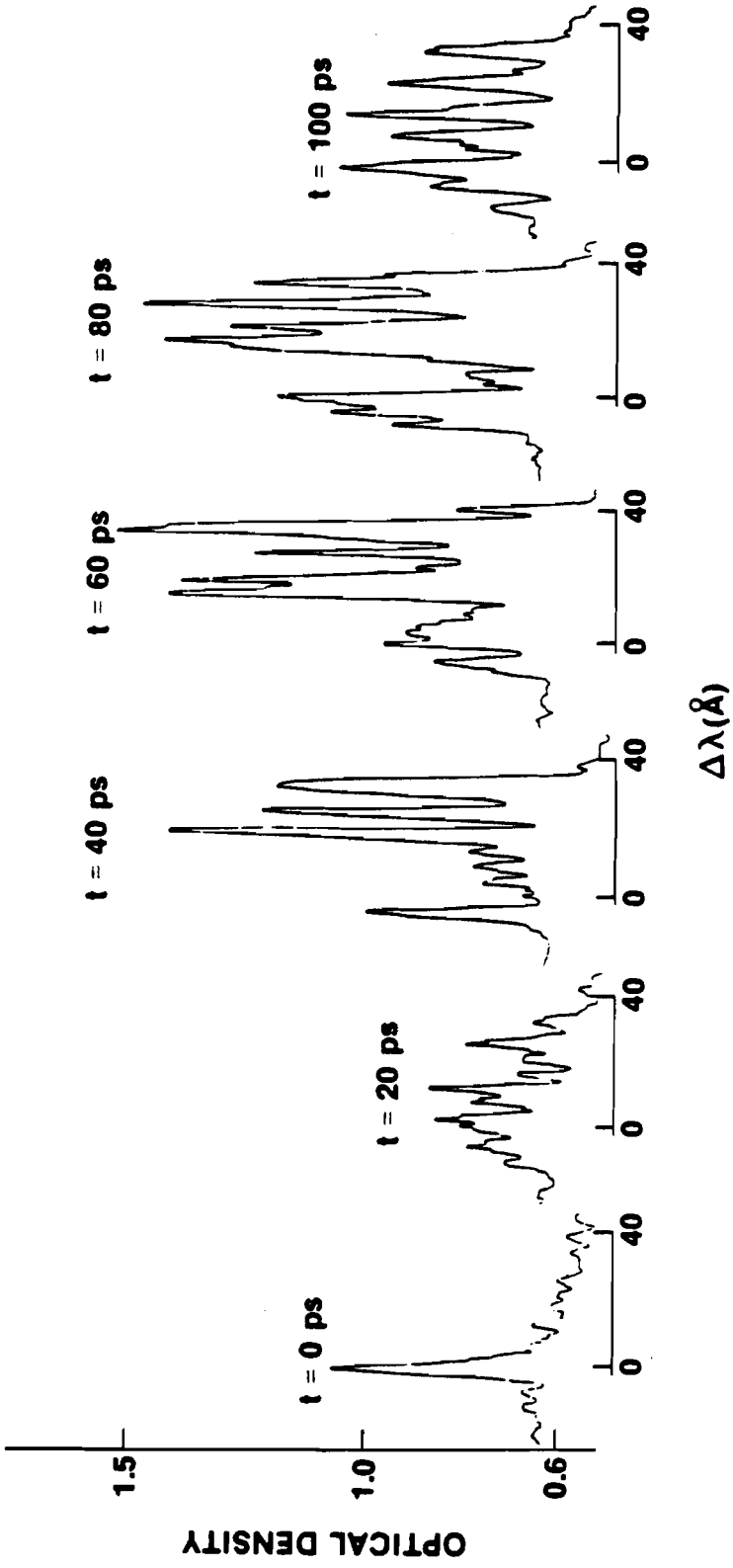

Figure 29. Densitometer Traces of Time Resolved Backscatter Spectra
Shot Number 3221 (1% prepulse 1 nsec before main pulse)

VI. DISCUSSION

A. Density Scale Length Dependence

In chapter II, we discussed several possible nonlinear mechanisms for limiting Brillouin backscatter, and made some simple estimates of the fractional backscatter predicted by them. We will now compare the density scale length and fractional backscatter data with the predictions of these models. It should be kept in mind that any quantitative agreement is somewhat fortuitous, for several reasons. First of all, the models are all strictly one dimensional, and planar, while the experiment is on spherical targets, and measures backscatter within a small but finite (0.19 str) solid angle. Secondly, several parameters (the electron and ion temperatures, and the density at which the scattering is occurring) are not precisely known, and must be estimated. Finally, the wave vector mismatch caused by the density gradient makes it unlikely that the scattering region is an entire exponential scale length long. We will compare the measured scale length with these models, which use a finite length homogenous plasma, in order to ascertain whether or not they scale properly.

We assume that the scattering is occurring in the density region $0.1<(n/n_c)<0.5$. At higher densities, the wavenumber of the electromagnetic waves becomes small, going to zero at the critical density. The linear growth rate of the instability also vanishes there. Physically, the increase in the size of the wavelength as one approaches the critical surface causes the gradient of the field amplitude to decrease. This reduces the size of the pondermotive force driving the ion-acoustic wave.

Brillouin scattering can occur at densities of less than $0.1\ n_c$; however, we believe that higher densities are strongly favored. The linear growth rate (equation (26)) is larger for higher densities. For waves which are non-linearly limited to some fixed fraction $\delta n/N$, equations (47) and (44) show considerably higher reflected energy for higher densities. The non-linear model of Kruer[1,2], equations (55)and (56), also show a strong increase in reflectivity with increasing density. In Kruer's model, there is a simple physical explanation. The reflectivity is limited by Landau damping due to the hot ions. The temperature of the ions will, if other parameters are held constant, be inversely proportional to the density (see equation (57)). The lower the ion density, the smaller the heat capacity is. Thus, at low densities, the ion temperature is high, and Landau damping is strong, preventing significant

backscatter from occurring. For our estimates, we will use $n = 0.2n_c$.

Figure 30 shows a plot of the backscattered energy and density scale length data. Superimposed is the reflectivity estimate obtained in chapter II for an ion-acoustic wave which is non-linearly limited by harmonic generation to $\delta n/N = 0.06$. It is clear that the predicted reflectivity is too large for the longer scale lengths. As mentioned in chapter II, this is because the finite amount of ion heating, which is important in limiting the reflectivity, has been neglected.

Figure 31 shows a plot of the data, and the prediction of the ion heating model[1], again using the same parameters as were used in chapter II ($n = 0.2n_c$, $T_e = 6$ KeV, $I_o = 3\times10^{15}$ W/cm^2). This model fits the data well; in particular, the backscattered energy increases with increasing scale length at approximately the same rate as the model predicts. We conclude, therefore, that ion heating is an important effect in limiting Brillouin backscatter, even for our relatively short pulse experiments.

It should be noted that the model predictions[2] are essentially unchanged for higher intensities, or lower electron temperatures. This is because, for $(v_o/v_e)^2 > 0.2$, the Landau damping (ν) increases with increasing $(v_o/v_e)^2$,

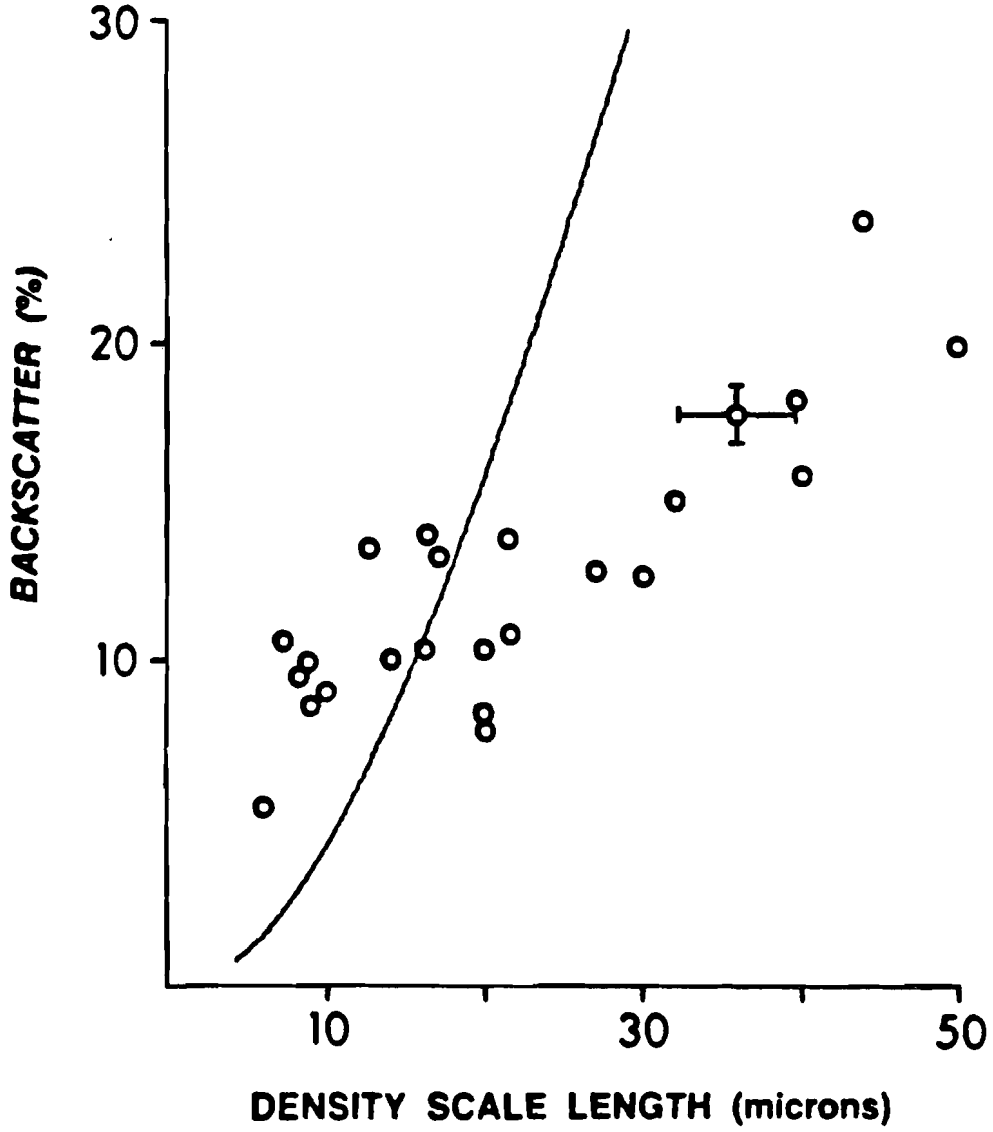

Figure 30. Comparison of Scale Length Data With A Simple Non-Linear Theory ($\delta n/N = 0.06$)

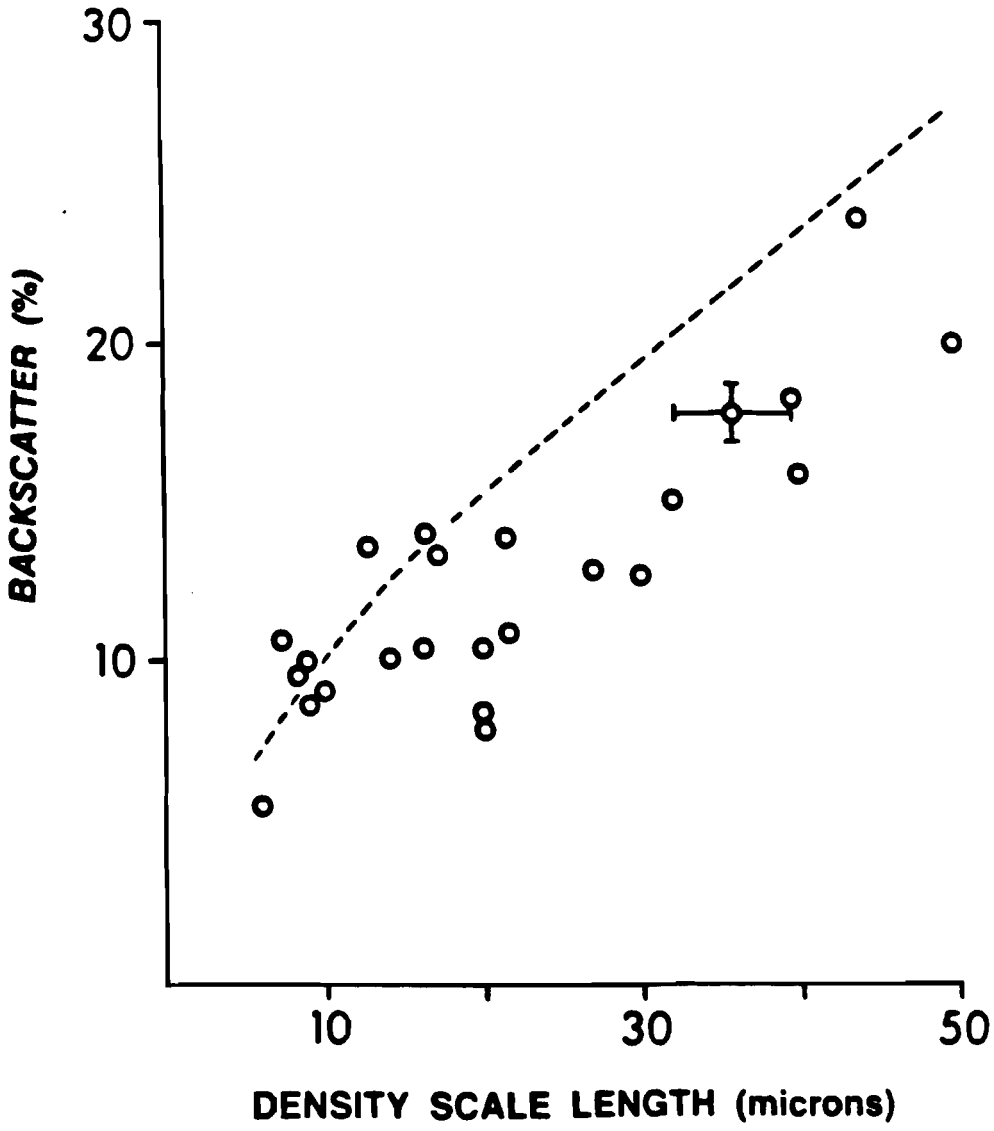

Figure 31. Comparison of Scale Length Data With The Ion-Heating Theory of Kruer

so that the factor q in equation (56) remains approximately unchanged. This, of course, is the negative feedback effect of the ion heating that has been previously discussed. The data supports this aspect of the model. All of the shots taken had $(v_o/v_e)^2 > 0.2$, and no correlation exists between backscatter and incident intensity. However, it must be pointed out that the experiment was not designed to test this aspect of the model; the intensity variations range over less than one order of magnitude, as an inspection of Table III shows.

Figure 32 shows the scale length data, and the ion heating model's predictions[2] for different assumed plasma densities. The intensity was taken to be 3×10^{15} W/cm^2, and the electron temperature used was 3 KeV (or $(v_o/v_e)^2 = 0.4$). As mentioned previously, there is virtually no change in the predictions for higher intensities and/or lower electron temperatures. The upper curve in Figure 32 is for an electron density of $0.33n_c$, while the lower one is for a density of $0.15n_c$. One sees that a higher scattering density allows for substantially more backscatter. In the context of the model, this is because the larger heat capacity causes a lower ion temperature, and therefore less Landau damping. It should be mentioned that these curves have been calculated using a slightly more sophisticated version of the model[2]. In this improved model, the ion Landau damping creates a hot 'tail' in the

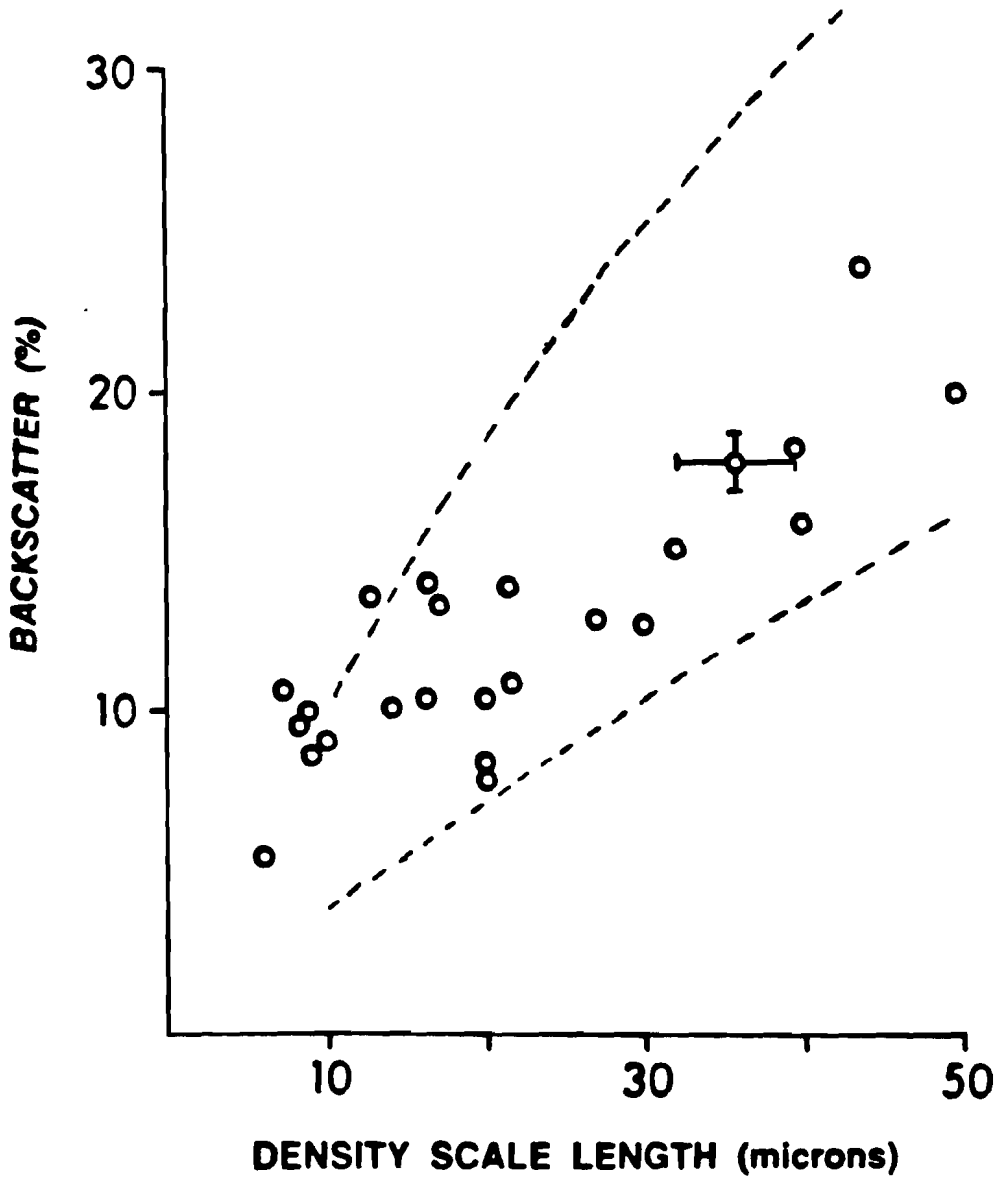

Figure 32. Ion Heating Model Predictions For (N/N_c) Equal To 0.33 (Upper Curve) and 0.15 (Lower Curve)

ion distribution function, around $v = c_s$. However, the results are found to be essentially the same as those predicted by the bulk heating version of the model.

One should be cautioned against attempting to attach quantitative significance to the curves shown in Figure 32. As mentioned in the beginning of this section, the problem of calculating Brillouin scattering at high intensities for an inhomogeneous plasma is extremely difficult, and the one dimensional homogeneous model used must be regarded as a great simplification.

The question of the size of the total stimulated scattering into all solid angles has not been addressed here. Others have presented evidence for stimulated side scattering in high power laser pellet irradiation experiments[3]. In addition, it is known[4] that a considerable amount of light energy is scattered into the region just outside the solid angle subtended by the focusing lens. A spectral investigation is currently under way[5] to determine if this light originates from a stimulated process. Thus, while it appears that the directly backscattered light is limited to a reasonably small value, the total amount of stimulated scattering may be unacceptably large in a shaped pulse experiment. This is especially true if large targets and focal spots are used, since this would increase the effective length for stimulated side scattering.

B. Spectral Results

The backscatter spectra show, as anticipated, a red shift, characteristic of Brillouin scattering. They also show, for large backscatter cases, some energy shifted as much as 80 Å from the initial wavelength. It is difficult to reconcile this fact with a simple model of Brillouin scattering, where $\Delta\lambda = 2c_s\lambda_o/c$, so that an 80 Å shift would imply ion-acoustic velocities of over 10^8 cm/sec, or electron temperatures of over 24 KeV. The time resolved backscatter spectra show quite clearly that the scattering taking place at these high intensities is definitly not a simple, one Brillouin mode event. Rather, at any one instant in time, there are a number of well defined wavelengths at which the scattering is occurring. There are several possible explanations.

In the development of the equations in chapter II, only the resonant terms were kept in the driving (pondermotive) force. However, when the waves have grown large, the non-resonant terms may become important. Thus, the component of the product of the pump wave and the acoustic wave which has a frequency of $\omega_o+\omega_2$ can drive an anti-Stokes, or blue shifted, backscattered wave. Similarly, the product of the backscattered wave and the ion-acoustic wave can drive another backscattered wave at frequency $\omega_1-\omega_2$, or $\omega_o-2\omega_2$. Since these

waves are not resonantly driven, they depend on the initial, resonant interaction to keep the ion-acoustic wave driven to a large value.

Another possible explanation, which was mentioned in chapter II in connection with limiting the amount of Brillouin backscatter, is the generation of harmonics by the ion-acoustic wave[6]. When the acoustic wave is rapidly driven to large values, it becomes non-sinusoidal; a Fourier analysis shows the presence of higher harmonics. These could beat directly with the electomagnetic pump wave to produce backscatter at different (harmonically related) wavelengths.

Still another possibility is multiple Brillouin scatterings[7]. That is, the backscattered wave could itself undergo stimulated scattering, with the scattered wave now heading back into the plasma. This wave could now scatter, and the process would repeat again. At each Brillouin scattering, the wave becomes further red shifted, thus giving rise to a cascade of modes.

None of these explanations is entirely satisfactory. The theories involving higher order mode interactions and ion-acoustic wave harmonic generation would predict that the modes should all be harmonically related. The multiple scattering model does not require this, if one is willing to assume that the different scatterings

occur at different places within the plasma (a difficult to justify assumption), so that each additional wavelength shift would be governed by different parameters. If the multiple scatterings are taking place in the same region, then the backscatter should be red shifted by $1\omega_2$, $3\omega_2$, $5\omega_2$, etc. The even harmonics are, of course, forward scattered; if they are reflected from the critical surface, however, they might be mistaken for backscatter. The backscatter data does not show only odd harmonics, and so does not appear to support the multiple scattering model. As for the other models mentioned, the data shows some modes to be harmonically related, while others do not appear to be. An additional serious problem for all of these theories is the observation that, at certain particular times, (for example, t=60 psec in Figure 29), a mode with a large red shift is more intense than those with smaller red shifts. It is difficult to conceive of a situation where a non-resonant mode should be larger than a resonant one, or where a high harmonic should be larger than the fundamental. For the multiple scattering model to account for this data, it is necessary to make the assumption that the first several scatterings occur with very high efficiency, each reflecting over 60% of the light, and to further assume that the even harmonics are efficiently reflected from the critical surface.

Kruer has suggested[2] that the complex spectral results may be due, in part, to the formation of hot ion tails (i.e., an ion velocity distribution which is modeled by two Maxwellians, one of which (the 'tail') is at a high temperature), which have been formed by either ion trapping or Landau damping of the acoustic wave. If the temperature of the ions in this tail is comparable to Z times the electron temperature, then the ion-acoustic velocity can be increased, since

$$c_s^2 = (ZT_e + 3T_i)/M_i \quad . \tag{14}$$

The suggested[2] scenario is that an ion-acoustic wave forms; it is damped, forming an ion tail with temperature T_1 ($T_1 \approx M_i c_s^2$); this now supports a new acoustic mode, at a higher phase velocity; it is damped, forming a new tail at temperature T_2, where $T_2 > T_1$; the process continues. Thus this 'tail on a tail on a tail...' ion distribution gives rise to a complex spectral mode pattern. The details of this model have not yet been worked out. The calculation is difficult, since it depends on the exact shape of the ion distribution function, which is only crudely known.

These data suggest other experiments which may provide additional useful information regarding the nature of Brillouin scattering. In particular, time resolved backscatter spectral measurements performed at

lower intensities may show the mode development more clearly. This is suggested by the time integrated spectra, which show less energy at large red shifts (fewer modes) when the backscatter (and, presumably, the non-linear effects) are smaller.

In conclusion, we have presented clear experimental evidence of multiple modes in Brillouin scattering. While several simplified theoretical explanations exist, none are completely satisfactory for explaining the data in detail. We expect that these observations of multiple modes will eventually lead to an increased understanding of the complex nature of Brillouin scattering from high power laser produced plasmas.

ACKNOWLEDGEMENT

This work was partially supported by the following sponsors: Exxon Research and Engineering Company, General Electric Company, Northeast Utilities Service Company, New York State Energy Research and Development Authority, The Standard Oil Company (Ohio), The University of Rochester, and Empire State Electric Energy Research Corporation. Such support does not imply endorsement of the content by any of the above parties.

REFERENCES

1- 1 M.J. Lubin and A.P. Fraas, Scientific American 224, 21 (1971); F.F. Chen, "Introduction To Plasma Physics", (Plenum Press, New York, 1974), pg. 310.

1- 2 J. Dawson and C. Oberman, Physics of Fluids 5, 517 (1962).

1- 3 K.G. Estabrook, E.J. Valeo, and W.L. Kruer, Physics of Fluids 18, 1151 (1975); T. Speziale and P.J. Catto, Physics of Fluids 20, 990 (1977).

1- 4 N.A. Krall and A.W. Trivelpiece, "Princeples of Plasma Physics", (McGraw-Hill, New York, 1973), pg. 386ff.

1- 5 J. Albritton and P. Koch, Physics of Fluids 18, 1136 (1975).

1- 6 F.F. Chen, "Introduction To Plasma Physics", (Plenum Press, New York, 1974), pg. 259-270.

1- 7 C.S. Liu, M.N. Rosenbluth, R.B. White, Physics of Fluids 17, 1211 (1974).

1- 8 D.W. Forslund, J.M. Kindel, E.L. Lindman, Physics of Fluids 18, 1002, 1017 (1975).

1- 9 K. Nishikawa, in "Advances In Plasma Physics", Vol 6, A. Simon, W. Thompson, editors, (John Wiley and Sons, New York, 1976), pg. 3-82.

1-10 D.W. Phillion, W.L. Kruer, V.C. Rupert, Physical Review Letters 39, 1529 (1977).

1-11 J.M. Dawson, W.L. Kruer, B. Rosen, in "Dynamics of Ionized Gases", M. Lighthill, I. Imai, H. Sato, editors, (University of Tokyo Press, Tokyo, 1973) pg. 47 ff.

1-12 B.H. Ripin, et al., Physical Review Letters 39, 611 (1977).

2- 1 C.S. Liu, M.N. Rosenbluth, R.B. White, Physics of Fluids 17, 1211 (1974).

2- 2 K. Nishikawa, Journal of the Physical Society of Japan 24, 916 (1968).

2- 3 A.A. Galeev, et al., Soviet Physics JETP Letters 17, 35 (1973).

2- 4 D.W. Forslund, J.M. Kindel, E.L. Lindman, Physics of Fluids 18, 1002, 1017 (1975).

2- 5 J. Drake, et al., Physics of Fluids 17, 778 (1974).

2- 6 M.N. Rosenbluth, Physical Review Letters 29, 565 (1972).

2- 7 J.M. Dawson, W.L. Kruer, B. Rosen, in "Dynamics of Ionized Gases", M. Lighthill, et al., editors, (University of Tokyo Press, Tokyo, 1973) pg. 47 ff.

2- 8 S.J. Karttunen, R.R.E. Salomaa, Plasma Physics 21, 247 (1979).

2- 9 D.W. Forslund, J.M. Kindel, E.L. Lindman, Physical Review Letters 30, 739 (1973).

2-10 W.L. Kruer, in "Advances In Plasma Physics", Vol 6, A. Simon, W. Thompson, editors, (Wiley, New York, 1976), pg. 237 ff.

2-11 P. Bertrand, M.R. Feix, Physics Letters A 28, 68 (1968).

2-12 D.W. Phillion, W.L. Kruer, V.C. Rupert, Physical Review Letters 39, 1529 (1977).

2-13 W.L. Kruer, Bulletin of the American Physical Society 24, 1031 (1979).

2-14 N.A. Krall and A.W. Trivelpiece, "Principles of Plasma Physics", (McGraw-Hill, New York, 1973), pg. 389 ff.

2-15 W.L. Kruer, K.G. Estabrook, Lawrence Livermore Laboratory Report UCRL-83743, and "Proceedings of the Fifth Workshop on Laser Interaction and Related Plasma Phenomena"(to be published), (Rochester, N.Y. 1979).

2-16 C.L. Tang, Journal of Applied Physics 37, 2945 (1966).

2-17 T. Dewandre, J.R. Albritton, E.A. Williams, Bulletin of the American Physical Society 24, 981 (1979).

2-18 S. Jackel, B. Perry, M. Lubin, Physical Review Letters 37, 95 (1976); S.M. Jackel, Ph.D. thesis, University of Rochester (1977), pg. 129.

3- 1 W. Seka, et al., Applied Optics 19, 409 (1980).

3- 2 N.H. Burnett, et al., Applied Physics Letters 31, 172 (1977).

3- 3 B.H. Ripin, et al., Physical Review Letters 39, 611 (1977).

3- 4 A. Yariv, "Quantum Electronics" (Second Edition), (Wiley, New York, 1975), pg. 407-434.

3- 5 J. Machewirth, R. Webb, D. Anafi, Laser Focus 12, No. 5, 104 (1976).

3- 6 J. Wilson, C. Lin, J. Hoose, Laboratory For Laser Energetics Report No. 44, (1975).

3- 7 Corning Glass, Corning, New York.

3- 8 J.M. Stone, "Radiation and Optics", (McGraw-Hill, New York, 1963), pg. 239.

3- 9 H.M. Smith, "Principles of Holography", (Wiley, New York, 1975), pg. 204.

3-10 R. Fedosejevs, et al., Physical Review Letters 39, 932 (1977).

3-11 H.M. Smith, op. cit., pg. 227 ff.

3-12 D.T. Attwood, L.W. Coleman, D.W. Sweeney, Applied Physics Letters 26, 616 (1975); D.T. Attwood, et al., Physical Review Letters 40, 184 (1978).

3-13 Tropel, Inc., Fairport, New York.

3-14 R. Hopkins, (private communication).

3-15 Eastman Kodak, Rochester, New York.

3-16 Kodak Anti-Fog #1 (AF-70).

3-17 P. Dunn, J.M. Walls, Applied Optics 18, 263 (1979).

3-18 Spex, Inc., model 1704.

3-19 F.A. Jenkins, H.E. White, "Fundamentals of Optics", (McGraw-Hill, New York, 1957), pg. 328-350.

3-20 Hadland Photonics, Inc., with S-1 photocathode.

4- 1 C.D. Green, "Integral Equation Methods", (Barnes and Noble, New York, 1969), pg. 133.

4- 2 D.W. Sweeney, D.T. Attwood, L.W. Coleman, Applied Optics 15, 1126 (1976).

4- 3 D.W. Sweeney, Department of Energy Report No. C00-4001-6 (1978).

4- 4 C.M. Vest, "Holographic Interferometry",(Wiley, New York, 1979), pg. 329-334.

5- 1 D.W. Forslund, J.M. Kindel, E.L. Lindman, Physics of Fluids 18, 1002 (1975).

6- 1 D.W. Phillion, W.L. Kruer, V.C. Rupert, Physical Review Letters 39, 1529 (1977).

6- 2 W.L. Kruer, Bulletin of the American Physical Society 24, 1031 (1979).

6- 3 H.D. Shay, et al., Physics of Fluids 21, 1634 (1978).

6- 4 H.D. Shay, et al., Ibid.; R. Turner, L. Goldman, Laboratory For Laser Energetics Experimental Note No. 13, (1976) (unpublished).

6- 5 L.M. Goldman (private communication).

6- 6 J.M. Dawson, W.L. Kruer, B. Rosen, in"Dynamics of Ionized Gases", M. Lighthill, et al., editors, (University of Tokyo Press, Tokyo, 1973), pg. 47.

6- 7 S.J. Karttunen, R.E.E. Salomaa, Plasma Physics 21, 247 (1979); T.W. Johnston (private communication).